Nanomechanics of carbon nanotubes

by

Kenneth James Jensen

B.S. (Massachusetts Institute of Technology) 2003

A dissertation submitted in partial satisfaction of the
requirements for the degree of
Doctor of Philosophy

in

Physics

in the

GRADUATE DIVISION
of the
UNIVERSITY OF CALIFORNIA, BERKELEY

Committee in charge:
Professor Alex Zettl, Chair
Professor John Clarke
Professor Kristofer Pister

Fall 2008

The dissertation of Kenneth James Jensen is approved:

_____

Chair   Date

_____

Date

_____

Date

University of California, Berkeley

Fall 2008

Nanomechanics of carbon nanotubes

Copyright 2008

by

Kenneth James Jensen

Abstract

Nanomechanics of carbon nanotubes

by

Kenneth James Jensen

Doctor of Philosophy in Physics

University of California, Berkeley

Professor Alex Zettl, Chair

Advances in lithography and materials synthesis have enabled the fabrication of nanoscale mechanical devices, such as nanoscale resonators and bearings, which often exhibit behavior qualitatively different from that of their macroscopic counterparts. Accompanying these advances in fabrication, there has been an explosive growth in the number of techniques for observing and manipulating matter with nearly atomic resolution, such as the combination of electron microscopy with nanopositioning systems, which has allowed a variety experiments on these devices. Taking advantage of these advances, we study the mechanical properties of and develop novel applications for carbon nanotube-based mechanical devices.

This thesis is divided into three parts. In the first part, we describe the physics behind and potential signal processing and sensing applications of nanotube-based nanomechanical resonators. Specifically, we developed a nanomechanical resonator tunable over a

broad bandwidth using a multi-walled carbon nanotube's unique telescoping property. We also developed a nanomechanical sensor of radio waves, which was able to function as all of the components of a radio receiver: antenna, filter, amplifier, and demodulator. Finally, we constructed the first nanomechanical resonator capable of determining the mass of single atoms, essentially a new breed of mass spectrometer. Moreover, using this sensitive mass sensor, we observed a new form of shot noise, atomic mass shot noise, caused by the discrete addition of atomic masses.

In the second part, we describe precision force measurements on nanotube devices performed while observing the devices with atomic resolution inside a transmission electron microscope. In one experiment, we measured the forces involved during nanotube buckling, correlated these forces with the configuration of the nanotube, and analyzed the results with classical elastic theory. In another experiment, we measured the friction and interlayer forces between telescoping nanotubes. Under appropriate conditions, frictional forces were below the force resolution of our instrument, or less than 1.4×10^{-15} N/atom.

In the third part, we describe a method for using carbon nanotubes as nanofluidic channels to transport molten metals and as chemical reaction chambers to grow other carbon nanotubes. Using this method, we observed the growth of carbon nanotubes, in real-time, with atomic resolution inside the transmission electron microscope.

Professor Alex Zettl
Dissertation Committee Chair

In memory of Kevin, Edgar, and Anne

Contents

List of Figures

List of Tables

Acknowledgments

Acronyms

AFM	Atomic force microscope
AM	Amplitude modulation
CNT	Carbon nanotube
CVD	Chemical vapor deposition
CMOS	Complementary metal-oxide-semiconductor
DC	Direct current
ESI	Electrospray ionization
FM	Frequency modulation
MALDI	Matrix assisted laser desorption/ionization
MWNT	Multi-walled carbon nanotube
QCM	Quartz crystal microbalance
QPC	Quantum point contact
RF	Radio frequency
SEM	Scanning electron microscope
SET	Single electron transistor
SSET	Superconducting single electron transistor
STM	Scanning tunneling microscope
SWNT	Single-walled carbon nanotube
TEM	Transmission electron microscope
UHV	Ultra-high vacuum

Part I

Nanomechanical resonators

Chapter 1

Fundamentals of nanomechanical resonators

The vibrating strings of a violin and the beating head of a drum, the pendulum in a grandfather clock and the quartz crystal oscillator in a wristwatch – these are all examples of mechanical resonators. Even a single water molecule, with its scissors-like vibrational mode, could be construed as one. Though, in practice, the term "mechanical resonator" refers to mechanical systems designed to resonate at particular frequencies, to store mechanical energy efficiently, and to be monitored easily. The canonical example, familiar to any student of physics, is a spring with an attached mass, which is free to oscillate. This system is an important model of physics and appears over and over again in classical mechanics, the theory of waves, the theory of solids, and quantum mechanics.

Besides being interesting from a fundamental standpoint, mechanical resonators also have numerous practical applications. In particular, mechanical resonators excel in

applications where the size of corresponding electrical resonators would be too large or the resistive energy losses too great. A commercially relevant example is the acoustic wave filter in a cellular phone, which mechanically filters radio frequency (RF) signals far better than analogous electrical circuits. Another common example is the quartz crystal oscillator in a wristwatch, which keeps time more accurately and with less energy input than an electrical oscillator. Mechanical resonators also excel in applications where the physical displacement and mass of the resonator play an important role. As examples, the displacement of an atomic force microscope (AFM) cantilever allows it to image individual atoms, and the inertial mass of a mechanical resonator allows it to function as an accelerometer or inertial balance[1].

Recently, fabrication of nanoscale mechanical resonators, or nanomechanical resonators, has been made possible through advances in lithography and materials synthesis. These resonators typically take the form of a cantilevered beam or a doubly-clamped beam (a beam fixed at both ends) with widths on the order of nanometers and lengths on the order of microns. Nanomechanical resonators may be fabricated using standard "top-down" e-beam lithographic techniques[2, 3, 4]. Here, a wafer of silicon or other material is selectively etched away leaving a beam which is free to vibrate (see Fig. 1.1(A)). The primary advantage of this technique is the ease and control of fabrication and integration. Nanomechanical resonators may also be synthesized with "bottom-up" techniques (*e.g.* nanotubes, nanowires, *etc.*) and later assembled into functioning devices (see Fig. 1.1(B,C,D))[5, 6]. The advantage here lies in the unique properties of many nanomaterials. In this work, we employed the latter technique and fabricated our resonators from carbon nanotubes (see
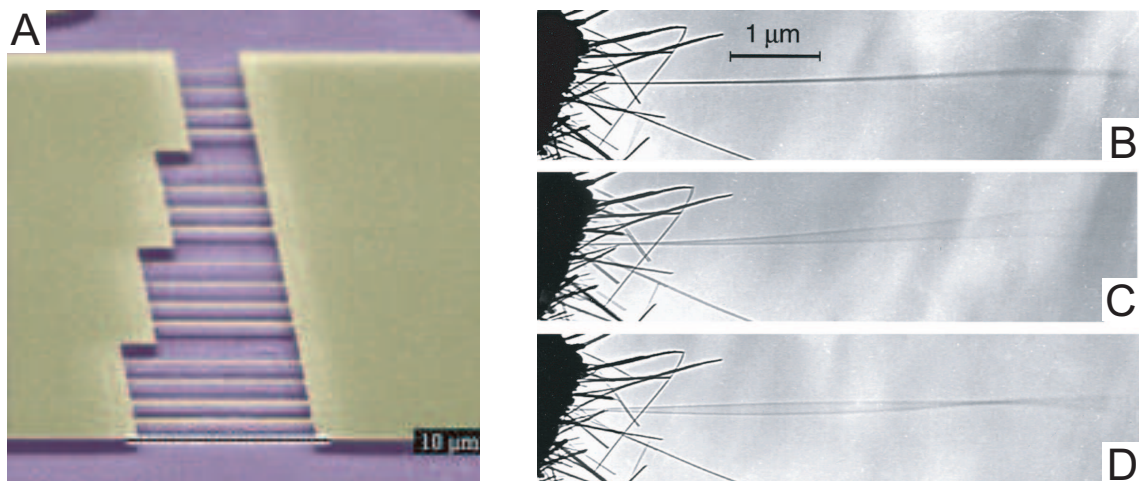
Figure 1.1: Examples of "top-down" (left) and "bottom-up" (right) nanomechanical resonators. (A) Array of nanomechanical resonators of various sizes fabricated with standard lithographic techniques from silicon[7]. (B,C,D) Carbon nanotube nanomechanical resonator vibrating in its fundamental and second modes[5].

App. A). Though, the theory and applications we discuss are relevant to all nanomechanical resonators.

Due to the scaling of their various properties with size, nanomechanical resonators have many advantages over their macroscopic counterparts. In particular, these resonators function as precise sensors. They currently hold records for force[8] and position[9, 10] sensitivity, $8.2 \times 10^{-19} \mathrm{N}/\sqrt{\mathrm{Hz}}$ and $3.8 \times 10^{-15} \mathrm{m}/\sqrt{\mathrm{Hz}}$ respectively. Moreover, they are also excellent mass sensors[11], and can even function as a new breed of mass spectrometer (see Ch. 4). Again due to scaling, nanomechanical resonators operate at high frequencies (*i.e.* radio and microwave frequencies), which makes them useful as signal processing elements (see Ch. 3), and also, interestingly, makes them valuable tools for studying the quantum theory of measurement and for testing quantum mechanics on macroscopic systems[12, 13, 14, 15, 16].

In this chapter we examine aspects of nanomechanical resonators, which are interesting from a fundamental physics standpoint and also critically affect their performance in various applications. The chapter is organized as follows: In Sec. 1.1, we briefly review the harmonic oscillator, as it applies to nanomechanical resonators, and its common extensions. This leads to a discussion in Sec. 1.2 of the dissipation of energy in nanomechanical resonators, which is intimately linked to a resonator's quality factor. The quality factor, of course, is a key figure of merit for the performance of a nanomechanical resonator. Another factor that determines performance is the method for detecting vibrations of the resonator. We describe multiple such signal transduction methods in Sec. 1.3 and discuss their relative merits. Both dissipation and signal transduction method play a key role in the mechanical noise in the resonator, which is discussed in Sec. 1.4. Noise limits our ability to precisely determine the position of the resonator or the forces acting on the resonator, and thus it sets the ultimate limit for the precision of nanomechanical sensors. In Sec. 1.5, we discuss how these various properties scale with the size of the system. Finally, in Sec. 1.6, we review the status of nanomechanical resonator technology, discuss interesting experiments, and highlight potential applications.

1.1 Harmonic oscillator and common extensions

The fundamental equation governing mechanical resonators (ignoring anharmonic effects) is the equation for the damped, driven harmonic oscillator:

$$m\ddot{y} + \lambda\dot{y} + ky = F\sin(\omega t). \tag{1.1}$$

Here y is the displacement of the mass from its equilibrium position, and $F\sin(\omega t)$ is the time varying force acting on the mass. The resonator's dynamics depend on only three parameters of the resonator itself, the mass m, spring constant k, and damping coefficient λ. The damping coefficient is often written in terms of a damping rate, $\Gamma = \lambda/m$.

For a given driving force amplitude, the steady-state response of the resonator is maximal near the resonance frequency of the system[1], which is defined by the familiar equation:

$$\omega_0 = \sqrt{\frac{k}{m}}. \tag{1.2}$$

More generally, the steady-state amplitude of the resonator as a function of frequency is

$$|Y(\omega)| = |H(\omega)|F = \frac{F/m}{\sqrt{(\omega^2 - \omega_0{}^2)^2 + \omega^2\Gamma^2}}. \tag{1.3}$$

And, the phase of the resonator relative to the driving signal is

$$\phi(\omega) = \arctan\left(\frac{\omega\Gamma}{\omega^2 - \omega_0{}^2}\right). \tag{1.4}$$

These relations are plotted in Fig. 1.2 for a typical resonator.

Interestingly, even complex mechanical systems with distributed mass and elasticity are successfully modeled as simple harmonic oscillators. Here, the actual mass of the system m must be replaced by an effective mass, m_{eff}, and the material's Young's modulus and geometry determine an effective spring constant, k_{eff}. Also, the force, which may be distributed along the length of the resonator or concentrated at a single point, is modified by a numerical constant, η. As the damping constant is generally determined empirically,

---

[1] The amplitude is maximal at the resonance of displacement: $\omega_{\text{d}} = \omega_0\sqrt{1 - \frac{1}{4Q^2}}$
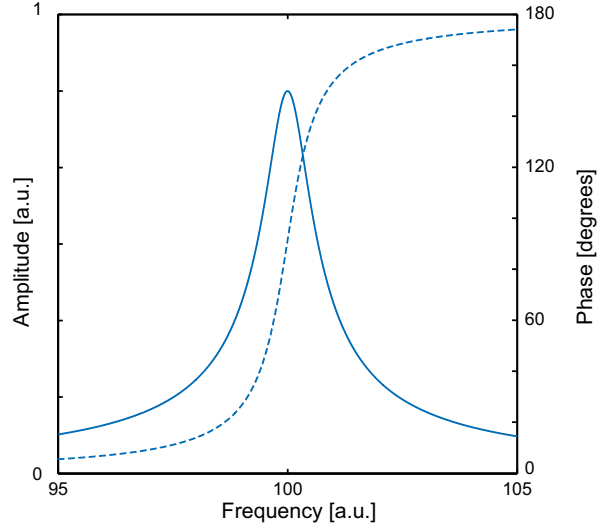
Figure 1.2: Amplitude (solid) and phase (dashed) response of a damped harmonic oscillator.

we leave its notation unchanged. The resulting equation is

$$m_{\text{eff}}\ddot{y} + \lambda\dot{y} + k_{\text{eff}}y = \eta F \sin(\omega t). \tag{1.5}$$

For cantilevered beams with a uniform cross-section along their length, the relevant case in this thesis, $m_{\text{eff}} \approx 0.24m$ and $k_{\text{eff}} = 3YI/L^3$, where Y is the Young's modulus and I is the areal moment of inertia. If the force is applied to just the tip of the cantilever, $\eta = 1$. (See App. B for detailed derivations.) Again, the resonance frequency is simply $\omega_0 = \sqrt{k_{\text{eff}}/m_{\text{eff}}}$.

At large amplitudes, most physical oscillators experience some form of nonlinear behavior due to nonlinearities in their spring constant. After all, Hooke's law is only a linear approximation of the true behavior of a spring. Including nonlinear spring terms up to y^3, the equation of motion becomes

$$m_{\text{eff}}\ddot{y} + \lambda\dot{y} + k_{\text{eff}}y + \alpha y^2 + \beta y^3 = F_{\text{eff}} \sin(\omega t). \tag{1.6}$$

For $\alpha = 0$ this is known as the Duffing oscillator equation, which, due to the symmetric

nature of the nonlinear potential, is the most common equation for describing nonlinearities in nanomechanical systems. The more general equation with $\alpha \neq 0$ is relevant to our work, and thus we describe the behavior of this equation here.

As a result of the nonlinearities, the resonance frequency of the oscillator depends on the amplitude of vibrations. This may be thought of in terms of an effective hardening or softening of the spring constant as a function of deflection amplitude. The relation between the shift in resonance frequency, $\delta\omega_0$, and amplitude, y_0, is[17]

$$\delta\omega_0 = \kappa {y_0}^2 = \left(\frac{3\beta}{8m_{\text{eff}}\omega_0} - \frac{5\alpha^2}{12{m_{\text{eff}}}^2{\omega_0}^3} \right) {y_0}^2. \tag{1.7}$$

Notably, all values of α result in a downward shift in resonance frequency, while shifts caused by β depend on its sign. In most nanomechanical systems, β is positive and thus results in an upward shift in resonance frequency.

Figure 1.3 shows the steady-state response of a nonlinear oscillator for different drive amplitudes. For small driving forces, the steady-state response is essentially that of a harmonic oscillator. For slightly larger driving forces, the resonance frequency begins to shift according to Eq. 1.7, but otherwise the behavior remains the same. However, for even larger driving forces, above a critical force, F_c, nonlinear oscillators exhibit a new behavior where at a given frequency there are three steady-state solutions with different amplitudes. The high and low amplitude solutions are stable, meaning that a resonator operating at that position of the response curve will continue to do so, while the middle solution is unstable. The experimental consequences of this are that if the frequency is swept from low to high, the amplitude will undergo a sharp transition at the peak of the resonance curve. Whereas if the frequency is swept from high to low, the amplitude will undergo a transition at a
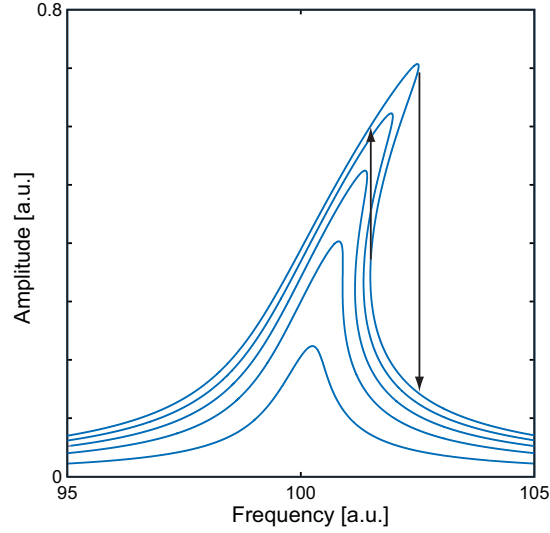
Figure 1.3: Amplitude response of a Duffing oscillator at different drive strengths. Notice how there are multiple stable solutions for large drive strengths at some frequencies.

lower frequency as shown in the figure.

The critical force and amplitude, which are important parameters for any nanomechanical resonator, are:

$$F_{\rm c} = \sqrt{\frac{4\sqrt{3}m_{\rm eff}{}^2\omega_0{}^2\Gamma^3}{9|\kappa|}}, \quad y_{\rm c} = \sqrt{\frac{4\sqrt{3}\Gamma}{9|\kappa|}}. \tag{1.8}$$

Often various properties of a resonator device, such as its sensitivity, can be improved simply by driving the resonator at a higher amplitude (see Sec. 1.5). However, the nonlinearities that occur above the critical amplitude ultimately limit the extent of these improvements.

1.2 Dissipation

Both the effective mass and spring constant in Eq. 1.5 are easy to determine from the resonator's geometry and material properties; however, determining the damping constant, λ, is more difficult. This constant, which describes the dissipation of energy in

the resonator, is critical to the performance of the nanomechanical resonator in a variety of applications. In fact, one of the primary distinguishing features of nanomechanical resonators is that at a given frequency and for a given size they are much less dissipative than standard electrical resonators. Here, we describe the effects of dissipation on the resonator's properties, various sources of dissipation, and some methods for controlling dissipation.

One of the primary effects of dissipation is the broadening of a system's resonance peak. The sharpness of a resonance peak is described by a dimensionless number known as the quality factor or Q. The quality factor is defined as

$$Q = \frac{\omega_0}{\Gamma} = \frac{2\pi U_0}{\Delta U} \tag{1.9}$$

where U_0 is the elastic energy initially stored in the resonator and ΔU is the energy lost each cycle of oscillation. This number figures prominently in the amplitude of vibrations on resonance, $|Y(\omega_0)| = FQ/m\omega_0^2$, and in the width of the resonance peak, $\Delta\omega = \omega_0/Q$.[2] Figure 1.4 shows two resonance peaks with different Q values. A tall and narrow high-Q peak, such as the one shown in the figure, would be ideal for sensing applications and filters, while the short and wide low-Q peak would be needed for broad-bandwidth devices.

There are a variety of dissipation mechanisms that affect nanomechanical resonators. These are broadly classified as extrinsic or intrinsic mechanisms. Extrinsic mechanisms result from couplings between the resonator and its environment. For example, energy lost via friction to a surrounding gas or radiated away as acoustic waves through the resonator's supports are common forms of extrinsic dissipation. On the other hand, intrinsic mechanisms are a fundamental property of the resonator itself. Some prominent intrinsic

---

[2]Here $\Delta\omega$ is the full-width at half maximum for the *energy* resonance peak.
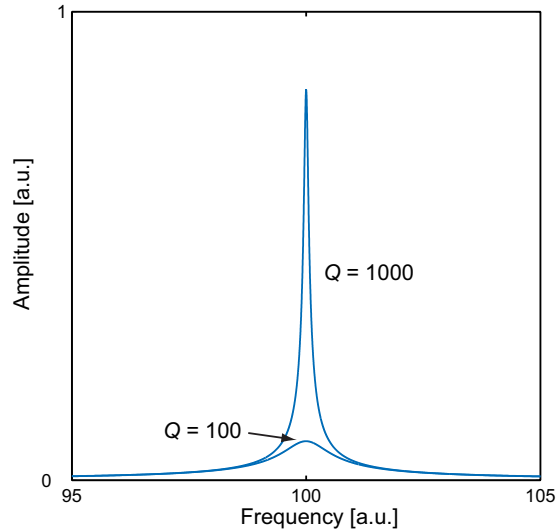
Figure 1.4: Amplitude response of a damped harmonic oscillator with different Q values.

dissipation mechanisms are phonon-phonon scattering, phonon-electron scattering, surface losses, and thermoelastic dissipation. In general, extrinsic dissipation is easier to control than intrinsic dissipation because it is often easier to change a resonator's environment than to change a resonator's material.

For nanomechanical resonators, there is significant evidence that clamping losses and surface losses dominate over other forms of dissipation[18, 19]. If these two loss mechanisms could be controlled, then it is expected that thermoelastic dissipation would be the ultimate limit on Q. Indeed, for slightly larger micromechanical resonators, thermoelastic dissipation is the ultimate limit[20, 21]. Thus, we consider each of these dissipation mechanisms in more detail below. The nanomechanical resonators in this work are primarily constructed from carbon nanotubes. Some sources of dissipation are unique to carbon nanotubes such as the sliding friction between the walls of a multi-walled carbon nanotube.

This particular form of dissipation will be discussed in more detail in Ch. 6.

The combined effect of all the dissipation mechanisms or equivalently the total rate of energy loss is the sum of the rates from each loss mechanism. Thus, to find the total coupling constant, Γ_{tot}, we sum the coupling constants from each source: $\Gamma_{\text{tot}} = \Gamma_{\text{clamp}} + \Gamma_{\text{surf}} + \Gamma_{\text{TE}} + ...$ Likewise, the total quality factor, Q_{tot}, is determined from the quality factor of each source as follows:

$$Q_{\text{tot}}{}^{-1} = Q_{\text{clamp}}{}^{-1} + Q_{\text{surf}}{}^{-1} + Q_{\text{TE}}{}^{-1} + ... \tag{1.10}$$

as is easily seen from Eq.1.9.

1.2.1 Clamping losses

Clamping loss refers to mechanical energy dissipated through a resonator's supports. There are two modes of clamping loss, which we term elastic and inelastic clamping loss. In elastic clamping loss, energy is radiated away through the supports by surface or bulk acoustic waves excited by the resonator's vibrations. In inelastic clamping loss, energy is dissipated through a viscous clamp to the support.

There have been many detailed theoretical analyses of elastic clamping loss, especially as it applies to beams with a rectangular cross-section. Though nanotubes have a circular cross-section, these analyses provide the correct order-of-magnitude of elastic clamping loss. For a rectangular cantilevered beam with width, w, thickness, t, and length, L, attached to a semi-infinite half-space support composed of the same material, the predicted dissipation is[22]

$$Q_{\text{el.clamp}}{}^{-1} = \alpha \frac{w}{L} \left(\frac{t}{L} \right)^4 \tag{1.11}$$
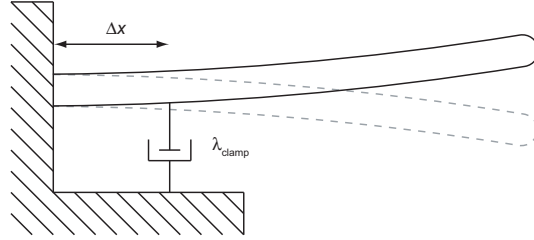
Figure 1.5: Inelastic clamping loss model.

where $\alpha \approx 0.3$ is a proportionality constant weakly dependent upon the material's Poisson ratio. Thus, for a cylindrical beam with radius r, $Q_{\text{el.clamp}}^{-1} \approx \alpha(2r/L)^5$.

Inelastic clamping loss is comparatively less well understood. We model inelastic clamping loss through a viscous damper with damping constant λ_{clamp} attached a short distance, Δx, away from the resonator's clamp as shown in Fig. 1.5. Assuming that the damper has a negligible effect on the resonance frequency or mode shape, $y_0(x)$, of the cantilevered beam, the quality factor is given by Eq. 1.9 where $U_0 = \frac{1}{2}m_{\text{eff}}\omega_0^2 y_0(L)^2$ and $\Delta U = \pi\lambda_{\text{clamp}}\omega_0 y_0(\Delta x)^2$. (The mode shape of a cantilever is calculated in App. B.) Thus, the inelastic clamping loss for the fundamental resonance mode is

$$Q_{\text{in.clamp}}^{-1} \approx 3.09\frac{\lambda_{\text{clamp}}}{\omega_0 m_{\text{eff}}}\left(\frac{\Delta x}{L}\right)^4. \tag{1.12}$$

Assuming that λ_{clamp} scales as r and Δx is independent of geometry, the inelastic clamping loss is proportional to $1/r^2 L^3$.

The easiest way to control both forms of clamping loss is simply to create a resonator with a high aspect ratio, L/r. Nanotubes naturally have exceptionally high aspect ratios. According to Eq. 1.11, for typical nanotube resonators ($L = 1\mu$m, $r = 5$ nm), $Q_{\text{el.clamp}}^{-1} \approx 3 \times 10^{-11}$, which is clearly negligible. As λ_{clamp} and Δx depend on the nature

of the clamp, the magnitude of inelastic clamping varies widely, and it could be a significant source of dissipation in nanotube resonators. Alternate techniques for controlling clamping loss exist such as clamping at the nodal points of the resonator's vibrations[23] and fabricating resonators with a tuning fork configuration such that the resonator's vibrations destructively interfere at the support.

1.2.2 Surface losses

Surface losses are caused by metastable systems that commonly exist at a resonator's surface such as adsorbed molecules, dangling or broken bonds, or an amorphous oxide layer. Transitions between stable states of these systems are excited by the vibrations of the resonator. These systems absorb energy from the fundamental resonance mode and irreversibly transfer it other mechanical modes and thermal energy.

There is strong evidence for the importance of surface losses at the nanoscale. In particular, Mohanty *et al.* have noticed a disturbing trend in the quality factors of resonators as a function of resonator volume (see Fig. 1.6)[18]. From the giant resonant bar gravitational wave antennas[24] to the smallest nanomechanical resonators, as the resonator gets smaller so does its quality factor. Indeed, our own nanotube resonators, which have relatively high Q's when compared to other nanotube resonators[6], follow the trend comfortably, as indicated by the left-most datum in Fig. 1.6.

To explain how this trend supports the dominance of surface losses, we consider the definition for the quality factor. For resonating beams, the energy of a resonator is stored in the elastic strain throughout its volume and thus is proportional to its volume, V.
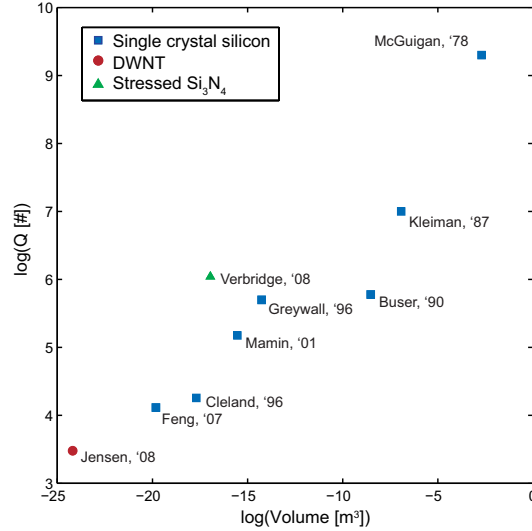
Figure 1.6: Quality factor versus resonator volume. There is a clear trend toward smaller quality factors as resonators become smaller[24, 25, 26, 27, 21, 8, 2, 28, 29]. A possible explanation is the increase in surface-to-volume ratio.

If we assume that energy is predominately dissipated at the surface, then we would expect that the energy lost per cycle would be proportional to the surface area S, and thus:

$$Q_{\mathrm{surf}}^{-1} \propto \frac{S}{V} \tag{1.13}$$

which describes the trend in Fig. 1.6.

There are two methods, other than increasing the size of the resonator, proven to reduce the effects of surface losses. In the first method, contaminants are removed from the surface via high-temperature annealing in vacuum. For single crystal silicon resonators, such a treatment results in more than an order-of-magnitude increase in Q[30]. In the second method, the surface of the resonator is terminated with a methyl or other functional group, which impedes oxidation of the surface. Again, increases in quality factor of almost an order-of-magnitude are reported[31].

1.2.3 Thermoelastic dissipation

Thermoelastic dissipation arises from temperature gradients created in a resonator as a result of its vibrations. As a beam bends, sections of the beam contract while other sections expand. Just as a gas warms or cools upon adiabatic contraction or expansion, the contracted sections of the beam warm and the expanded sections cool. Consequently, heat flows irreversibly from the hot sections to the cool sections, which results in the dissipation of mechanical energy. An approximation for the magnitude of this effect[3], originally derived by Zener[33], gives

$$Q_{\text{TE}}^{-1} = \frac{Y \alpha_T{}^2 T}{c_v} \frac{\omega \tau}{1 + \omega^2 \tau^2}, \quad \tau = \frac{t^2 c_v}{\pi^2 \kappa_T}, \tag{1.14}$$

where, Y is the Young's modulus, $\alpha_T = \frac{1}{L} \frac{\partial L}{\partial T}$ is the linear thermal expansion coefficient, c_v is the volumetric specific heat capacity, and τ is the characteristic thermal relaxation time, which also depends on the thickness t and thermal conductivity κ_T of the beam.

Examination of Eq. 1.14 suggests a few methods for controlling thermoelastic dissipation. The resonator's material can be selected such that it has a lower Y or α_T. Also, κ_T, c_v, or ω can be tuned such that the thermal relaxation time is significantly different from the oscillation period, resulting in lower dissipation. Finally, lowering the temperature is a good material-independent way of reducing thermoelastic dissipation.

Thermoelastic dissipation is the dominant form of dissipation for some microme-chanical resonators[20, 21]. Current nanomechanical resonators are likely dominated by other forms of dissipation such as clamping loss and surface losses; however, it may be possible to reduce these losses through clever engineering as discussed above[23, 31]. Thus, for

---

[3]An exact but more complicated form of this result is given in Ref. [32]

any given material, thermoelastic dissipation provides the ultimate upper limit on quality factor. For typical carbon nanotubes (L=1 μm, r=5 nm) at room temperature, using the parameters for Y, α_T, c_v and κ given in App. A, we calculate the thermoelastic dissipation to be $Q_{\mathrm{TE}}^{-1} \approx 2 \times 10^{-8}$ and thus the upper limit on Q is 4×10^7. Our current nanotube resonators have Q's closer to 1000, indicating that this is not yet the dominant form of dissipation.

1.3 Signal transduction

Signal transduction is the conversion of a resonator's mechanical vibrations into an easily detectable signal, such as an electrical signal, a necessary step for integration with standard electronics. Mature methods of signal transduction exist for micromechanical resonators. However, these methods often fail at the nanoscale. For example, reflection of a laser beam, a common technique for AFM resonators, does not work efficiently for nanomechanical resonators because they are smaller than the wavelength of light. Thus, a host of new signal transduction technologies have been developed for nanomechanical resonators. Here, we briefly review some of the techniques currently used, and then discuss a novel technique, field emission detection, in more detail.

1.3.1 Capacitive

Capacitive detection is one of the primary methods used for micromechanical resonators[34]. This method relies on the variations in capacitance between a vibrating resonator and a stationary electrode. Due to the small size of nanomechanical resonators,

there is very little area between the resonator and stationary electrode, and thus, there is a very small capacitance between these electrodes. This capacitance is typically $\sim 10^{-17}$ F and variation due to vibrations is typically $\sim 10^{-19}$ F[35]. Such a small variation is difficult to measure with the standard technique.

A clever and simple modification of standard capacitance detection extends this technique into the nanoscale regime[35]. The trick is simply to charge the resonator by applying a DC voltage. Now, when an RF signal at the resonance frequency of the resonator is applied to the electrode opposite the resonator, it forces the resonator to vibrate significantly. The RF power dissipated in the resonator is detectable with RF reflectometry.

Multiple other techniques harness variations in capacitance for signal transduction. Some techniques exploit variations in capacitance to modulate the strain in a device. For example, this has been used to detect the vibrations of piezoresistive resonators[36] and carbon nanotube-based resonators[6, 37]. Other techniques, such as the quantum point contact (QPC)[38] and single electron transistor (SET)[10, 9] techniques, use variations in capacitance as a form of variable gate. As the resonator nears the junction of the QPC or the island of the SET it gates the junction or island. For the QPC this alters the number of open conductance channels. For the SET it changes the resonant scattering conditions. Both techniques require low-temperatures, and thus may not be suitable for practical applications. However, these techniques, particularly the SET technique, are some of the most precise displacement detection methods.

1.3.2 Magnetomotive

Magnetomotive detection was one of the first techniques proposed for nanomechanical resonators[2], and it remains one of the most popular. Here, a circuit containing a conducting nanomechanical resonator is placed in a large external magnetic field. An RF current is injected into the resonator causing it to vibrate via the Lorentz force. As the resonator vibrates the area enclosed by the circuit and thus the magnetic flux enclosed oscillates. According to Faraday's law, this creates a back electromotive force, which is detected using RF reflectometry.

The advantages of this technique are that it is easy to implement and scales well with size. However, there are two significant disadvantages. First, it requires a large external magnet with a field of typically a few tesla. Obviously, this complicates commercial applications. Second, this technique is naturally dissipative[39], which will reduce the Q's and possibly limit applications.

1.3.3 Near-field optical

As mentioned earlier, standard optical detection techniques fail for nanomechanical resonators because the resonators are smaller than the wavelength of light and thus do not scatter light efficiently. Though some larger nanomechanical resonators still use these techniques[8, 21], they sacrifice many of the advantages of nanoscale size.

For true nanomechanical resonators, it is still possible to use optical techniques by exploiting near field effects[7]. In one experiment, this was accomplished by fabricating the resonator less than a wavelength away from a photonic waveguide[40]. Photons can tunnel

from the waveguide to the resonator, which serves as a second wave guide. This coupling is dependent on the distance between the resonator and waveguide, and thus is dependent on the vibrations of the resonator. By monitoring the power transmitted through the first waveguide, it is possible to detect vibrations of the resonator.

Such techniques have excellent bandwidth. However, their sensitivity is still much worse than the sensitivity of other techniques (*e.g.* SET detection). Moreover, this technique has yet to be demonstrated on resonators with widths less than 100 nm.

1.3.4 Tunneling

Tunneling is renowned for its displacement detection sensitivity as is demonstrated by its use in scanning tunneling microscopy (STM). Thus, it is an obvious candidate for nanomechanical resonator displacement sensing. Indeed, theoretical work has predicted that tunneling detection could reach the quantum limit of position measurement[41].

One challenge to overcome with tunneling detection is the typically low bandwidths involved. Whereas STMs operate with a bandwidth of a few kilohertz, a nanomechanical resonance detection scheme must operate with a bandwidth in the megahertz range. The bandwidth of STMs is limited because the high junction resistance and any parasitic capacitances serve as a low pass filter. However, it is possible to transform the high junction resistance down to 50 Ω using a resonant transformer, which has proven useful in increasing bandwidth for a number of experiments[42, 43]. A second challenge is reproducibly fabricating nanomechanical devices with tunnel junctions. Standard techniques for fabricating tunnel junctions rely on both sides of the junction remaining stationary, which obviously

does not occur for nanomechanical resonators. Thus, new fabrication techniques must be developed.

1.3.5 Field emission

Field emission detection[44, 45] is the technique we champion in this work. It is a variation of tunneling detection that relaxes the requirement that the resonator be positioned within a few nanometers of an electrode. This technique works best for cantilevered resonators, through perhaps a variation would also work for doubly clamped resonators.

Field emission is the extraction of electrons from a conductor by a strong electric field. It is distinct from thermionic emission in that the electrons do not have sufficient thermal energy to overcome the conductor's work function. Rather, due to the strong electric field, the electrons tunnel through the potential barrier between the conductor and the vacuum. As shown in Fig. 1.7, the distance an electron must tunnel is related to the applied electric field.

The field emission current is governed by the Fowler-Nordheim law[46]:

$$I = c_1 A (\gamma E_{\text{ext}})^2 \exp\left(-\frac{c_2}{\gamma E_{\text{ext}}}\right) \tag{1.15}$$

where A is the area from which the metal emits electrons, E_{ext} is the external applied electric field, and γ is the local field enhancement factor. The field enhancement factor is essentially a measure of how much the geometry of the resonator concentrates the electric field. The constants c_1 and c_2 involve only fundamental constants and the metal's work function.

Field emission detection works by coupling the electric field to vibrations of the
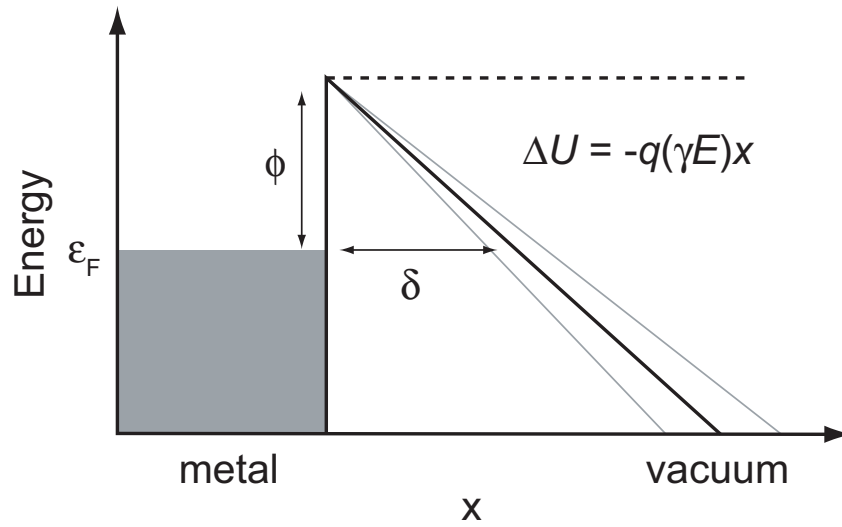
Figure 1.7: Field emission detection. Diagram of relevant energy levels versus position for field emission.
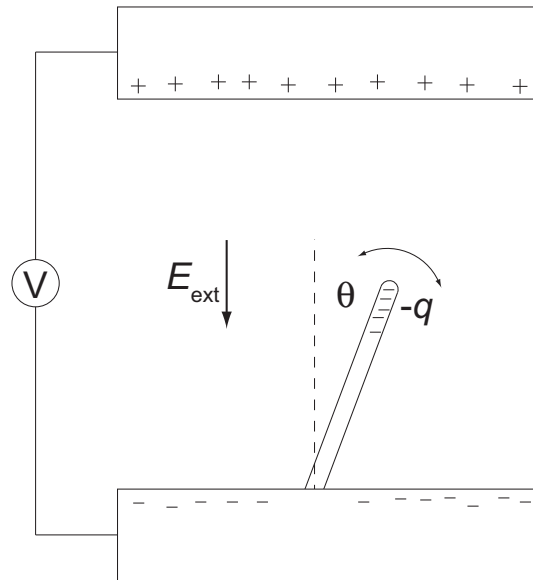
Figure 1.8: Geometry of a field emitting nanotube.

resonator. This is accomplished through the field enhancement factor, the only parameter in Eq. 1.15 that depends on the geometry. Figure 1.8 depicts the geometry of a field-emitting nanotube resonator. As the nanotube vibrates the distance between its tip and the electrode to which it is mounted varies by approximately $y_0 \sin \theta$, where y_0 is the amplitude of vibrations at the nanotube's tip and θ is the misalignment angle of the nanotube. This effectively varies how "sharp" the nanotube appears, and thus changes the field enhancement factor. To a good approximation, the field enhancement factor is $\gamma \approx 3.5 + h/r$ where h is the height of the tip of the nanotube over the electrode and r is the radius of the tip of the nanotube[47]. Thus, as the nanotube vibrates, the field enhancement factor varies by approximately $y_0 \sin \theta/r$.

Field emission detection shares all the advantages of tunneling detection. It is extremely sensitive to displacements. It does not add significant dissipation. It can operate on cantilevered resonators as it does not require a continuous electrical path. It also has the additional advantage that devices are much easier to fabricate. Like all detection techniques, it too has its disadvantages. Most notably, field emission is noisy both electrically[48] and mechanically (see Sec. 1.4). Field emission requires high voltages (typically 100 V in our devices), which may make it unsuitable for portable applications. Finally, field emission requires a high vacuum to prevent destruction of the device by ionized atoms in the surrounding gas.

1.4   Mechanical noise

Nanomechanical resonators are excellent sensors of position, force, mass, and numerous other quantities[4]. However, this very sensitivity implies that they may respond in unwanted ways to other quantities, thus obscuring the desired signal. Since noise ultimately limits their potential applications, understanding and controlling mechanical noise is critical. Here, we define various metrics of noise, describe and quantify common noise sources, and discuss methods for controlling noise.

Two metrics are commonly used to quantify noise in a resonator, power spectral density and Allan variance. Power spectral density is a measure of signal power in the frequency domain. It is defined as the Fourier transform of the auto-correlation function of a signal $x(t)$, or more precisely[4]

$$S_x(\omega) = \frac{1}{\pi} \int_{-\infty}^{\infty} \langle x(t)x(t+\tau) \rangle e^{-i\omega\tau} d\tau. \tag{1.16}$$

We often use the normal frequency, rather than angular frequency, version of Eq. 1.16, which is related by a simple change of variables: $S_x(f) = 2\pi S_x(\omega)$.

Allan variance is a measure of frequency stability in the time domain. It is defined as one-half of the time-average of the squared difference between successive samples of frequency deviation, or more precisely[33]:

$$\sigma_A{}^2(\tau) = \frac{1}{2f_c{}^2} \frac{1}{N-1} \sum_{n=2}^{N} (\overline{f_n} - \overline{f_{n-1}})^2 \tag{1.17}$$

Here, f_c is the mean overall frequency and $\overline{f_n}$ is the mean frequency over the nth sample with sample time τ. As Allan variance is typically used to measure frequency stability, we

---

[4]This is the one-sided power spectral density as is used throughout this thesis.

give its formula in terms of a frequency signal, though it can also be used with more general

signals.

As one would expect, these two metrics for noise are related[33]:

$$\sigma_A{}^2(\tau) = \frac{2}{\omega_0{}^2} \int_0^\infty S_{\omega_0}(\omega) \frac{\sin^4(\omega\tau/2)}{(\omega\tau/2)^2} d\omega. \tag{1.18}$$

Allan variance is easier to measure and more intuitive than spectral density, and as such it

is commonly used for measuring the stability of oscillators. It, however, does not contain

all the information about fluctuations. In this sense, spectral density is a more fundamental

metric for fluctuations.

There are a variety of noise sources which affect nanomechanical resonators. The

dominant mechanical noise source for most room-temperature resonators is the thermal

vibration of the resonator or thermomechanical noise, the mechanical analogue of Johnson-

Nyquist voltage noise in resistors. At low temperatures or for particularly small resonators,

other noise sources become significant. Two that have particular relevance for nanomechan-

ical resonators are temperature fluctuation noise, due to the small heat capacities involved,

and adsorption-desorption noise, due to the small resonator masses involved. Also, partic-

ular signal transduction methods often introduce their own noise. Field emission detection,

our preferred detection scheme, is actually the dominant mechanical noise source for our

nanotube resonators. We discuss each of these noise sources in more detail below.

1.4.1   Thermomechanical noise

According to the fluctuation-dissipation theorem[49], any dissipation in a resonator

naturally leads to fluctuations. This is essentially the same effect as the thermal voltage

fluctuations, or Johnson-Nyquist noise, in resistors. Indeed, the fluctuations in force experienced by a resonator are described by an equation similar to the equation for Johnson-Nyquist noise in a resistor, $S_V(f) = 4k_\mathrm{B}TR$, except the resistance R is replaced by the "resistance" of the resonator $m_\mathrm{eff}\Gamma$ (see Eq. 1.5), so that

$$S_F(f) = 4k_\mathrm{B}Tm_\mathrm{eff}\Gamma. \tag{1.19}$$

Similarly to the voltage fluctuations in a resistor, the force fluctuations in a resonator are white, or frequency independent.

When we monitor a resonator, we do not generally measure the force acting on it. Rather, we measure its position or possibly its resonance frequency. Thus, we analyze how the force noise affects the position noise and frequency noise. To convert force noise to position noise, we multiply $S_F(\omega)$ by the squared response function $|H(\omega)|^2$ (see Eq. 1.3):

$$S_y(\omega) = |H(\omega)|^2 S_F(\omega) = \frac{1}{m_\mathrm{eff}^2} \frac{S_F(\omega)}{(\omega^2 - \omega_0^2)^2 + \omega^2\Gamma^2}. \tag{1.20}$$

As expected, the position noise is maximal near the resonance frequency of the system; in effect, the mechanical resonance is acting as a band-pass filter on the force noise.

To convert position noise to frequency noise, we first convert position noise to phase noise. The time averaged phase noise is $S_\phi(\omega) = S_y(\omega)/\langle y_0^2\rangle$ where $\langle y_0^2\rangle$ is the mean-squared amplitude of the forced vibrations of the resonator. Thus, if we drive the resonator at its critical amplitude y_c, $S_\phi(\omega) \approx 2S_y(\omega)/y_\mathrm{c}^2$. Finally, the frequency noise is[50, 11]

$$\begin{aligned}
S_{\omega_0}(\omega) &= \frac{S_\phi(\omega)}{(\partial\phi/\partial\omega)^2} \approx \frac{\Gamma^2}{2} \frac{S_y(\omega)}{y_\mathrm{c}^2} \\
&\approx \frac{1}{2\pi} \frac{k_\mathrm{B}T}{U_\mathrm{c}} \frac{\omega_0^2\Gamma^3}{(\omega^2 - \omega_0^2)^2 + \omega^2\Gamma^2}
\end{aligned} \tag{1.21}$$

where $U_c = \frac{1}{2}m_{\text{eff}}\omega_0{}^2 y_c{}^2$ is the critical driving energy. On resonance the frequency noise is simply: $S_{\omega_0}(\omega_0) \approx \frac{1}{2\pi}\frac{k_B T}{U_c}\Gamma$.

For a typical carbon nanotube-based nanomechanical resonator (r=5 nm, L=1 μm, Q=1000, $y_c \approx 100$ nm) operating at room temperature, the frequency noise is: $\sqrt{S_{f_0}(f_0)} \approx 1.7\text{Hz}/\sqrt{\text{Hz}}$

1.4.2 Temperature fluctuation noise

Due to their small heat capacities and their low thermal conductances, nanoscale systems can experience drastic changes in temperature. These temperature fluctuations are modeled using the analogue of Johnson-Nyquist noise for thermal circuits. The spectral density of the temperature fluctuations across a thermal conductance G is $S_T(f) = 4k_B T^2/G$[51]. If the thermal conductor connects a system with heat capacity C to a thermal reservoir at temperature T, the resulting temperature fluctuations are

$$S_T(\omega) = \frac{2}{\pi}\frac{k_B T^2/G}{1 + \omega^2 \tau_T{}^2} \tag{1.22}$$

where $\tau_T = C/G$ is the thermal time constant of the system. For nanomechanical resonators in direct contact with a thermal reservoir, a model with distributed heat capacities and thermal conductances is necessary[50]. Here, Eq. 1.22 holds with the heat capacity C replaced by the heat capacity of a section of the resonator with length on the order of the phonon mean free path, and the conductance G replaced by *half* the conductance of the same section of the resonator. (For a detailed calculation, see Ref. [50].)

For a nanomechanical resonator, these temperature fluctuations cause shifts in resonance frequency through temperature-induced variations of the resonator's length L

and speed-of-sound, $c_{\mathrm{s}} \approx \sqrt{Y/\rho}$. Accordingly, the spectral density of the frequency noise is $S_{\omega_0}(\omega) = (d\omega_0/dT)^2 S_T(\omega)$, which upon expanding $d\omega_0/dT$ in terms of the frequency shifts caused by length changes (first term in parentheses below) and shifts from speed-of-sound changes (second term) is[50, 11]

$$S_{\omega_0}(\omega) = \frac{4}{\pi}\left(-\frac{11.2c_{\mathrm{s}}^2}{\omega_0 L^2}\alpha_T + \frac{\omega_0}{c_{\mathrm{s}}}\frac{\partial c_{\mathrm{s}}}{\partial T}\right)^2 \frac{k_{\mathrm{B}}T^2/G}{1+\omega^2\tau_T^2} \tag{1.23}$$

where τ_T is the thermal time constant of a section of the beam with length on the order of the mean free path and G is the thermal conductance for the same section.

For a typical nanotube-based nanomechanical resonator operating at room temperature, the temperature-induced frequency noise is: $\sqrt{S_{f_0}(f)} \approx 140.6\,\mathrm{Hz}/\sqrt{\mathrm{Hz}}$

1.4.3 Adsorption-desorption noise

Due to their small effective mass, nanomechanical resonators experience significant frequency shifts from changes in mass caused by single atoms or molecules adsorbing to or desorbing from the resonator's surface.

To calculate the total adsorption-desorption noise, we first calculate the noise at a single adsorption site. For the moment, we ignore the mass of the adsorbate and its effect on the resonance frequency, and we simply calculate the spectral density of the occupation number, n_{occ}, of adsorbates at the site. Obviously, there can be only zero or one adsorbate at a given site. Also, the adsorption and desorption processes have characteristic rates r_{a} and r_{d}. Thus, the occupation number may be described as a telegraph process, which has mean occupation number $\langle n_{\mathrm{occ}}\rangle = r_{\mathrm{a}}/(r_{\mathrm{a}}+r_{\mathrm{d}})$, occupation number variance $\sigma_{\mathrm{occ}}^2 = r_{\mathrm{a}}r_{\mathrm{d}}/(r_{\mathrm{a}}+r_{\mathrm{d}})^2$, and correlation function $\langle n_{\mathrm{occ}}(t')n_{\mathrm{occ}}(t'+t)\rangle = \sigma_{\mathrm{occ}}^2\exp(-|t|/\tau_{\mathrm{r}})$

with characteristic time $\tau_r = 1/(r_a + r_d)$. From the definition of spectral density (see Eq. 1.16), we find:

$$S_n(\omega) = \frac{2}{\pi} \frac{\sigma_{\text{occ}}^2 \tau_r}{1 + \omega^2 \tau_r^2}. \tag{1.24}$$

Finally, we sum the contributions of $S_n(\omega)$ at each of the N_a adsorption sites and multiply the result by $(d\omega_0/dn)^2 = (\omega_0 m/2m_0)^2$, where m is the mass of the adsorbate and m_0 is the total initial mass of the resonator. Thus, the total frequency noise caused by adsorption and desorption of particles is[50, 11]

$$S_{\omega_0}(\omega) = \frac{1}{2\pi} \frac{\omega_0^2 N_a \sigma_{\text{occ}}^2 \tau_r}{1 + \omega^2 \tau_r^2} \left(\frac{m}{m_0} \right)^2. \tag{1.25}$$

The adsorption rate may be calculated from the collision rate of gas particles with the adsorption site assuming some sticking coefficient s: $r_a = \frac{2}{5} P A_a s / \sqrt{m k_B T}$, where P is the pressure and A_a is the area of the adsorption site. Desorption may be treated as a thermally activated process with a potential barrier E_b and an attempt frequency ν_d (typically 10^{13} Hz[50]), and thus the desorption rate is $r_d = \nu_d \exp(-E_b/k_B T)$.

For a typical nanotube-based nanomechanical resonator the adsorption-desorption noise is negligible.

1.4.4 Field emission specific noise sources

Specific detection schemes often introduce their own sources of noise. For example, optical detection schemes introduce photon shot noise[52] and capacitive detection schemes introduce amplifier noise[35]. Likewise, our preferred detection scheme, field emission detection[45], introduces various noise sources, the dominant one of which is tension noise.

Variations in tension are caused by variations in the charge stored at the tip of the carbon nanotube. These charge variations are predominately caused by variations in the field enhancement factor, which in turn are caused by the thermal vibrations of the nanotube. Thus, to determine the tension noise $S_T(\omega)$ we multiply the position noise $S_y(\omega)$ by $(dT/d\gamma)^2 = (4\pi\epsilon_0 r^2 E_{\text{ext}}{}^2)^2$ and $(d\gamma/dy)^2 \approx (\sin\theta/r)^2$:

$$S_T(\omega) = \left(4\pi\epsilon r^2 E_{\text{ext}}{}^2\right)^2 \left(\frac{\sin\theta}{r}\right)^2 S_y(\omega). \tag{1.26}$$

This may be converted to frequency noise by multiplying by $(d\omega_0/dT)^2$. The effects of tension on the resonance frequency of a beam, such as a carbon nanotube, are calculated in App. B. The resulting frequency noise is

$$S_{\omega_0}(\omega) = \left(\frac{1.07}{2m_{\text{eff}}\omega_0 L}\right)^2 S_T(\omega). \tag{1.27}$$

For a typical nanotube-based nanomechanical resonator operating at room temperature, the tension noise is 235 Hz/$\sqrt{\text{Hz}}$.

1.5 Scaling

Much of what has been discussed so far applies to macroscopic resonators as well as nanoscale resonators. But, this is not a thesis on macroscopic resonators! What really distinguishes nanomechanical resonators as interesting objects of study? Here, we discuss how the various properties of resonators scale with the size of the resonator. In doing so, we find at least four areas where nanomechanical resonators are significantly superior to their macroscopic counterparts: high resonance frequency, potential to access quantum effects, improved force sensitivity, and improved mass sensitivity.

1.5.1 Resonance frequency

As mechanical resonators become smaller, their resonance frequency increases. The guitar string provides a common macroscopic example. As the string is shortened, by pressing a finger on the fret board, its pitch increases. Likewise, as the width of a string decreases, its pitch again increases. For mechanical resonators in general, this trend continues all the way down to the nanoscale.

For a cylindrical beam, the resonance frequency scales as (see App. B)[5]

$$\omega_0 \propto \frac{r}{L^2}. \tag{1.28}$$

Thus for a fixed aspect ratio, L/r, decreasing the length results in a higher resonance frequency.

For carbon nanotubes, this scaling results in resonance frequencies that are typically in the megahertz to gigahertz frequency range[6, 53]. This is a commercially relevant frequency range which includes FM radio, cellular communications, wireless computer networks, the global positioning system, and numerous other applications. Indeed, carbon nanotubes are being explored as signal processing elements for such applications (see Ch. 2).

1.5.2 Quantum effects

Another effect of high resonance frequencies is the potential to access quantum effects in nanomechanical resonators. The energy levels of a harmonic oscillator are $U_n = \hbar\omega(n + 1/2)$, and thus the ground state of a nanomechanical resonator has energy $U_0 =$

---

[5]For a cylindrical *string*, the resonance frequency scales as $1/rL$.

$\frac{1}{2}\hbar\omega_0$. According to the equipartition theorem, there is $\frac{1}{2}k_{\mathrm{B}}T$ energy in each harmonic degree-of-freedom at temperature T. For a 1 GHz resonator, these energy scales become equivalent at a temperature of just 48 mK, which is accessible in a laboratory with a common dilution refrigerator. Thus, in general, for nanomechanical resonators cooled to millikelvin temperatures:

$$\hbar\omega_0 \sim k_{\mathrm{B}}T. \tag{1.29}$$

As a result, a host of experiments have been suggested using nanomechanical resonators as quantum limited sensors[10], as quantum information processing elements[54], and as a platform to test quantum mechanics on macroscopic objects[55]. These experiments are discussed in more detail in Sec. 1.6.

1.5.3 Force sensitivity

As mechanical resonators become thinner and longer, they become more sensitive force detectors. A prime example of this is the AFM cantilever, which is typically 200 μm long and only 5 μm thick and as a result can sense forces of less than a nanonewton. In fact, one highly-engineered, very thin and long AFM cantilever currently holds the record for force sensitivity, 8.2×10^{-19} N/$\sqrt{\mathrm{Hz}}$[8]. Such force sensitivity is expected to improve even more as these systems are scaled down to the nanoscale.

Though a number of factors can limit force sensitivity (*e.g.* signal transduction technique), the ultimate limit on force sensitivity is the mechanical noise in the system. Here we assume that thermomechanical force noise is the limiting mechanical noise source[6].

---

[6]Even though the analysis in Sec. 1.4 showed that temperature fluctuations and field emission noise dominate in current nanotube resonators, we still consider thermomechanical noise the more fundamental limit for a number of reasons. Obviously, field emission noise can be eliminated simply by using an alternate

According to Eq. 1.19, thermomechanical force noise and thus force sensitivity scale as

$$F_{\min} = \sqrt{4k_{\mathrm{B}}Tm_{\mathrm{eff}}\Gamma} \propto \sqrt{\frac{r^3}{LQ}}. \tag{1.30}$$

Thus, for a given aspect ratio and a given Q, a thinner resonator is more sensitive. This holds true even if we assume that Q scales as the surface-to-volume ratio as suggested by Sec. 1.2.

Carbon nanotubes are perhaps the ultimate long, thin structure. They typically have aspect ratios on the order of 1000, and aspect ratios greater than one million have been reported[56]. From Eq. 1.30, we find that a typical nanotube could, if it were limited by thermomechanical noise, achieve a force sensitivity of $3.8 \times 10^{-20}\mathrm{N}/\sqrt{\mathrm{Hz}}$ at 100 mK, which is more sensitive than the current record[8]. However, our current nanotube resonators are limited by other noise sources, such as temperature fluctuations.

1.5.4 Mass sensitivity

As mechanical resonators become smaller, they become more sensitive to detecting changes in mass. Mechanical resonators, in general, have long been used to measure adsorbed mass through its effect on resonance frequency[1]. Nanomechanical resonators are particularly good mass sensors because they have a small effective mass and thus any additional mass has a significant effect. Moreover, their high resonance frequency makes it easy to detect shifts in frequency and also provides them with a high bandwidth.

To find the mass sensitivity, we multiply the frequency sensitivity, given by Eq.

---

signal transduction method. Temperature fluctuations, on the other hand, depend heavily on material properties and are only an issue in carbon nanotubes due to their high thermal conductance and speed of sound. Thus, for most nanomechanical resonators, thermomechanical noise ultimately limits the force sensitivity.

1.21, by $(d\omega_0/dm)^{-1} = 2m_0/\omega_0$. Thus, the mass sensitivity scales as

$$m_{\min} = \frac{2m_0}{\omega_0} \sqrt{\frac{k_{\mathrm{B}}T}{\frac{1}{2}m_{\mathrm{eff}}\omega_0^2 y_{\mathrm{c}}^2}\Gamma} \propto \sqrt{\frac{L^5}{rQ}}. \tag{1.31}$$

Here we assume that y_{c} scales as L, though the exact scaling depends on how β scales in Eq. 1.6. This is an extremely advantageous scaling for mass sensitivity with the size of the resonator.

1.6 Review of current nanomechanical resonators

Here we give a brief overview of the current state of nanomechanical resonator technology. First, we discuss the state-of-the-art nanomechanical resonator design. This includes the choice of materials, geometry, environment, and signal transduction method. Finally, we discuss important experiments and emerging applications of nanomechanical resonators.

1.6.1 Resonator design

Nanomechanical resonators have been fabricated from a variety of materials. A short list of these materials and resonator properties is shown in Tbl. 1.1. Here is a brief summary of the dominant material choices:

- Silicon is the default choice for nanomechanical resonators, mostly for historical and economic reasons. There is a wealth of information on the processing and electrical transport properties of silicon, which makes fabricating and analyzing these resonators much easier. Moreover, silicon resonators have the commercially enticing potential

to be incorporated with standard complementary metaloxidesemiconductor (CMOS) processing.

- Stressed silicon nitride is currently one of the most popular choices for high performance nanomechanical resonators. Due to their low intrinsic dissipation[21], a property which is still not well understood, these resonators hold the record for highest Q per unit volume, and thus they serve as exceptional sensors and filters.

- Gallium arsenide is an emerging option for "self-sensing" resonators, which utilize piezoelectric and piezoresistive properties to perform signal transduction[36]. However, this material lags behind others in terms of overall performance as is seen in Tbl. 1.1.

- Carbon nanotubes, and possibly other nanotubes such as boron-nitride nanotubes, are the obvious choice for high mass sensitivity. Though the quality factors of nanotube resonators are relatively low, their small size and low density makes their effective mass ($\sim 10^{-21}$ kg) more than four orders-of-magnitude smaller than lithographed resonators and even nanowire-based resonators ($\sim 10^{-17}$ kg) (see Tbl. 1.1). Thus, according to Eq. 1.31 for typical nanotube resonators, the minimum mass sensitivity should be 3.4×10^{-29} kg/$\sqrt{\text{Hz}}$.

After choice of material, the next consideration is the geometry of the resonator. The primary geometries for nanomechanical resonators are the singly clamped beam and doubly clamped (clamped at each end) beam. Each has its own advantages. Singly clamped beams have reduced clamping losses and a higher dynamic range (essentially how far the

resonator can bend before nonlinear effects dominate). On the other hand, doubly clamped beams allow certain signal transduction techniques such as magnetomotive detection and generally have higher resonance frequencies. Other geometries such as membrane resonators where a drum-like mode is excited[57] or disk resonators where the radial-breathing mode[58] is excited are being explored as well. These resonators have high quality factors and unique optical properties.

The environment in which the resonator operates is crucial. A high vacuum is ideal to avoid dissipation from viscous or acoustic losses to the surrounding gas and to avoid additional adsorption-desorption noise. Low temperatures help reduce thermoelastic dissipation and thermomechanical noise. Finally, tensioning the resonator significantly increases its quality factor[59], possibly through a reduction in inelastic clamping losses. This, in part, explains the success of stressed silicon nitride resonators[21, 57].

As discussed in Sec. 1.3, there are numerous techniques for signal transduction, each with its own advantages and disadvantages. Optical detection is the preferred technique for larger nanomechanical resonators[8, 21], though resonator technology is now reaching the point where this technique is limited by photon shot noise. Magnetomotive detection is the preferred technique for smaller resonators due to its strong signal, and it is often used in conjunction with other techniques as a means of initially finding the resonance[10]. The RF-SSET is the most sensitive technique, and has almost approached the quantum limits of position measurement[10]. Capacitive and piezoresistive techniques are the most likely to succeed in commercial applications because they operate at room temperature and do not require large magnetic or electric fields. Field emission detection is our preferred technique

because it is sensitive, works on cantilevered resonators, automatically adds tension to the resonator, and does not require tight tolerances during resonator fabrication.

1.6.2   Experiments and applications

The fundamental physics experiments involving nanomechanical resonators have focused on attempting to observe quantum effects in these devices. To this end, significant effort has been expended on cooling the resonators. Standard refrigeration technologies (*e.g.* dilution refrigeration) have been pushed to their limit, and thus alternate techniques are being explored. These alternate techniques may be classified as either feedback cooling or dynamical backaction cooling. With feedback cooling, the position of the resonator is monitored, and an appropriate counteracting force is applied to return the resonator to its neutral position, thus actively reducing the thermal vibrations. With dynamical backaction cooling, the same technique used in atomic laser cooling[60], an external device such as an RF circuit[61] or SSET[16] is coupled to the resonator such that it automatically applies a counteracting force to the resonator as a function of the resonator's position, again cooling the resonator but without the need for monitoring or active feedback. Notably, neither of these techniques cools all modes of the resonator; rather, only the fundamental mode is significantly cooled. The temperature of this modes is defined via the equipartition theorem as $T_{\mathrm{mode}} = k_{\mathrm{eff}} \langle y^2 \rangle / k_{\mathrm{B}}$. Feedback cooling has succeeded in cooling the fundamental mode of room temperature resonators all the way down to 670 mK and has cooled resonators starting out at lower temperatures down to 2.9 mK[52]. Similarly, backaction cooling has cooled resonators down to 6.8 mK[62]. Clearly, these temperatures are close to those where

quantum effects are predicted to have significant effects (see Eq. 1.29).

Once nanomechanical resonators are cooled near their ground state, it becomes possible to use them to explore the quantum limits of measurement. The most impressive experiments in this line of research have been the experiments by K. Schwab *et al.*, which have attempted to reach the quantum limit of position measurement[10]. Here, a nanomechanical resonator is capacitively coupled to the island of an RF-SSET. As the resonator vibrates, it modulates the island capacitance and thus the impedance of the SSET, which is monitored by RF reflectometry. Working backwards from the impedance of the SSET, it is possible to determine the position of the resonator. This technique allows the determination of the position of the resonator to within 4.3 times the quantum limit of position measurement, the closest this limit has been approached to date.

Another interesting experiment involves using cooled nanomechanical resonators as quantum information processing devices. In one proposal, a nanomechanical resonator is coupled to multiple Josephson junction phase qubits[54]. Quantum states initially encoded in eigenstates of the phase qubit can be transferred to and from the phonon-number states of a nanomechanical resonator. This system is similar to a more conventional approach to quantum computing involving atoms in an electromagnetic cavity[63]. Here the Josephson junctions function as artificial atoms, and the nanomechanical resonator serves as an artificial electromagnetic cavity. The main advantage of this approach is the ability to tune *in-situ* the energy levels of the "atoms" and the interaction strength of the "cavity."

In terms of practical applications, nanomechanical resonators are exceptional sensors for a variety of quantities as discussed in Sec. 1.5. In particular, nanomechanical

resonators are excellent sensors of adsorbed mass. With this sensitivity, it is possible to make nanomechanical sensors for proteins and viruses based on mass detection[64]. There has been significant effort to further increase the mass sensitivity of nanomechanical resonators, possibly to the point of creating a new form of mass spectrometer[65, 66, 67, 28, 29]. The current record for a lithographed nanomechanical resonator is 20×10^{-24} kg$/\sqrt{\text{Hz}}$. For any nanomechanical resonator, our nanotube-based devices hold the mass sensitivity record 0.13×10^{-24} kg$/\sqrt{\text{Hz}}$. This is sensitive enough to determine the mass of single gold atoms as we demonstrate in Ch. 4.

Nanomechanical resonators are also excellent force sensors, and as mentioned earlier hold the record for force sensitivity, 8.2×10^{-19}N$/\sqrt{\text{Hz}}$[8]. This incredible force sensitivity has allowed these resonators to measure the force between a single electron spin and a magnet. Using this technique, it is possible to image proteins using scanning nuclear magnetic resonance[68]. This force sensitivity also allows nanomechanical resonators to detect weak electric fields, which we use in Ch. 3 to receive radio signals.

The high quality factor and small size of nanomechanical resonators makes them attractive as RF signal processing elements. Already, nanomechanical resonators have been used as RF filters, mixers[69], amplifiers[70], and switches[71]. In Ch. 2, we develop a tuneable nanomechanical resonator with potential signal processing applications.

Table 1.1: Representative sample of nanomechanical resonators and their properties. Resonators are sorted in order of increasing effective mass. The minimum detectable force and mass are theoretical limits based on thermomechanical noise at room temperature.

Material	Geometry ($w \times t \times L$) [nm] × [nm] × [μm]	Clamps	m_{eff} [kg]	k_{eff} [N/m]	f_0 [MHz]	Q [#]	F_{min} [N/$\sqrt{\text{Hz}}$]	m_{min} [kg/$\sqrt{\text{Hz}}$]
DWNT[29]	$1.78 \times 1.78 \times 0.205$	single	3.79×10^{-22}	0.00161	328.5	3000	2.1×10^{-18}	3.4×10^{-29}
SWNT[6]	$2 \times 2 \times 1.750$	double	5.37×10^{-21}	0.000641	55	80	2.0×10^{-17}	1.3×10^{-27}
MWNT[45]	$10 \times 10 \times 0.500$	single	6.02×10^{-20}	0.155	251	440	6.0×10^{-17}	6.8×10^{-28}
Si nanowire[28]	$74 \times 74 \times 2.770$	double	2.34×10^{-17}	6.0	80.57	13100	1.2×10^{-16}	2.4×10^{-27}
3C-SiC[72]	$120 \times 75 \times 1.090$	double	4.34×10^{-17}	1814	1029	500	3.0×10^{-15}	9.5×10^{-28}
poly diamond[19]	$180 \times 40 \times 2.5$	double	4.63×10^{-17}	45.2	157.3	3000 [3]	5.0×10^{-16}	2.9×10^{-27}
GaAs[36]	$800 \times 200 \times 4$	single	8.14×10^{-16}	2.06	8	2700	5.0×10^{-16}	7.0×10^{-25}
low stress SiN[10]	$200 \times 100 \times 8$	double	9.70×10^{-16}	14.86	19.7	35000 [1]	2.4×10^{-16}	2.8×10^{-26}
AlN[73]	$200 \times 170 \times 3.9$	double	3.17×10^{-15}	85.4	82.585	21000	3.6×10^{-16}	4.9×10^{-27}
Silicon[2]	$800 \times 330 \times 7.7$	double	3.48×10^{-15}	687	70.72	18000	1.2×10^{-15}	1.1×10^{-26}
stressed Si$_3$N$_4$[21]	$350 \times 110 \times 275$	double	2.10×10^{-14}	0.928	1.058	1.1×10^6	4.6×10^{-17}	5.3×10^{-26}
Silicon[8]	$3900 \times 290 \times 260$	single	2.66×10^{-13}	2.6×10^{-4}	0.00498	150000 [2]	3.0×10^{-17}	1.7×10^{-21}

[1] at $T = 100$ mK
[2] at $T = 110$ mK
[3] at $T = 10$ K

Chapter 2

Tuneable nanotube resonator

One of the primary potential commercial applications of nanomechanical resonators is RF signal processing. This is already an enormous market for macroscopic mechanical resonators as they are commonly used as filters in cellular phones. However, these macroscopic resonators are currently a separate component from the rest of the purely electrical, usually single-chip RF transceiver. If the functions of a macroscopic mechanical resonator could be incorporated on-chip, perhaps using nanomechanical resonators, there would be enormous cost savings. One significant difficulty of incorporating nanomechanical resonators on-chip is developing a fabrication process compatible with current CMOS processing. Another difficulty is developing nanomechanical resonators with properties comparable to, or possibly superior to, macroscopic resonators.

Carbon nanotube-based nanomechanical resonators are a potential solution to these difficulties. First, they are compatible with CMOS processing[74]. Also, they have been proven to operate as mechanical filters from the kHz range all the way up to 3.8

GHz[5, 53]. They have potentially high quality factors[6]. And, because of their unique elec-trical properties, they have also been used as radio frequency amplifiers and mixers[45, 75] (see Ch. 3). However, current nanotube-based mechanical filters either operate at a single frequency or have a relatively narrow frequency range, possibly limiting their application.

Here we propose a fundamentally different nanotube-based nanomechanical res-onator, which takes advantage of one of carbon nanotubes' most interesting properties. Multi-walled carbon nanotubes (MWNTs), which consist of multiple, concentric nanotubes precisely nested within one another, exhibit a striking telescoping property whereby an inner nanotube core may slide within the atomically smooth casing of an outer nanotube shell[76]. This property has been exploited to build a rotational nanomotor[77] and a nanorheostat[78]. By harnessing this versatile telescoping property in a new fashion, we have created a tunable nanomechanical resonator operating at frequencies up to 300 MHz and tunable over a broad range of more than 100 MHz. Relatively high quality factors (up to 1000) indicate that sliding friction between telescoping sections of our resonator is an insignificant source of dissipation, and in fact the telescoping action may increase quality factors through the suppression of thermoelastic dissipation.

2.1 Experiment

Figure 2.1(A) is a schematic drawing of our tunable nanomechanical resonator. A MWNT is suspended between a metal electrode and a mobile, piezo-controlled contact. By peeling the outer shell of the MWNT[79] and exposing the inner core, we access its unique telescoping function. Like a trombone player shifting notes, we controllably slide
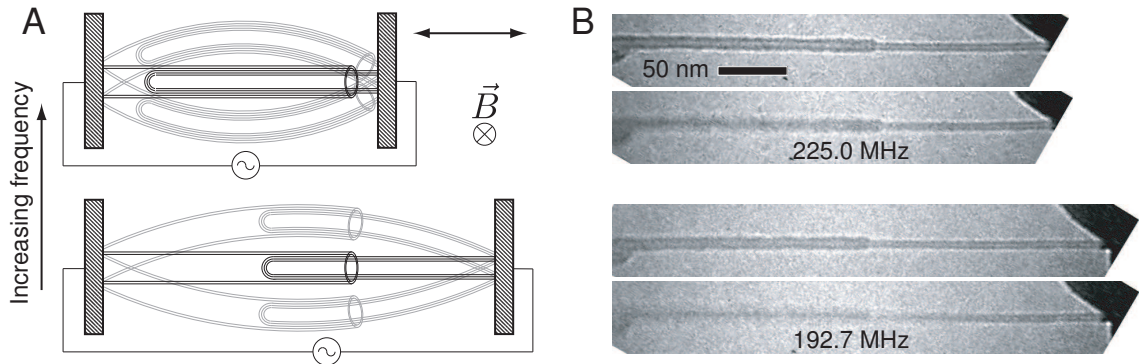
Figure 2.1: (A) Schematic drawing of our tunable resonator. A specially prepared MWNT is suspended between a stationary contact and mobile, piezo-controlled electrode. Varying the length of the nanotube beam through the controlled telescoping of the inner nanotube core from the outer nanotube shell tunes its resonance frequency. Operating the device in an external magnetic field, B, allows actuation with alternating current via the Lorentz force. (B) TEM micrographs show the device in action. The top two images show the nanotube at one extension off resonance (sharp) and on resonance (blurred) with a resonance frequency $f_0 = 225$ MHz. The bottom two images show an extended nanotube with a lowered resonance frequency (193 MHz).

the inner nanotube from its casing using the mobile contact, effectively changing the length of the MWNT and tuning its resonance frequency. In the top image, the resonator is fully retracted and has a relatively high resonance frequency. In the bottom image, the resonator is extended and consequently has a lower resonance frequency. By operating the device in an external magnetic field and applying an alternating electrical current through the MWNT, we can excite the mechanical vibrations of the nanotube via the Lorentz force[2]. With a TEM it is possible to detect these vibrations through the physical displacement of the nanotube.

Transmission electron micrographs in Fig. 2.1(B) show our tunable nanomechanical resonator in action. The first two images show a 558 nm long nanotube beam before resonance (sharp) and during resonance at 225 MHz (blurred). The final two images show
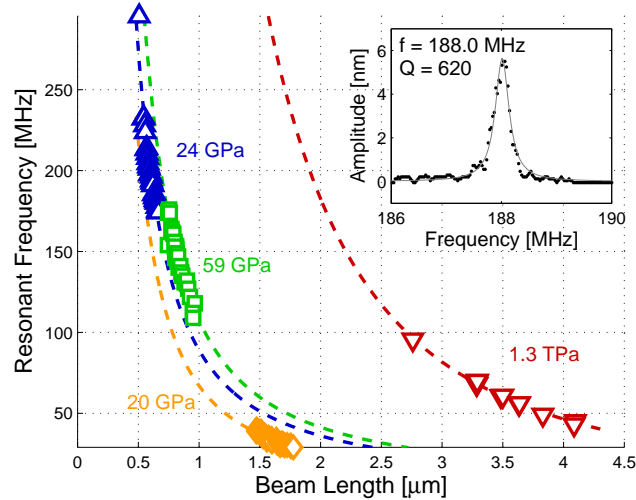
Figure 2.2: Tuning curves for four nanomechanical resonator devices. A theoretical model provides a good fit to the data and yields reasonable values for the effective Young's modulus of each device. The inset shows a typical resonance peak with a Lorentzian fit.

the nanotube beam after the inner nanotube has been telescoped out 50 nm. The resonance frequency has shifted downward to 193 MHz.

Resonance peaks are detected by analyzing video from the TEM with an image processing routine. The maximum displacement of the nanotube is calculated in each video frame. A Lorentzian is fit to the data to determine the resonance frequency and quality factor. The inset in Fig. 2.2 shows a typical resonance response of our nanomechanical resonator with a quality factor of 622. Note that measured quality factors may actually be up to 10% lower than intrinsic values due to inherent dissipation in our measurement apparatus caused by eddy currents created by vibrating the nanotube in a magnetic field[39]. Despite this fact, quality factors for our devices were generally between 100 and 1000, relatively high compared to other doubly-clamped nanotube resonators[6].

2.2 Analysis

2.2.1 Frequency shifts

To demonstrate our ability to tune the nanomechanical resonator, we plot resonance frequency versus beam extension for four devices in Fig. 2.2. As expected, extended nanotubes produce lower frequencies. Also, each device covers a relatively wide range of frequencies, and together the devices span nearly the entire spectrum from 30 MHz to 300 MHz. Apparent in the graph is the extreme sensitivity of resonance frequency to telescoping extension, more than 1 MHz/nm for one device, suggesting possible application as a precision distance/position sensor or strain gauge.

Euler-Bernoulli beam theory (see App. B) describes how frequency varies with beam extension. The nanotube beam is treated as a continuum, elastic medium subject to the differential equation:

$$\frac{\partial^2}{\partial x^2}\left(YI\frac{\partial^2 y}{\partial x^2}\right) - \frac{\partial}{\partial x}\left(T\frac{\partial y}{\partial x}\right) = -\rho A\frac{\partial^2 y}{\partial t^2} \tag{2.1}$$

where $y(x)$ is the transverse displacement of the beam along its length, Y is the Young's modulus, I is the areal moment of inertia, T is the tension, ρ is the density, and A is the cross-sectional area[80]. For a cylindrical beam with outer and inner radii, r_o and r_i, $I = \pi(r_o{}^4 - r_i{}^4)/4$. Strictly speaking our device is not a simple cylindrical beam but rather is more closely modeled as a combination of two cylindrical beams, the shell nanotube combination and the core nanotube combination. To simplify analysis, however, it is here modeled as a simple cylindrical beam with effective values of Y, I, ρ, A, r_o, and r_i which remain constant over the length of the beam and during operation. Applying the boundary

conditions of a doubly-clamped system with beam length, L, $(y(0) = 0, y'(0) = 0, y(L) = 0, y'(L) = 0)$ and solving the equation for the resonance frequency of the nth mode gives[80]

$$f_n \approx \frac{\beta_n{}^2}{2\pi L^2} \sqrt{\frac{YI + 0.024TL^2}{\rho A}}, \beta_n = 4.73, 7.85, 11.00, ... \tag{2.2}$$

Numerical solutions of Eq. 2.1 using the more complicated two-cylinder model indicate that this approximate solution is accurate to within one percent for typical devices.

Tension in our device is supplied by the van der Waals attraction between the core nanotube and the shell nanotube, $F_{\text{vdw}} = (0.2 \, \text{J/m}^2) \cdot C$, where C is the core nanotube's circumference[76]. Interestingly, as a result, tension remains constant regardless of extension, temperature, or other environmental factors, allowing robust and reproducible results.

Using Eq. 2.2, we fit curves to the experimental tuning data in Fig. 2.2. Only the Young's modulus and an offset to the length of the beam were used as fitting parameters. Due to our current fabrication techniques, some of our tunable nanomechanical resonators are composed of nanotube bundles rather than individual nanotubes resulting in lower values for the effective Young's modulus, which may vary from one device to another. Also, the exact location of the sample-side clamp is often obscured in TEM imaging requiring the usage of a length offset. The data follow the curves well and give reasonable values for the Young's modulus of a MWNT (1.3 TPa)[5] or MWNT bundles (20.3 GPa, 23.5 GPa, and 59.4 GPa)[81].
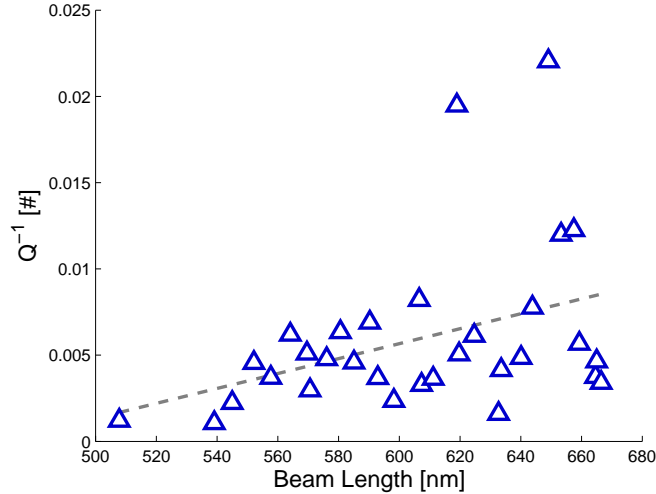
Figure 2.3: Dissipation as a function of nanotube beam length for one device. A linear regression shows a significant positive correlation.

2.2.2   Dissipation

As well as having many practical applications such as RF signal processing, our tunable nanomechanical resonator also provides an excellent platform for studying the physics of dissipation. Figure 2.3 is a plot of energy dissipation (Q^{-1}) as a function of extension for one device. There is a significant ($p = 0.03$) positive correlation between dissipation and extension. Possible dissipation mechanisms for nanomechanical resonators, most of which have been discussed in Ch. 1, include clamping loss, thermoelastic effects, core-shell sliding friction, and various irreversible processes involving surface defects and adsorbents. An additional dissipative effect known as eddy current damping results from operating the resonator in an external magnetic field. Eddy current damping[39], though it would exhibit a positive correlation with extension, cannot account for the magnitude of the increase in dissipation. Both clamping loss and thermoelastic dissipation are expected

to decrease as length increases, opposite to what is observed[82]. Moreover, thermoelastic dissipation is likely greatly suppressed because the nanotube may telescope to increase its length rather than stretch. Sliding friction could depend on overlap length between the core nanotube and shell nanotube; however again, dissipation would likely decrease with increased extension because there would be less overlap[83]. Surface losses therefore remain the most likely candidate for the dominant form of dissipation here. This important size-dependent contributor to dissipation has been suspected in other nanoscale oscillators[84].

Surface losses are typically modeled through the addition of a thin dissipative layer to the resonator's surface. Though our experiments were conducted in high vacuum (10^{-7} torr), the surface of the nanotube, even the newly exposed portion following telescoping, is likely covered with more than a monolayer of adsorbents, which functions as the dissipative layer. Dissipation, defined as the inverse of the quality factor, is given by: $Q^{-1} = \Delta U / 2\pi U_0$, where ΔU is the energy lost per cycle and U_0 is the energy originally stored in the resonator. Stored energy is related to total resonator volume while energy lost per cycle is related to the volume of the dissipative surface layer, resulting in dissipation proportional to the surface-to-volume ratio. Thus, in most nanomechanical resonators, dissipation is inversely proportional to length[18]. Curiously, in our nanomechanical resonator, the actual volume of the resonator remains constant during extension giving a dissipation that is directly proportional to length, $Q^{-1} \propto S/V \propto L$.

2.3   Discussion

Our unique high-Q tunable nanomechanical resonator exhibits promise as a precise mass, force, position, or frequency sensor. It has demonstrated a wider frequency range than competing tunable nanomechanical resonator designs. Also, its unique sliding ability lends itself to position sensing applications unlike other immobile resonators. Finally, its nearly perfect atomic structure and precisely controlled geometry make it an ideal tool to study the physics of dissipation.

Chapter 3

Nanotube radio

Radio communication has had a profound effect on civilization. Within a decade of the experimental discovery of electromagnetic waves in 1888 by Hertz, radio was used for critical communications, for example with ships at sea. By the 1930s, it had achieved mass popularity, with more than 50 million listeners, as a medium for music and news[85]. Today, radio remains a widely used communications medium that underlies modern technologies such as cellular phones, wireless computer networks, and the global positioning system.

Throughout its history, potential applications for radio have been tightly linked to available technology. The earliest spark-gap transmitters and receivers were large, dangerous, and only capable of transmitting on/off signals such as Morse code. Later, the vacuum tube enabled cheap, reliable audio communication, thus heralding the "golden age" of radio in the 1930s. Perhaps most strikingly, the solid-state transistor transformed the radio from a bulky, power-hungry, and stationary unit to a device that could be carried in a shirt-pocket. Development continues today with technologies such as microstrip antennas[86] and digital

signal processing which again are creating new applications.

Conventional radio technologies, however, are now approaching fundamental limits. In particular, transistors, as created by optical lithography, are approaching their theoretical size limit. These hard physical limits suggest that new nanoscale materials will soon be needed to complement or even replace silicon-based architectures[87]. Indeed, carbon nanotubes have emerged as potential alternatives for a variety of electronic devices including diodes[88], transistors[89, 90], and sensors[91, 92], and also electromechanical systems including nanoscale motors[77] and mechanical resonators[6]. Recently, small-scale integrated circuits such as ring oscillators have been fabricated using single nanotubes[74]. Continuing this trend, we have fabricated a fully-functional radio, orders-of-magnitude smaller than previous radios, from a single carbon nanotube.

The functioning of our nanotube radio depends on the remarkable mechanical and electrical properties of carbon nanotubes[6, 5, 93]. In particular, it relies on their high elastic modulus[94], low mass density, sharp mechanical resonance peak, large aspect ratio, and ability to carry large currents without degradation[95].

3.1 Nanotube radio design

3.1.1 Envelope detector radio receivers

To understand how the nanotube radio receiver operates, it is instructive to examine how radio receivers work in general, specifically envelope detector radio receivers. These radios consist of four essential components: antenna, tuner, amplifier, and demodulator, all shown in the dashed box in the block diagram in Fig. 3.1.

All-in-one nanotube radio
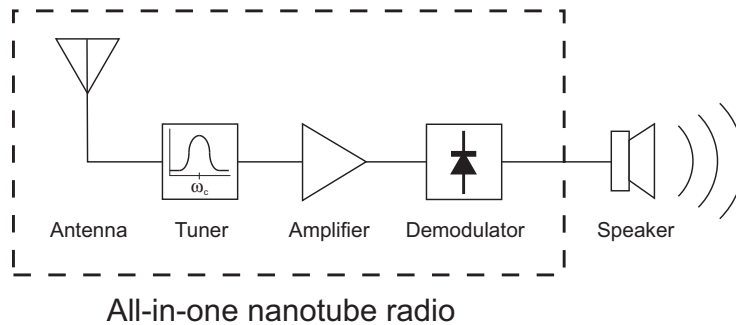
Figure 3.1: Block diagram for a traditional radio. All four essential components of a radio, antenna, tuner, amplifier, and demodulator, may be implemented with a single carbon nanotube.

The antenna receives the incoming radio transmissions. The tuner then filters this received signal, selecting a frequency range or channel of interest. The amplifier increases the generally weak radio signal power to a more robust level. Finally, the demodulator, typically a nonlinear device like a diode, extracts from the incoming modulated, high frequency radio signal the lower frequency informational signal which, depending on application, can either be directly amplified and sent to an audio loudspeaker (as shown in the remainder of the block diagram in Fig. 3.1) or further processed by a computer or other instrument.

3.1.2   Nanotube radio schematics

Amazingly, all four critical radio receiver components can be simultaneously implemented with a single carbon nanotube. A schematic of the nanotube radio is shown in Fig. 3.2. A model of simplicity, the entire radio consists of an individual carbon nanotube mounted to an electrode, in close proximity to a counter electrode. A DC voltage source, such as from a battery, is connected to the electrodes and powers the radio. Importantly for the radio's operation, the applied DC bias negatively charges the tip of the nanotube,
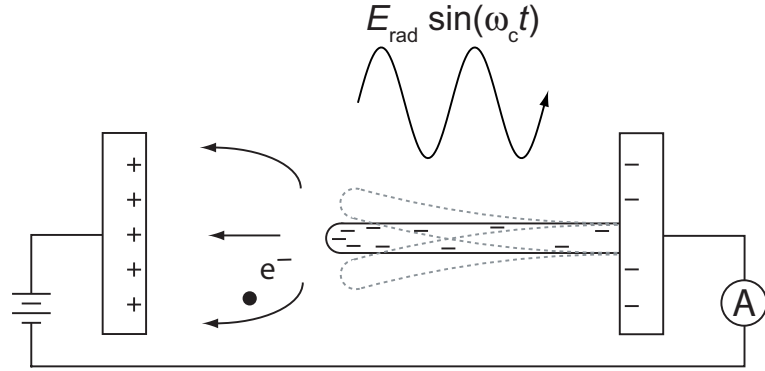
Figure 3.2: Schematic of the nanotube radio. Radio transmissions tuned to the nanotube's resonance frequency force the charged nanotube to vibrate. Field emission of electrons from the tip of the nanotube is used to detect the vibrations and also amplify and demodulate the signal. A current measuring device, such a sensitive speaker, monitors the output of the radio.

sensitizing it to oscillating electric fields. Also, both electrodes and nanotube are contained in vacuum, typically below 10^{-7} torr. Interestingly, this geometrical configuration is reminiscent of a conventional vacuum tube, and indeed there are some key functional similarities between the two.

3.1.3 Antenna

The antenna is implemented by the charged tip of the nanotube, which directly responds to the induced force from the incoming radio wave. This is substantially different than other proposals which use nanotubes as scaled-down versions of macroscopic antennas[96, 97]. The quantity of charge at the tip, which is critical to the performance of the antenna, is[47]

$$q = 4\pi\epsilon_0 E_{\text{ext}} hr \left(1 + \frac{r}{2h}\right) \tag{3.1}$$

where h is the height of the tip of the nanotube over the electrode and r is the radius of the tip of the nanotube. Accordingly, nanotubes of similar sizes and under similar conditions to the ones used in this experiment ($L \approx 500$ nm, $r \approx 5$ nm, $E_{ext} \approx 10^8$ V/m) accumulate approximately 3×10^{-17} C of charge (almost 200 unbalanced electrons) at their tips[47].

In a typical metal-wire antenna, the incoming electromagnetic wave induces an oscillating current in the wire. In our radio, the incoming wave forces the charged-tip of the nanotube to mechanically oscillate up-and-down. The mechanically oscillating charge on the nanotube tip acts as an extremely small dipole antenna. Interestingly, the effective area of a small dipole antenna (*i.e.* the area it presents to the incoming electromagnetic radiation) is independent of the size of the antenna and only depends on the wavelength of the received radiation, impedance matching to the receiver, and the quality factor of the antenna. Thus, despite its extremely small size, this nanotube antenna could, in principal, collect radiation over a relatively large area.

3.1.4   Tuneable band-pass filter

The tuner filters radio signals through the nanotube's flexural resonance frequency. According to classical Euler-Bernoulli beam theory, the resonance frequency of a can-tilevered nanotube is $f_0 = \frac{0.56}{L^2}\sqrt{\frac{YI}{\rho A}}$, where L is the length of the nanotube, Y is the Young's modulus, I is the areal moment of inertia ($\pi(r_o{}^4 - r_i{}^4)/4$ for a cylinder with outer and inner radii r_o, r_i), ρ is the density, and A is the cross-sectional area[33]. Typical nan-otubes used in our experiments had resonance frequencies from 10 to 400 MHz, lying in a commercially relevant portion of the spectrum including FM radio. The bandwidth of the

filter is determined by the quality factor of the nanotube resonators, typically around 500 (see Fig. 3.6(B)).

3.1.5   Sensitivity

By combining theoretical results for the antenna and tuner, it is possible to determine the sensitivity of the nanotube radio to incoming electromagnetic waves. The amplitude of the vibrations of the tip of the nanotube is given by the familiar equation:

$$|y| = \frac{qE_{\mathrm{rad}}/m_{\mathrm{eff}}}{\sqrt{(\omega^2 - \omega_0{}^2)^2 + (\omega\omega_0{}^2/Q)^2}} \tag{3.2}$$

where q is the charge on the tip, E_{rad} is the amplitude of the electric field of the incoming transmission, $m_{\mathrm{eff}} \approx 0.24m$ is the effective mass of the nanotube determined from Euler-Bernoulli theory, and Q is the quality factor. This amplitude may be compared to the thermal vibrations of the nanotube, which ultimately limit the sensitivity of the single nanotube radio. The minimum detectable electric field amplitude while maintaining a bandwidth B is $E_{\mathrm{rad}} = \frac{1}{q}\sqrt{4k_{\mathrm{B}}Tm_{\mathrm{eff}}\omega_0 B/Q}$, which for our experiments was typically 1 V/m/$\sqrt{\mathrm{Hz}}$ or equivalently 60 dBmV/m/$\sqrt{\mathrm{Hz}}$[4]. The nanotube radio's sensitivity can be enhanced by operating at reduced temperature, using a lower resonance frequency, or improving the Q of the oscillating nanotube. Other modifications include attaching an external antenna, or, in the interest of preserving the overall small size of the receiver system, using multiple nanotubes all tuned to the same frequency.
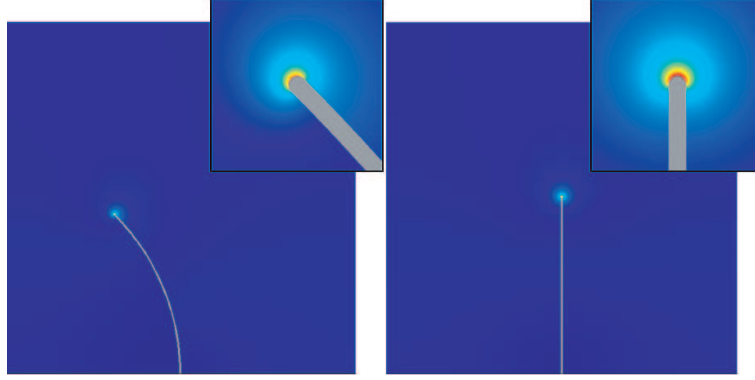
Figure 3.3: Simulations of the electric field amplitude surrounding the nanotube when it is bent (left) and straight (right)

3.1.6 Amplifier and Demodulator

The amplification and demodulation stages rely on the remarkable field-emission properties of carbon nanotubes, which are due in large part to their needle-point geometry which concentrates the electric field[93]. The DC bias voltage applied across the electrodes in Fig. 3.2(A) produces a nominally constant field-emission current. Mechanical vibrations of the nanotube modulate the field-emission current[44], which then serves as the easily detected electrical signal. Because the battery voltage source, rather than the incoming electromagnetic wave, powers the field-emission current, amplification of the radio signal is possible. Also, due to nonlinearities inherent in field-emission, demodulation of the radio signal occurs as well.

The field emission current, I, from a carbon nanotube is well described by the Fowler-Nordheim law[46]:

$$I = c_1 A (\gamma E_{\text{ext}})^2 \exp\left(-\frac{c_2}{\gamma E_{\text{ext}}}\right) \tag{3.3}$$

where A is the area from which the nanotube emits, E_{ext} is the external applied electric

field, and γ is the local field enhancement factor. The constants c_1 and c_2, which involve

only fundamental constants and the nanotube's work function, take the values 3.4×10^{-5}

A/V^2 and 7.0×10^{10} V/m, respectively. The field enhancement factor, a measure of the

concentration of the local electric field by the nanotube's geometry, distinguishes carbon

nanotubes as excellent field emitters and also plays a critical role in the operation of the

nanotube radio. To a good approximation, the field enhancement factor for a nanotube is

$\gamma \approx 3.5 + h/r$, where h is the height of the tip of the nanotube above the cathode and r

is the radius of the nanotube[47]. As the nanotube vibrates, the height of its tip oscillates

resulting in a time-varying field enhancement factor: $\gamma(t) = \gamma_0 + \Delta\gamma(t)$.

The response of the field emission current to the vibrations is determined by sub-

stituting $\gamma_0 + \Delta\gamma(t)$ for γ in Eq. 3.3. Expanding to second order in powers of $\Delta\gamma(t)/\gamma_0$

and filtering out the zeroth and first powers of $\Delta\gamma(t)/\gamma_0$, which correspond to DC and RF

terms, yields

$$\Delta I(t) = I_0 \left(1 + \alpha + \frac{\alpha^2}{2}\right) \left(\frac{\Delta\gamma(t)}{\gamma_0}\right)^2; \quad \alpha = \frac{c_2}{\gamma_0 E_{\text{ext}}} \tag{3.4}$$

which accounts for both amplification and demodulation. Amplification occurs because the

output of the radio, $\Delta I(t)$, is proportional to the field emission current, I_0, which is powered

by the battery voltage source. The power gain, given by the ratio of the power dissipated

by the signal current through a load resistor, $P_{\text{out}} = \Delta I_{\text{rms}}^2 R_L$, to the power absorbed

by the nanotube from a radio signal on resonance, $P_{\text{in}} = m_{\text{eff}}\omega_0^3|y|^2/2Q$, was typically on

the order of 50 dB in these experiments, though it is easily adjustable over a wide range.

Demodulation occurs because $\Delta I(t)$ is proportional to the square of the input signal $\Delta\gamma(t)$,

effectively mixing the input signal with itself. In this manner, a field-emitting nanotube

operates similarly to standard diode detectors.

Thus, all four essential components of a radio receiver are compactly and efficiently implemented by the vibrating and field-emitting nanotube.

3.2 Nanotube radio operation

3.2.1 Receiving a signal

Now that we have described the theory behind the nanotube radio's operation, we demonstrate it in action. Because of the critical role played by mechanical motion of the nanotube during radio operation, visual observation of the nanotube radio is invaluable. We accomplished this by mounting the nanotube radio inside a high resolution TEM. A sine-wave carrier radio signal (generated for screening reasons inside the TEM) was launched from a nearby transmitting antenna. Figure 3.4 shows TEM micrographs of the nanotube attached to the cathode (the anode is not shown as it is more than one micron off the image toward the left). In the upper image, the nanotube resonance frequency does not match the transmitted carrier wave frequency; the nanotube is relatively motionless and no radio reception can occur. Apparent in this image is the negative charging of the tip of the nanotube, which manifests itself as a significant brightening toward the nanotube's tip[98]. In the lower image, the nanotube's resonance frequency has been brought into tune with the transmission carrier wave frequency (251 MHz). Here the oscillating electric field of the radio signal resonantly drives the charged nanotube, causing it to vibrate vigorously thereby blurring its image[5]. During this resonance condition, radio reception is possible.

To correlate the mechanical motion of the nanotube to actual radio receiver oper-
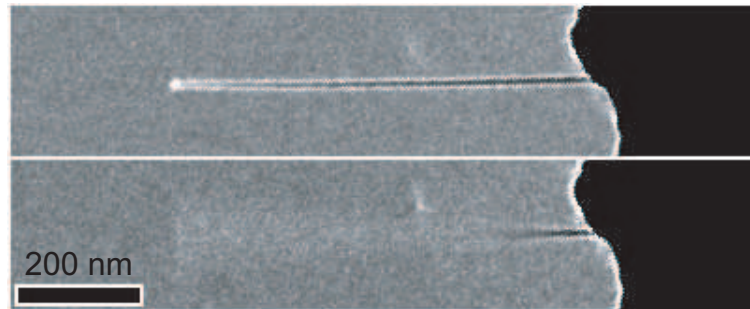
Figure 3.4: Transmission electron micrographs of a nanotube radio off and on resonance during a radio transmission.

ation, we launched a frequency modulated (FM) radio transmission (amplitude modulated (AM) signals work as well) of the song *Good Vibrations* by the Beach Boys. After being received, filtered, amplified, and demodulated all by the nanotube radio, the emerging signal was further amplified by a current preamplifier and sent to an audio loudspeaker and recorded. The upper portion of Fig. 3.5 shows the frequency spectrum and audio waveform of a two second segment of the song as transmitted, while the lower portion of the same figure shows the same segment as received by the radio. The nanotube radio faithfully reproduces the audio signal, and the song is easily recognizable by ear. As a test, during operation we purposely detuned the nanotube from the carrier frequency, and, as expected, whenever mechanical resonance was lost, so was radio reception. We found it straightforward, even without active feedback, to maintain "lock" on a given radio transmission channel for many minutes at a time.

Though the audio delivered by the nanotube radio is quite good and the song is easily recognizable by ear, some distortions are evident. First, in the received audio waveform some "spikes" are visible near 0.3 s, 1.6 s, and 1.7 s. These are a result of "burst noise" in the field emission current where the current suddenly switches between
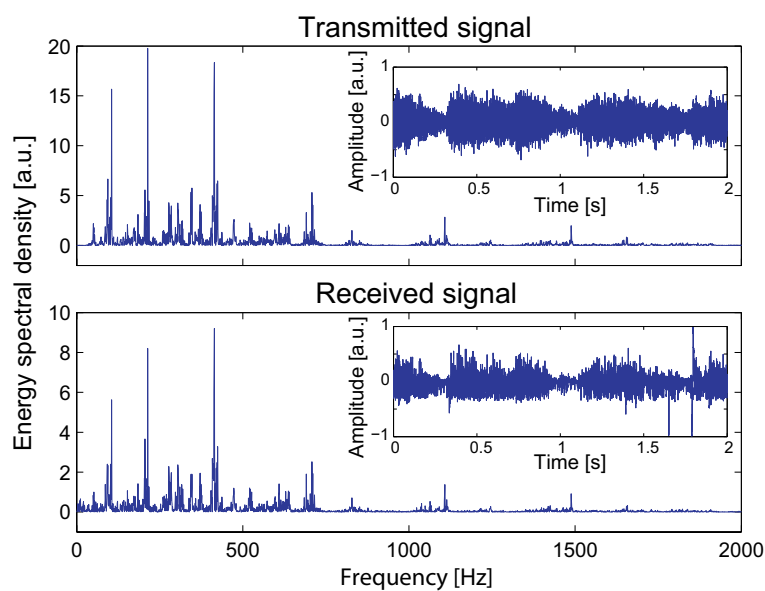
Figure 3.5: Transmitted and received audio waveforms (inset) and frequency spectra of two seconds of the song *Good Vibrations* by the Beach Boys. The nanotube radio faithfully reproduces the audio signal, and indeed the song is easily recognizable by ear.

multiple stable states. Burst noise occurs when molecules adsorb or desorb from the field emission surface greatly altering the field emission current via resonance tunneling states[99]. Fortunately, this noise source can be eliminated by operating in ultrahigh vacuum. Second, the amplitude of the audio waveform output appears to be limited on the negative half. This results from setting the center frequency of the radio transmission near the edge of the resonance peak of the nanotube. To function as an FM receiver, the nanotube radio uses "slope detection," which converts the FM signal to an AM signal though filtering with the nanotube's sharp resonance peak. Operating near the edge of the nanotube resonance introduces nonlinearity into this conversion. This distortion can be controlled by using a smaller FM deviation.

3.2.2 Tuning

The resonance frequency of the nanotube radio is tuned using a two-step process. An initial "coarse" tuning adjustment sets the operational frequency band by trimming, or shortening, the length of the nanotube. To accomplish this, a high field-emission current, much higher than used for radio operation, is run through the nanotube, and as a result, carbon atoms are ejected from the end of the nanotube, permanently altering its length[100]. The trimming process is terminated once the nanotube's resonance frequency reaches the target frequency band. Figure 3.6(A) demonstrates coarse tuning of a nanotube radio from a lower frequency FM radio band (around 100 MHz) to much higher frequency bands (up to 350 MHz) reserved for applications such as television or emergency services.

Fine tuning of the radio within the desired band is accomplished by tensioning the nanotube with an electrostatic field[44]. Thus, much as a guitar is tuned by tensioning its strings, the nanotube's resonance frequency is tuned (over several megahertz) through small adjustments to the already established dc bias voltage. Figure 3.6(B) demonstrates fully reversible fine tuning of a nanotube's resonance frequency during radio operation.

3.3 Applications

The nanotube radio's primary advantage over previous radio receivers is, of course, its size. A typical volume for the active element (*i.e.* the nanotube) is only 3.9×10^4 nm^3. This is small enough to travel in the human bloodstream or even fit within a single cell. Thus, a host of new biomedical applications are possible. For example, it may be possible to place radio-controlled medical devices in the bloodstream to perform diagnosis or to control
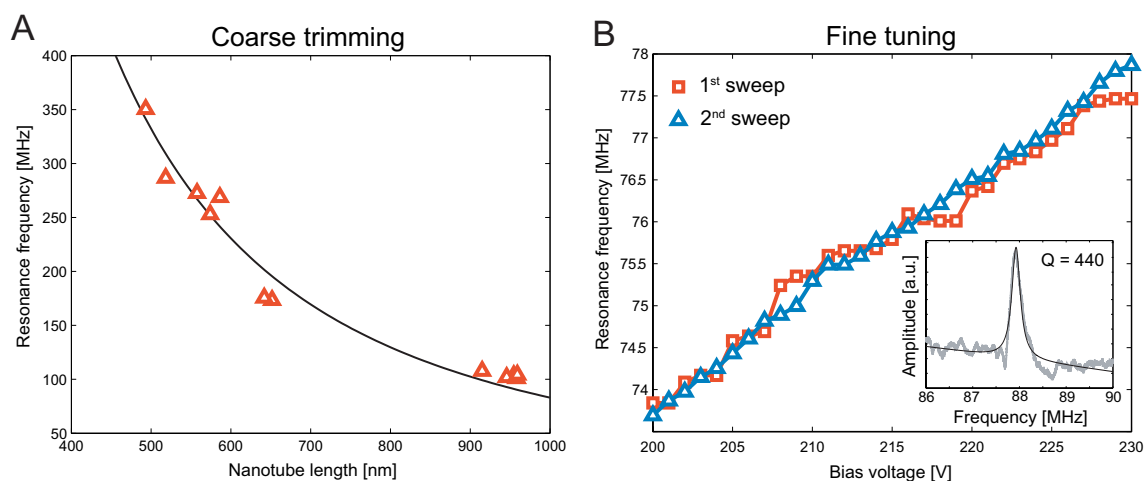
Figure 3.6: Demonstration of coarse and fine methods for adjusting the center frequency of the nanotube radio's tuner. (A) During coarse tuning, or "trimming," the nanotube is controllably shortened, thus increasing its resonance frequency. Its resonance frequency closely follows the $1/L^2$ dependence predicted by Euler-Bernoulli beam theory. (B) During fine tuning, a bias voltage is used to adjust tension on the nanotube. Multiple sweeps of the bias voltage demonstrate the reversibility of the process. Inset is a typical resonance peak with a Lorentzian fit.

drug delivery. Other potential applications for nanoscale radios include "smart dust"[101], enhanced radio frequency identification tags, or simply smaller, cheaper wireless devices such as cellular phones.

Besides its small size, the nanotube radio has numerous other advantages. As it is chemically inert, it can operate in a variety of chemical environments. Also, as it is partially composed of mechanical elements, the nanotube radio is naturally radiation hardened and can operate in the presence of severe ionizing radiation (*e.g.* in space). Finally, because many nanotube radios, each with a different resonance frequency, can be incorporated on the same chip, it is possible to make extremely broad bandwidth devices.

Chapter 4

Atomic-resolution nanomechanical

mass sensor

The concept of using mechanical resonators to measure inertial mass is as old as Newton's second law ($F = ma$). One simply attaches a mass to a spring and sets the system into motion. From the frequency of oscillations, it is possible to infer the system's mass. Such inertial balances have long been used to measure mass, and in some cases, for example in space[102] or for thin-film deposition[1], they are the preferred means of measurement.

As described in Ch. 1, inertial balances become increasingly sensitive to adsorbed mass as their size decreases. Specifically, the minimum detectable mass scales according to the following relation:

$$m_{\min} = \frac{2m_0}{\omega_0} \sqrt{\frac{k_{\mathrm{B}}T}{\frac{1}{2}m_{\mathrm{eff}}\omega_0{}^2 y_{\mathrm{c}}{}^2}} \Gamma \propto \sqrt{\frac{L^5}{rQ}}. \tag{4.1}$$

As a result of this advantageous scaling, Ekinci *et al.* noted that nanomechanical resonators,

operating as scaled down inertial balances, might one day serve as a new form of mass spectrometer[11]. Since then, there has been a steady push to reach this atomic mass limit[65, 66, 67, 28]. Here, we demonstrate an atomic resolution nanomechanical mass sensor constructed from a carbon nanotube, thus realizing a new form of mass spectrometer. The atomic sensitivity of our device is demonstrated by measuring the mass of a single *neutral* gold atom.

The extreme sensitivity of our device has also allowed the first observation of atomic mass shot noise. This effect is analogous to electronic shot noise, the random fluctuations in current resulting from the statistical nature of the arrival of discrete quantities of charge, corresponding to the electron's charge. First predicted by Schottky in 1918[103], this effect was used shortly thereafter to measure the charge of an electron[104]. Similarly, we use this technique to measure the discrete unit of mass, the mass of a single atom.

4.1 Resonator responsivity

The fundamental equation governing nanomechanical mass sensors is the relation between their change in mass, due to an adsorbed particle, and the consequent shift in mechanical resonance frequency. In general, this relation depends on the geometry of the resonator and the location of the adsorbed particle. For a cantilevered beam resonator, we describe this relation through a responsivity function, $R(x)$, defined as the ratio of the shift in resonance frequency, Δf, to the change in mass, Δm, as a function of position, x, of the adsorbed mass along the beam.

To determine the responsivity function, we first calculate the resonance frequency

of the beam as a function of adsorbed mass using the Rayleigh-Ritz method (see App.

B). An atom with mass, m_i, landing at position, x_i, along the cantilever is modeled as

a local modification of the beam's density, $\rho(x) = \rho_0 + m_i \delta(x_i)/A$. Here we assume that

the adsorbed mass has negligible effect on the resonator's strain energy and mode shape.

Following the procedure outlined in App. B, we calculate the resonance frequency for the

fundamental mode of a cantilever with adsorbed masses:

$$\omega_0 \approx \sqrt{\frac{3YI/L^3}{0.24\left(\rho_0 AL + \Sigma_i w(x_i) m_i\right)}}. \tag{4.2}$$

In the process, we arrive at a weighting function, $w(x)$, for the relative effect of masses at

different positions:

$$w(x) = \frac{L\,y_0{}^2(x)}{\int_0^L dx\,y_0{}^2(x)} \tag{4.3}$$

where $y_0(x)$ is the mode shape of the beam.

This weighting function figures prominently in the responsivity function of a can-

tilever. From Eq. 4.2 and Eq. 4.3, the responsivity of the cantilever is

$$R(x) = \frac{1}{2\pi}\frac{d\omega_0}{dm} \approx -\frac{f_0}{2m_0}w(x) \tag{4.4}$$

where f_0 and m_0 are the initial resonance frequency and mass of the cantilever. Figure

4.1 shows the form of the approximate responsivity function. The axes are normalized for

a resonator of unit length and unit averaged responsivity. The maximum frequency shift

is a factor of approximately four times the average frequency shift. However, most atoms

produce relatively small frequency shifts.

In our current experiment, we do not control or observe the position of the adsorbed

mass. Rather, the mass is deposited randomly along the length of the resonator. Thus, for
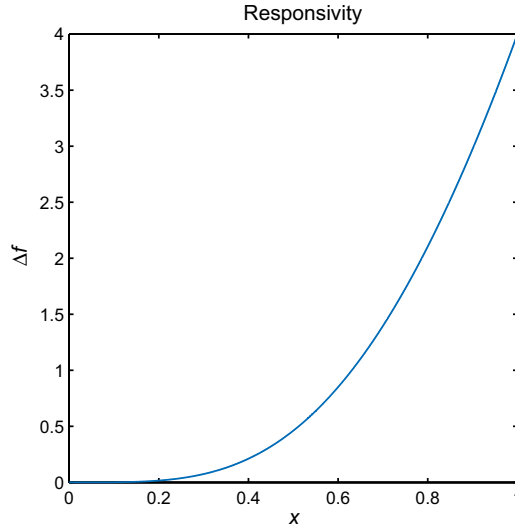
Figure 4.1: Responsivity of a cantilever of unit length normalized to a unit mean frequency shift. Atoms landing near the base of the cantilever cause minimal frequency shifts, while atoms landing near the tip cause a shift of approximately four times the mean.

our purposes, an averaged responsivity function is more appropriate. Integrating Eq. 4.4 over the length of the cantilever yields the averaged responsivity function:

$$\overline{R(x)} = \frac{1}{L} \int_0^L dx R(x) = -\frac{f_0}{2m_0}. \tag{4.5}$$

4.2 Design considerations

Determining the mass of single atoms with an inertial balance is a formidable task, and thus it is important to optimize all parameters of our system. Our nanomechanical mass sensor has two notable advantages over previous attempts at precision mass sensing: material choice and clamping geometry.

In terms of material choice, ours is the first system to specifically use double-walled carbon nanotubes. In order to maximize the magnitude of the responsivity, it is apparent from Eq. 4.5 that reducing the mass of the resonator, while maintaining high

resonance frequencies, is critical. Carbon nanotubes are ideally suited for this task. They are naturally much smaller and less dense than resonators manufactured using standard e-beam lithographic techniques, and thus their mass ($\sim 10^{-21}$ kg) is typically more than four orders-of-magnitude less than state-of-the-art micromachined resonators ($\sim 10^{-17}$ kg) (see Tbl. 1.1). Also, because of their high elastic modulus[94], even small, slender nanotubes maintain high resonance frequencies. Finally, the uniform electrical properties of double-walled carbon nanotubes (*i.e.* mostly metallic) afford simple and reproducible electrical readout.

In terms of clamping geometry, ours is the first mass sensor of its size scale to be singly clamped. Many previous attempts at precision mass sensing have focused on doubly clamped geometries[65, 67, 28] to allow simple electrical readout. Singly clamped geometries, however, have notable advantages. Their dynamic range, essentially how far they can bend before non-linear effects dominate, is significantly increased. Also, singly clamped resonators tend to have higher quality factors (*i.e.* sharper resonance peaks) due to reduced clamping losses[33]. Both dynamic range and quality factor are important in determining a resonator's ultimate sensitivity[11].

4.3   Experiment

A TEM image of a typical nanotube-based nanomechanical mass sensor is shown in Fig. 4.2(A). The entire device consists of a single arc-grown double-walled nanotube[105] attached to one electrode in close proximity to a counter electrode (not shown). Fabrication of these devices is described in detail in previous work[106].
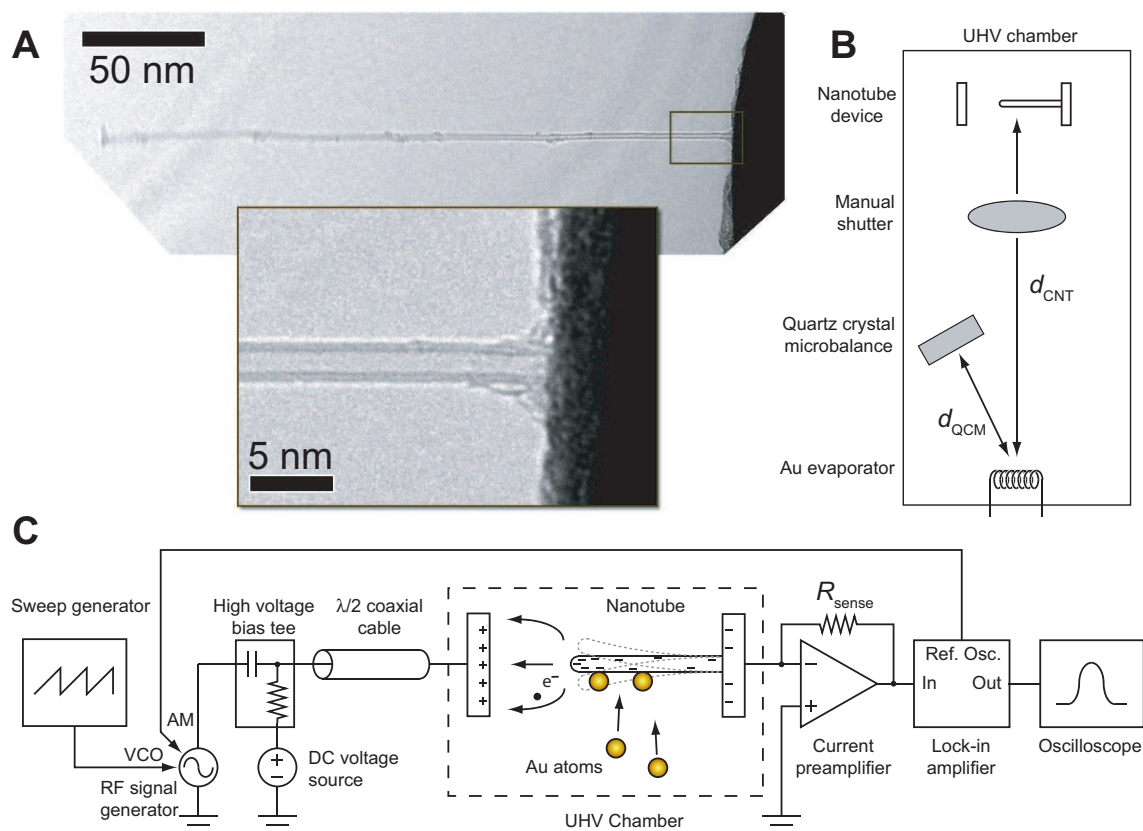
Figure 4.2: (A) TEM images of a nanomechanical mass sensor constructed from a double-walled carbon nanotube. From these high resolution TEM images, the geometry and thus mass of the nanotube are precisely determined ($m_{\mathrm{CNT}} = 2.33 \times 10^{-21}$ kg), which is an essential calibration for the mass sensor. (B) Physical layout of the entire nanomechanical mass sensor apparatus. Gold atoms are evaporated, inside a UHV chamber, and travel a distance d_{CNT} before adsorbing to the nanotube device and consequently lowering its resonance frequency. A shutter may be inserted to interrupt mass loading. The QCM provides an alternate means of calibrating the system through measurement of mass flux. (C) Schematic of the mechanical resonance detection circuit. Briefly, the electrode opposite the nanotube is biased to induce a field emission current from the nanotube. A modulated, frequency-swept RF signal is coupled to the nanotube forcing it into resonance, and consequently modulating the field emission current. The modulated field emission current is recovered by a lock-in amplifier and the resonance peak is displayed on the oscilloscope or recorded by a computer.

These high resolution TEM images enable precision calibration of our devices through determination of their exact size and thus mass. A double-walled nanotube's mass is simply $m_{CNT} = 2m_C\pi(D_i + D_o)L/A_{gr}$ where m_C is the mass of a carbon atom, D_i and D_o are the inner and outer shell diameters, L is the length, and A_{gr} is the area of graphene's unit cell. For the device shown in Fig. 4.2(A) ($D_i = 1.75$ nm, $D_o = 2.09$ nm, $L = 254$ nm), $m_{CNT} = 2.33 \times 10^{-21}$ kg.

The physical layout of the entire nanomechanical mass sensor apparatus, including nanotube device and evaporation system, is shown in Fig. 4.2(B). The nanotube device is placed at one end of an ultra-high vacuum (UHV) chamber (10^{-10} torr). To load atoms onto the device, we evaporate gold from a tungsten filament a distance $d_{CNT} = 50.2$ cm away from the nanotube device. A shutter may be inserted between the evaporation source and the nanotube to interrupt the gold mass loading. A water-cooled quartz crystal microbalance (QCM), a distance $d_{QCM} = 12.8$ cm from the evaporation source and normal to the direction of evaporation, is used as a secondary means of calibrating the nanotube device.

One difficulty of using nanomechanical resonators as precision sensors is the detection of the mechanical vibrations of the resonator. We use a detection technique based on a nanotube radio receiver design[45]. In effect, we broadcast a radio signal to the nanotube and listen for its vibrations. This technique relies on the unique field emission properties of carbon nanotubes[93], one of which is a strong coupling between the field emission current and the nanotube's mechanical vibrations. A schematic for the electrical detection circuit is shown in Fig. 4.2(C).

A field emission current is induced by positively biasing the electrode opposite the

nanotube. Then a radio frequency (RF) signal, with carrier frequency near the mechanical resonance frequency of the nanotube, is launched toward the nanotube. The carrier frequency is systematically swept through a range of a few megahertz in order to track shifts in the nanotube's resonance frequency. At the same time, the signal is amplitude modulated (AM) at a low frequency by the reference oscillator in the lock-in amplifier. When the carrier frequency matches the nanotube's resonance frequency, the vibrating, field-emitting nanotube demodulates the AM radio signal. The low-noise current preamplifer amplifies the demodulated signal, which is then recovered by the lock-in amplifier.

In a typical experiment, we adjust the gold evaporation source's filament current, with the shutter closed, until we measure a steady mass flux on the QCM. We then open and close the shutter multiple times, loading a small number of gold atoms onto the nanotube each time. As expected, the resonance frequency of the nanotube shifts downward during evaporation and remains steady with the shutter closed. The resonance frequency of the nanotube is automatically tracked and recorded at a sampling rate typically between 10 and 100 Hz.

Data from such an experiment are shown in Fig. 4.3. Here white regions indicate that the shutter is open, while shaded regions indicate that the shutter is closed, blocking the gold atoms. The nanotube used in this particular experiment has geometry and mass, determined from TEM images, described by the following parameters: $D_\mathrm{o} = 1.78$ nm, $D_\mathrm{i} = 1.44$ nm, $L = 205$ nm, $m_\mathrm{CNT} = 1.58 \times 10^{-21}$ kg. The initial resonance frequency of the nanotube was set near $f_0 = 328.5$ MHz through electrostatic tensioning[45, 44]. From the resonance frequency and mass of the resonator, we expect a responsivity of 0.104 MHz/zg

(1 zg $= 10^{-24}$ kg). A scale converting frequency shift to mass using this responsivity is shown on the vertical axis to the right. According to this scale, the frequency shift in the first "open" section corresponds to just 51 gold atoms.

The QCM provides a means of confirming the responsivity, initially calculated from TEM-determined parameters. Of course, the QCM does not have the sensitivity to weigh single atoms; however because it averages over a relatively large area, it is an excellent means of measuring mass flux. The mass adsorption rate at the nanotube calculated from the mass flux at the QCM assuming an isotropic evaporation source is

$$\frac{dm_{\mathrm{CNT}}}{dt} = \alpha \cos \theta_{\mathrm{CNT}} \frac{d_{\mathrm{QCM}}{}^2}{d_{\mathrm{CNT}}{}^2} A_{\mathrm{CNT}} \frac{1}{A_{\mathrm{QCM}}} \frac{dm_{\mathrm{QCM}}}{dt} \tag{4.6}$$

Only the sticking coefficient of gold on a nanotube, α, and the misalignment angle of the nanotube to the evaporation source, θ_{CNT}, are not precisely known. Fortunately, it is simple to extract these parameters by varying the evaporation rate. The inset in Fig. 4.3(A) shows the rate of frequency change of the nanotube resonator as a function of mass flux at the QCM over multiple experimental runs. A fit to the data gives a ratio between these quantities of 2.18 ± 0.13 MHz nm^2/zg. This implies that $\alpha \cos \theta_{\mathrm{CNT}} = 0.88 \pm 0.06$, which is reasonable assuming a well aligned nanotube and a relatively high sticking coefficient[107].

Using Eq. 4.6 and the experimentally determined value of $\alpha \cos \theta_{\mathrm{CNT}}$ it is possible to calculate the mass adsorption rate at the nanotube. The QCM records a constant evaporation rate of 2.44 ng/s, which corresponds to an adsorption rate of 1.01 zg/s or equivalently 3.09 Au atoms/s at the nanotube. In comparison, the adsorption rate, calculated using the TEM determined responsivity, is 2.94 Au atoms/s. After accounting for uncertainties in our measurement of $\alpha \cos \theta_{\mathrm{CNT}}$ and for natural, Poissonian variations in adsorption rate,
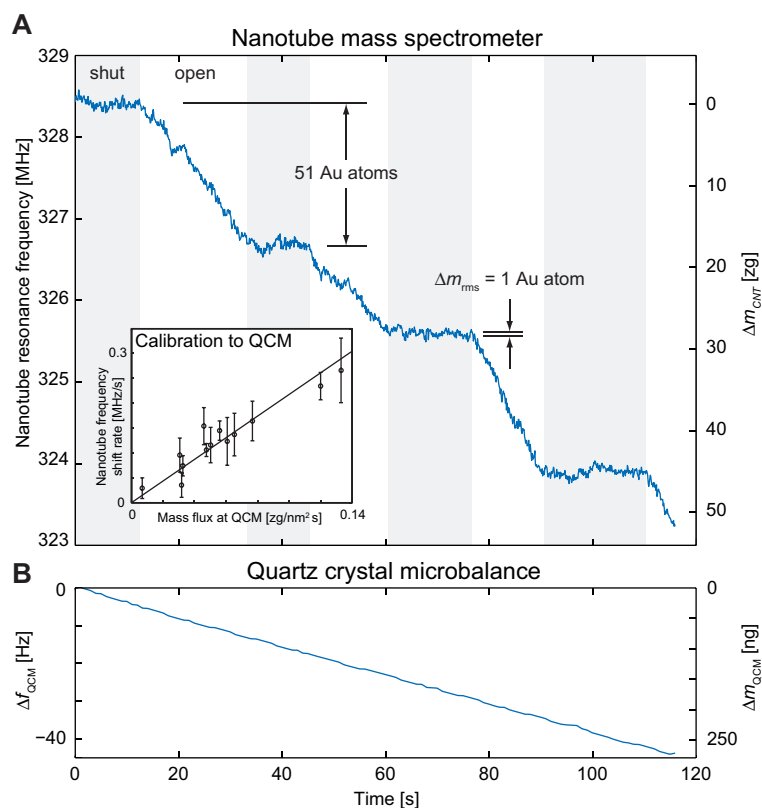
Figure 4.3: (A) The nanotube's resonance frequency versus time during evaporation of gold. The resonance frequency shifts downward when the shutter is open (white regions) and remains constant when the shutter is closed and blocking the gold atoms (shaded regions). The frequency shift in the first open section corresponds to just 51 gold atoms adsorbing to the nanotube. The inset shows a calibration of the nanotube's frequency shift rate versus the mass flux at the QCM. (B) At the same time, the QCM records a constant evaporation rate. Notably, the mass deposited on the QCM is measured in nanograms versus the zeptogram scale used for the nanotube.

these values are in agreement, and thus, the measurements from the QCM are consistent with the TEM determined responsivity.

4.4   Analysis

We now examine how to use our sensitive mass sensor as a mass spectrometer. The noise on the plateaus in Fig. 4.3(A), when no atoms are loaded on the nanotube, demonstrates that the sensitivity of our device is 0.13 zg/$\sqrt{\text{Hz}}$ or equivalently 0.40 Au atoms/$\sqrt{\text{Hz}}$. This is the lowest mass noise ever recorded for a nanomechanical resonator, which is even more striking considering that this measurement was performed at room temperature rather than in a cryogenic environment. These noise levels clearly indicate that we have achieved atomic sensitivity. However, to determine the mass of an adsorbed atom, it is also necessary to know, along with the resulting frequency shift, the position of the atom along the nanotube. One method of accomplishing this is to occlude portions of the resonator so that atoms must land at a specific location. Another method, which we employ here, relies on the statistics of the frequency shifts.

Atoms arrive at the nanotube at a constant average rate. However, because atoms are discrete, the number arriving during any given time interval is governed by Poisson statistics. This effect can be seen in Fig. 4.3(A) where the adsorption rates for the four open sections show significant variation (2.2, 2.1, 3.5, and 2.6 Au atoms/s). There are two independent approaches of using Poisson statistics to measure the mass of the gold atoms. The first approach relies on measuring statistical fluctuations in mass adsorption rate, which we term atomic mass shot noise. The second approach analyzes the statistical distribution

of frequency shifts that occur each sampling period. We now consider each approach in turn.

4.4.1 Atomic mass shot noise analysis

In analogy with electronic shot noise, which has spectral density $S_I^{(\text{shot})}(f) = 2eI$[108], we expect that the mass adsorption rate will have atomic mass shot noise with spectral density $S_{\frac{dm}{dt}}^{(\text{shot})}(f) = 2m_{\text{Au}}\frac{dm}{dt}$. Here we are making a few reasonable assumptions, which are supported by previous studies. We assume that gold arrives as single atoms rather than in clusters[109]. We assume that the arrival of gold atoms is uncorrelated. Finally, we assume that, after landing on the nanotube, gold atoms find a nucleation site to adhere to in a time short compared to the measurement time[107].

An additional complication arises from the fact that our experiment does not measure mass adsorption rate directly, but rather measures the time derivative of the resonance frequency, which is related to the mass adsorption rate though the responsivity function of the resonator, $R(x)$. To account for $R(x)$, we sum the noise contribution at each point along the resonator and arrive at the final equation for atomic mass shot noise:

$$S_{\frac{df_0}{dt}}^{(\text{shot})}(f) = 2m_{\text{Au}}\frac{dm}{dt}\frac{1}{L}\int_0^L dx\,[R(x)]^2 \approx 1.17\frac{f_0^2}{m_{\text{CNT}}^2}m_{\text{Au}}\frac{dm}{dt}. \tag{4.7}$$

Besides atomic mass shot noise, there are other significant noise sources such as readout noise and thermomechanical noise[11]. Both of these noise sources are frequency independent, or white, in $S_{f_0}(f)$. Thus, they will appear as *differentiated* white noise, which grows as the square of the measurement frequency[110], in $S_{\frac{df_0}{dt}}(f)$.

Figure 4.4(A) shows noise levels in our measurements as a function of measurement

frequency. At higher frequencies, some form of differentiated white noise, such as readout noise, dominates. However, at lower frequencies for the evaporation case, atomic mass shot noise dominates. The parameters from our experiment yield an expected atomic mass shot noise of 0.016 $\mathrm{MHz}^2/\mathrm{s}^2/\mathrm{Hz}$, which is drawn as the horizontal gray line in the figure. The total expected noise, including the measured differentiated white noise, is drawn as the dark black line. The data for the evaporation case follow the expected noise level well. A fit to the data yields a measured atomic mass shot noise of 0.014 ± 0.002 $\mathrm{MHz}^2/\mathrm{s}^2/\mathrm{Hz}$, which would result from an atomic mass of 0.29 ± 0.05 zg, consistent with the accepted mass of gold, 0.327 zg. Thus, we have successfully weighed a single gold atom with a nanomechanical resonator.

The low frequency noise for the shuttered case deviates somewhat from differentiated white noise indicating that another low frequency noise process exists, which does not depend on the evaporation of atoms. However, in this case the noise is an order-of-magnitude less than atomic mass shot noise. A potential explanation for this noise source is the current-induced motion of atoms along the surface of the resonator, which may be controlled by limiting the current to sufficiently low levels[111].

4.4.2 Frequency shift distribution analysis

We now turn to the statistical distribution of frequency shifts that occur each sampling period. The distribution of frequency shifts during mass loading (see Fig. 4.7(B)) provides evidence for the Poissonian nature of the mass adsorption process. Because the mass adsorption rate is well known from other calibrations, it is possible to estimate the
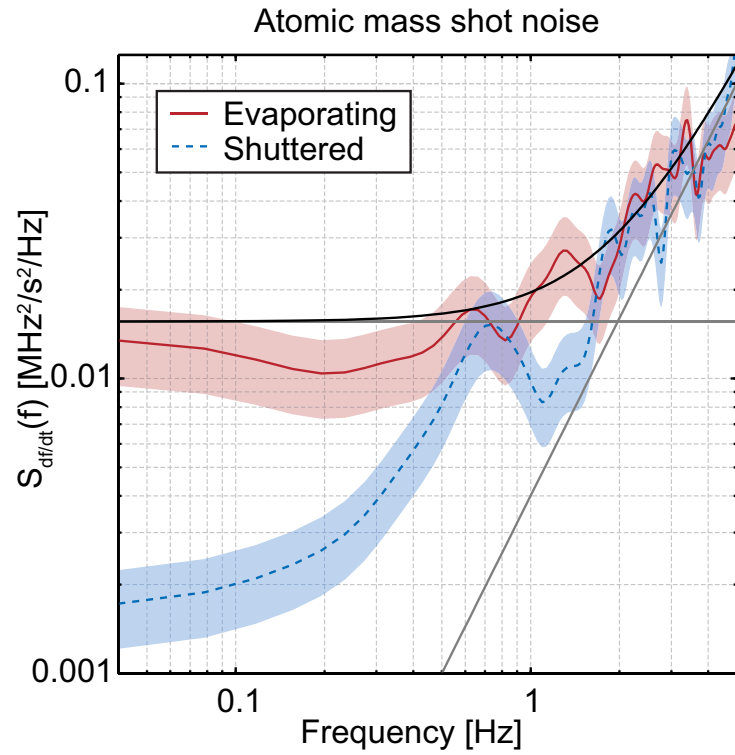
Figure 4.4: Spectral density of the noise in the time derivative of the resonance frequency during evaporation (red) and when the shutter is closed (blue). Shaded regions indicate uncertainty in the estimation of spectral density. In both cases, differentiated white noise dominates at higher frequencies. At lower frequencies for the evaporation case, there is a significant increase in noise caused by the discrete nature of the arrival of mass (*i.e.* atomic mass shot noise). The horizontal gray line depicts the predicted level of atomic mass shot noise, and the sloped gray line is the measured value of differentiated white noise. The black line is the sum of these noise sources.

atomic mass from the number rate of adsorption. Here we derive the expected distribution

of frequency shifts for various number rates.

In the following calculations, we assume that atoms are distributed uniformly

along the cantilever. It is well known that atoms, gold atoms in particular, cluster at

nucleation sites along a nanotube[112]. However, these nucleation sites are relatively evenly

distributed, and thus the assumed uniform distribution is a reasonable approximation.

Ignoring noise, when no atoms land on the resonator, there is obviously no fre-

quency shift. Thus, the probability distribution of frequency shifts is a simple delta function

centered at the origin:

$$q_0(\Delta f) = \delta(\Delta f). \tag{4.8}$$

When a single atom lands on the resonator, the probability distribution of the

resulting frequency shift is proportional to the derivative of the inverse responsivity function:

$$q_1(\Delta f) = \frac{d(R^{-1}(\Delta f))}{d(\Delta f)}. \tag{4.9}$$

According to this distribution (see Fig. 4.5) most atoms landing on the cantilever cause

relatively small frequency shifts. However, there is a significant probability for frequency

shifts approximately four times the mean.

Now we calculate the distribution for an arbitrary number of atoms. Since we

assume that there are no interactions between arriving atoms, the frequency shifts caused

by each atom are independent. Thus the distribution for the sum of two frequency shifts,

say if two atoms land on the cantilever, is given by the convolution of the single atom

distribution, Eq. 4.9, with itself. Likewise, the distribution for an arbitrary number of

atoms, n, may be defined recursively through the convolution of the distribution for $n-1$
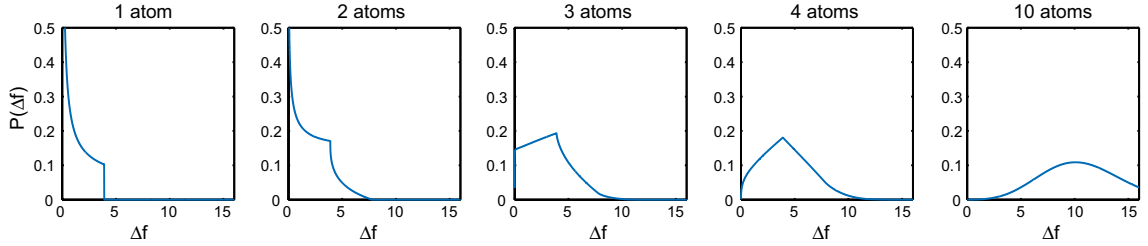
Figure 4.5: Probability distributions for the normalized frequency shifts caused by one atom through four atoms and by 10 atoms. The first few distributions have very distinct shapes, while the 10 atom distribution approaches a Gaussian centered at 10 as expected.

atoms with the distribution for a single atom.

$$q_n(\Delta f) = (q_{n-1} \star q_1)(\Delta f) \qquad (4.10)$$

In Fig. 4.5, we plot the first four non-zero atom distributions as well as a 10 atom distribution. The first few distributions have very distinct shapes, which have a significant effect on the histogram of frequency shifts observed in our experiment. The 10 atom distribution approaches a Gaussian centered at 10 as expected.

The number of atoms landing on the resonator during any given time interval is governed by Poisson statistics. The probability of observing n atoms landing on the resonator in a time interval t when atoms are adsorbing at constant rate λ is given by the standard Poisson distribution: $P(\lambda t, n) = (\lambda t)^n \exp(-\lambda t)/n!$. Now, to find the total distribution of frequency shifts, the distributions for each number of atoms are summed, weighted by their Poisson probability. Accordingly, the expected distribution of frequency shifts is

$$\overline{q(\Delta f)} = \sum_{n=0}^{\infty} P(\lambda t, n) q_n(\Delta f). \qquad (4.11)$$

So far, we have completely ignored any noise in the system. However, the noise levels in our experiment are significant. Fortunately, we know the noise distribution from

measurements of the resonance frequency when the shutter is inserted and no atoms are loaded onto the cantilever. This noise distribution is approximately Gaussian with a standard deviation of 43 kHz. Thus, the final, measured distribution should be the convolution of a Gaussian, $N(\sigma)$, with standard deviation $\sigma = 43$ kHz, with Eq. 4.11:

$$\overline{q(\Delta f)}_{\text{noisy}} = (\overline{q} \star N(\sigma)) (\Delta f). \tag{4.12}$$

For atoms adsorbing much faster than the sampling rate, the distribution is dominated by the $q_n(\Delta f)$ with large n, and thus is essentially a Gaussian centered at the mean Δf. For atoms adsorbing much slower than the sampling rate, the distribution is dominated by $q_0(\Delta f)$ and to a lesser extent $q_1(\Delta f)$. Accounting for noise, this distribution is essentially a Gaussian centered at the origin with a very few additional large frequency shifts. For adsorption rates near the sampling rate, the distribution becomes distinctly non-Gaussian. Fig. 4.6 illustrates these three scenarios.

In our experiment, we adjusted the adsorption rate so that it was near the sampling rate, or approximately 0.3 Au atoms/sample. Thus, we obtained a non-Gaussian distribution and were able to extract information about the mass of individual atoms. The histogram of frequency shifts is shown in Fig. 4.7. The expected distribution of frequency shifts, using the accepted atomic mass, m_{Au}, is drawn as the black line. The inset shows a measure, based on a χ^2 test, of how well the data fit the expected distribution calculated for various values of atomic mass. Due to the number of large downward frequency shifts ($\Delta f < -100$ kHz), these data are only consistent with distributions calculated for an atomic mass between 0.1 zg and 1 zg ($m_{\text{Au}} = 0.327$ zg). This is an independent measurement of mass of a single gold atom, though the atomic mass shot noise technique is more precise.
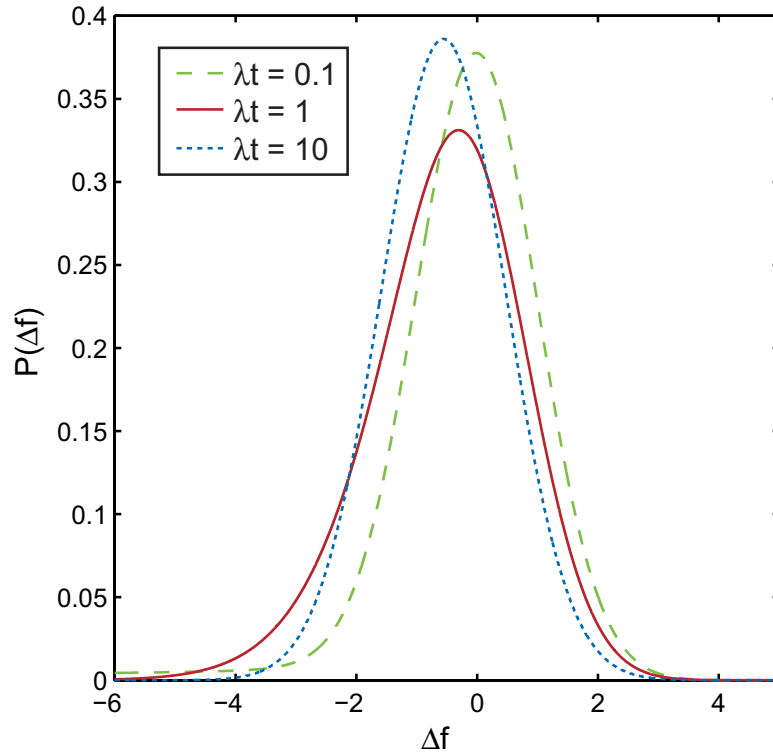
Figure 4.6: The expected distribution of normalized frequency shifts for 0.1, 1, and 10 atoms/sample (green, red, and blue curves, respectively) given a constant unit mass adsorption rate. Due to the constant mass adsorption rate, the atoms for the green curve must be 10 times more massive than atoms for the red curve, while atoms for the blue curve must be 10 times less massive. Significant numbers of large downward frequency shifts for distributions like the red curve allow accurate determination of the number of atoms per sample.
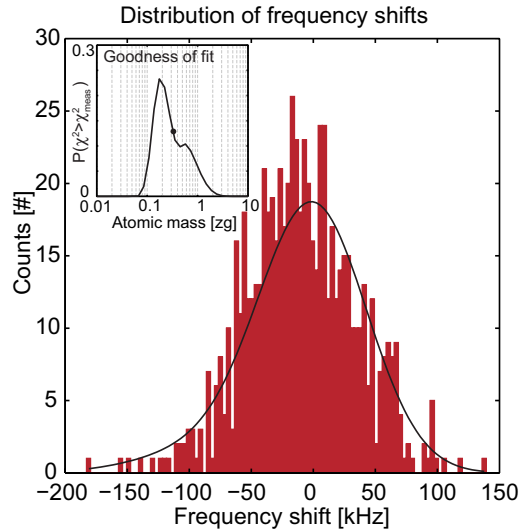
Figure 4.7: Histogram of frequency shifts per sampling time during evaporation. The black line shows the expected number of counts according to our model given the correct value of the atomic mass, m_{Au}. The inset shows a measure of how well the data fit the expected distribution calculated for various values of atomic mass. Due to the large number of downward frequency shifts ($\Delta f < -100$ kHz), the data are only consistent with distributions calculated for atomic masses between 0.1 zg and 1 zg ($m_{Au} = 0.327$ zg).

Of course the underlying purpose of this work is not to obtain a revised value for the mass of a gold atom, but rather to demonstrate the power of the technique.

4.5   Discussion

Our atomic-resolution nanomechanical mass sensor has significant advantages over traditional high-resolution mass spectrometers. Most notably, it does not require ionization of the test sample, which makes it more suitable for large biomolecules such as proteins. These molecules are often destroyed during ionization even with "soft" ionization techniques such as matrix-assisted laser desorption/ionization (MALDI)[113] and electrospray ioniza-tion (ESI)[114]. Our device becomes more sensitive at higher mass ranges, in contrast with

traditional mass spectrometers. Finally, our device is compact, as it does not require large

magnets or long drift tubes, and could in principle be incorporated on a chip.

Part II

In-situ TEM force measurements

Chapter 5

Force measurements during carbon nanotube buckling

Carbon nanotubes are renowned for their remarkable mechanical properties, which include exceptionally high axial elastic modulus and tensile strength[115, 94, 116]. Because of such advantageous properties, nanotubes have been suggested as components in mechanical systems ranging from atomic force microscope (AFM) tips[117] to resilient composites[118] to stronger-than-steel cables[81, 119] (such as those critical to space elevator applications)[120]. All of these applications, including those employing collections of nanotubes, would benefit greatly from a better understanding of the mechanical behavior of individual nanotubes. While the elastic modulus and tensile strength of individual nanotubes have been well characterized by multiple techniques[115, 94, 116, 121], an equally important property, the critical buckling load is comparatively less well understood. Thus, we here study the buckling behavior of individual, isolated multi-walled carbon nanotubes

(MWNTs).

Buckling is the failure of a structural component under an excessive compressive load. Obviously, this effect is critical on the macroscopic scale where it is a principal consideration in the design of structural members for buildings and bridges, but it is also important on the nanoscale where, for example, it governs the behavior of nanotube-tipped AFM cantilevers or determines whether a nanotube can penetrate a cell's membrane[122].

Two distinct forms of buckling, one simply termed "buckling" and the other termed "kinking," are discussed in this paper. Simple buckling, depicted in Fig. 5.1(B), occurs when the nanotube no longer remains straight under a compressive load. In this case, a relatively constant curvature develops along the entire length of the nanotube. Kinking, a more drastic form of buckling depicted in Fig. 5.1(C), occurs when the compressive load increases until a sharp bend forms at one point along the length of the nanotube.

In our experiment, we measure the forces involved in buckling and kinking an individual, isolated MWNT. Our approach has distinct advantages over previous nanotube buckling experiments[123, 124, 125, 126]. Most importantly, we observe the MWNT's geometry with nearly atomic resolution while measuring the forces involved. Also, we avoid interference in the force measurements from a substrate or embedding-matrix through meticulous control of the experiment's geometry. Finally, we can repeat the experiment on the same nanotube to look for possible permanent structural changes. These experiments were performed in close collaboration with William Mickelson.
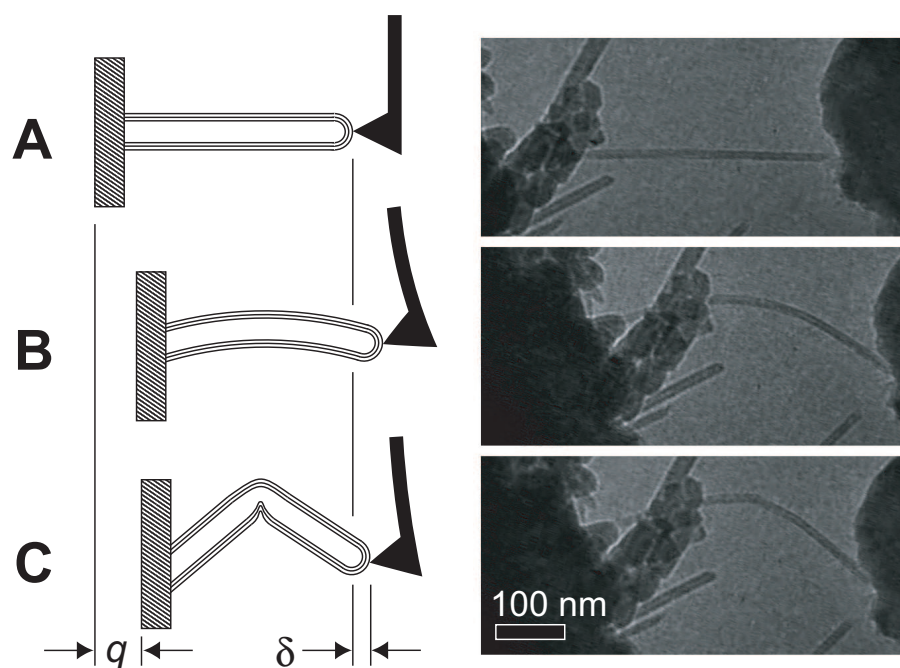
Figure 5.1: Schematic of a buckling and kinking force measurement along with corresponding TEM video frames of the measurement in progress. (A) Straight nanotube. A single MWNT protrudes from the translator on the left and contacts an AFM cantilever on the right. The AFM cantilever shows no deflection and thus there is no applied compressive force. (B) Buckled nanotube. As the translator moves to the right, the nanotube pushes against the AFM cantilever. In return the AFM cantilever applies a compressive force to the nanotube, which causes it to buckle. (C) Kinked nanotube. Further rightward translator movements cause the nanotube to kink, or locally buckle, which reduces the compressive force sustained by the nanotube.
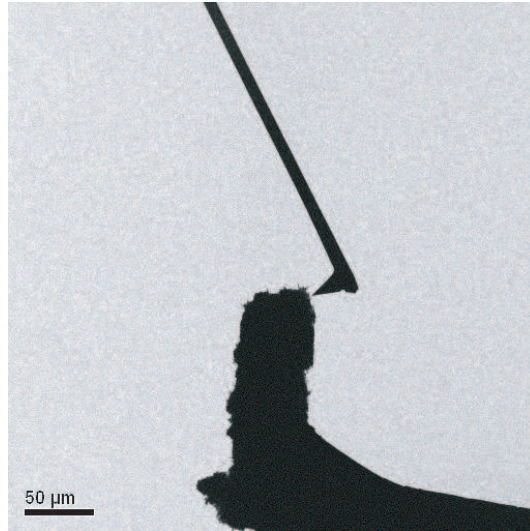
Figure 5.2: AFM inside the TEM.

5.1 Experiment

The experimental requirements for measuring the forces involved in buckling and kinking a single MWNT while observing its geometry are demanding. To precisely measure the forces, an AFM would be ideal. However, to observe the MWNT geometry, including the structure of the inner nanotubes, with atomic resolution, a transmission electron microscope (TEM) is necessary. Finally, to manipulate the nanotube at the nanoscale in order to control the buckling process, a nanopositioning platform is required. We satisfy all of these requirements by outfitting a commercial TEM nanopositioning system (Nanofactory Instruments AB) with a standard AFM cantilever.

The initial configuration of our experimental setup is shown schematically in the left half of Fig. 5.1(A). On the left side of the schematic is the piezoelectric translator of the nanopositioning system. The MWNT to be characterized is attached to this translator.

On the right side of the schematic is the AFM cantilever, which is placed on the stationary (relative to the microscope) side of the nanopositioning system in an orientation such that the cantilever is deflected in the plane that forms the TEM image. Importantly, both the MWNT and AFM cantilever are electrically grounded to prevent charging from the TEM's electron beam. At the start of an experiment, the MWNT is positioned using the translator so that it contacts, but does not deflect, the AFM cantilever. Through the course of an experiment, the translator extends and retracts causing the nanotube to go through various stages of buckling and kinking. The entire experiment is conducted at room temperature inside a JEOL-2010 TEM and recorded with a GATAN 794 charge-coupled device video camera.

In a typical experiment, the geometry of the MWNT progresses through three stages: straight, buckled, and then kinked. These stages are shown schematically in the left column of Fig. 5.1. At the start of the experiment, the MWNT is straight as shown in Fig. 5.1(A). There is no force on the nanotube, and thus the AFM cantilever shows no deflection. As the translator extends to the right by distance q the nanotube displaces the AFM cantilever on the right by distance δ. In return, the AFM cantilever applies a compressive force $F = -k_{\text{eff}}\delta$ to the nanotube, where k_{eff} is the effective spring constant of the AFM cantilever. This compressive force eventually causes the nanotube to buckle, as shown in Fig. 5.1(B). By further moving the translator to the right, it is possible to steadily increase the force applied to the already buckled nanotube. Finally, at some critical load, a sharp bend or kink forms along the nanotube as shown in Fig. 5.1(C).

An experiment does not necessarily end once the nanotube kinks. Afterward, it

is possible to retract the translator and relieve the force on the nanotube. The kink in the nanotube will disappear and the nanotube will relax to its unloaded, straight configuration. The experiment may be repeated multiple times on the same nanotube to confirm the critical buckling and kinking forces or to test for permanent structural damage inflicted on the nanotube by the buckling or kinking.

The right column of Fig. 5.1 shows TEM video frames from an experiment in progress. The chosen frames correspond to the straight, buckled, and kinked geometries shown schematically in the left column. As in the schematics, the translator is on the left, and the tip of the AFM cantilever appears on the right.

One notable difference between the video frames and the schematics is that the translator appears much "dirtier" in the video. This is due to our method of attaching the MWNT. In fact, we do not attach a single MWNT to the translator, but rather, for reasons of practicality, we attach a macroscopic mat of many MWNTs with epoxy. All force measurements are made on a particular nanotube that protrudes far from the mat. Unfortunately, this technique somewhat obscures the translator-side attachment of the nanotube; however, as will be discussed later, this does not pose significant problems.

There is a wealth of information regarding the buckling process contained in the TEM video. Most importantly, it is easy to quantify the displacements of both the translator and the AFM cantilever. We note, for example, that the AFM tip deflects to the right more when the nanotube is buckled (Fig. 5.1(B)) than when it is kinked (Fig. 5.1(C)) indicating that a kinked nanotube supplies less force. And, it is straightforward to measure basic properties of the MWNT such as its inner and outer diameters and its length. Moreover,

the shape of the buckled nanotube, the location and angle of the kink, and the way the nanotube contacts the AFM tip are all clearly visible. Such detailed information about the MWNT's geometry has not been available in previous experiments[123, 124, 125, 126], and these data now facilitate a much more accurate analysis of MWNT buckling.

The first step in analyzing the buckling and kinking data is to determine the force supplied by the MWNT through the various stages of buckling and kinking. In our experimental setup due to the restrictive geometry of the TEM, forces are not read from the AFM using one of the standard techniques[127]. Rather, as mentioned earlier, it is possible to directly measure the deflection of the AFM cantilever by imaging it with the TEM itself. Here an image processing routine analyzes the recorded TEM video to find the deflection of the cantilever. This deflection is converted to a force via the effective spring constant of the cantilever ($k_{\text{eff}} = 0.3$ N/m, calibrated using Sader's method)[128]. A similar system has been successfully used to measure forces in other experiments that demand the atomic resolution of the TEM, such as measuring the interlayer forces between telescoping nanotubes[129]. In this experiment, we use this technique to achieve force sensitivities on the order of 180 pN.

Using the image processing routine, we found the compressive force applied to the nanotube and the translator position through the course of a typical experiment. These are shown in the top and bottom plots, respectively, of Fig. 5.3. The nanotube begins in the unbuckled state shown in Fig. 5.1(A), but it becomes slightly buckled as soon as the translator moves. In the first section, the translator slowly moves in steps to the right. At first, each translator step results in significant increases in compressive force, on the order
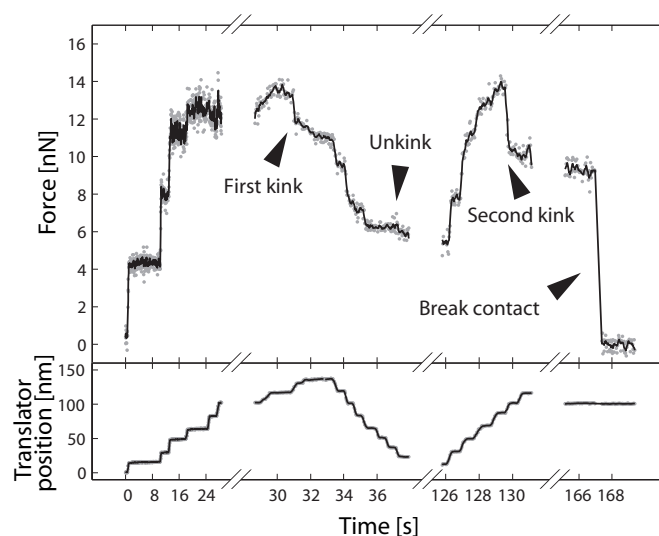
Figure 5.3: Force measurements on a buckled and then kinked nanotube over the course of a typical experiment. The top plot shows the force supplied by the nanotube as it progresses through various stages of buckling and kinking. Note the rapid decrease in supplied force following a kink. The bottom plot shows the position of the translator, which extends or retracts to control the buckling or kinking. In order to clarify the presentation, the first section uses a different time scale.

of 4 nN. However, the first step after the 16 s mark results in a smaller increase in force around 1 nN, and the following two steps result in no significant increase in force. Thus, as the nanotube becomes more buckled, the force it supplies approaches a constant value.

In the next section, the translator again slowly moves to the right until the compressive force reaches 13.5 nN and the nanotube kinks (Fig. 5.1(C)). Within the time span of a single TEM video frame (33 ms), the force supplied by the nanotube decreases 1.7 nN. This sudden decrease in force is indicative of an elastic instability. Over the next two seconds, while the translator remains stationary, the force continues to decrease by another nanonewton, indicating some form of relaxation process. The translator then retracts until the nanotube unkinks, which interestingly results in only a very small change in force.

In the third section, the experiment was repeated on the same nanotube. The

translator was again moved to the right, and the force supplied by the nanotube followed a similar curve and kinked in the same position and at almost the same force, 13.8 nN. However, this kink resulted in a significantly larger sudden decrease in force, 2.7 nN, possibly indicating that the slow relaxation of the previous kink resulted in permanent changes to the nanotube's structure.

In the last section of Fig. 5.3, the contact between the nanotube and the AFM tip was broken. This allowed the cantilever to relax to its neutral position, which defines the baseline for zero force.

5.2 Analysis

The first two sections of our analysis, Sec. 5.2.1 and Sec. 5.2.2, use classical elastic theory, where the MWNT is modeled as a continuum elastic medium, to explain many of the experimental results. Section 5.2.1 uses Euler's theory of buckling to describe the forces produced during simple buckling. Fitting this model to our experimental data yields the critical buckling load and Young's modulus of the MWNT. Section 5.2.2 uses Brazier's theory of buckling, which includes the effect of a deformable cross-section, to describe the process of kinking and provide a close lower bound for the critical kinking moment of the MWNT, which is consistent with our experimental data.

The last section of our analysis, Sec. 5.2.3, discusses the limits of elasticity in MWNTs. Here we calculate a lower limit to the yield strength of MWNTs and present evidence for permanent changes in the atomic structure of the MWNT following the first kink.

5.2.1 Euler buckling

Euler was the first to give an analytical model of buckling, and although his model is simplistic, it contains many of the features of more advanced models. In the Euler model, there is an initially straight, uniform, elastic beam with Young's modulus Y and areal moment of inertia I, which is under a compressive force, F, from the ends. According to the elastic theory of beams, the deflection, $y(x)$, of the beam from its initially straight configuration is described by the differential equation[130]:

$$YI\frac{d^4y}{dx^4} + F\frac{d^2y}{dx^2} = 0 \tag{5.1}$$

For small loads, this model only permits the trivial solution $(y(x) = 0)$, or a perfectly straight column. However when the load is increased to some critical load, F_{cr}, a situation known as an elastic instability occurs where there are two solutions, the straight column solution and the buckled solution. The straight column solution is unstable to small perturbations in y, hence above F_{cr}, the column buckles.

The value of the critical buckling load depends on how the nanotube is attached to its supports. It is clear from Fig. 5.1, that the attachment on the right may be described as a pin-joint because the angle of the nanotube relative to the surface is variable. The attachment on the left, however, is somewhat obscured. To discern the type of attachment, we extend lines tangent to the nanotube as it disappears behind the substrate for multiple frames of the video. These lines converge approximately to the same point, again indicating a pin-joint and also revealing the approximate location of the attachment. Now, Eq. 5.1 can be solved using the boundary conditions for a doubly pin-jointed beam of length L $(y(0) = 0,$

$y(L) = 0$, $y''(0) = 0$, $y''(L) = 0$) to give a critical buckling load of $F_{\mathrm{cr}} = \pi^2 Y I / L^2$.

Euler's model is a great simplification. If it were to hold true, we would expect a sharp, discontinuous initial increase in force as the translator was first moved causing the nanotube to buckle, and then relatively small changes in force as the translator was moved further. As can be seen in the first and third section of Fig. 5.3, the increase in force is continuous and only begins to taper off after the translator has moved more than 100 nm. The problem lies in the fact that the nanotube is not, strictly speaking, a perfectly straight column, which can be seen by closely examining Fig. 5.1(A).

To extend Euler's model to account for initially slightly crooked columns, we assume that the column has an initial shape, $y_0(x)$ and a deflection from this shape of $y_1(x)$. Equation 5.1 is modified to give[130]:

$$YI\frac{d^4y_1}{dx^4} + F\frac{d^2}{dx^2}(y_0 + y_1) = 0 \tag{5.2}$$

For simplicity, we assume $y_0(x)$ has the form $A\sin(\pi x/L)$. Note that a more complicated, empirical form determined from TEM micrographs (Fig. 5.1(A)), yields similar results. This more realistic model has the solution:

$$y = y_0 + y_1 = \frac{A}{1 - F/F_{\mathrm{cr}}}\sin(\pi x/L) \tag{5.3}$$

which allows small deflections for small loads. However, as the load increases toward F_{cr}, the critical load for Euler's simple model, the deflection again diverges.

As suggested by these models, in Fig. 5.4 we replot the data from Fig. 5.3 (along with more data for the same nanotube, which was not shown in Fig. 5.3) as compressive force versus maximum displacement. The data are grouped into four sweeps: an initial outward
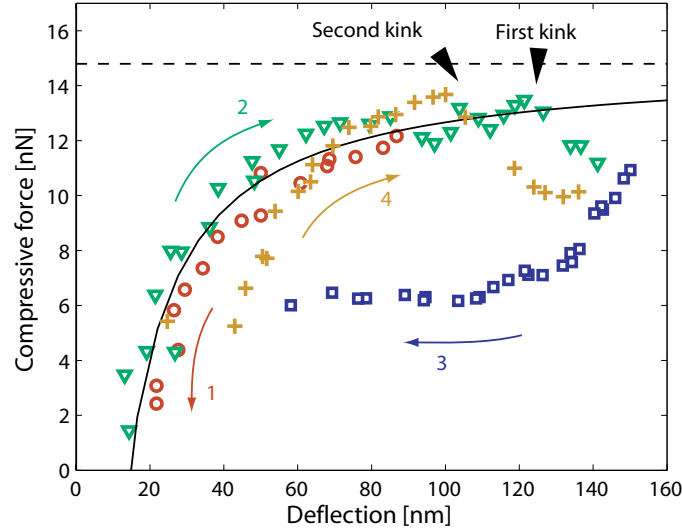
Figure 5.4: Compressive force applied to a nanotube versus the maximum deflection from a straight configuration for a buckled and then kinked nanotube over multiple cycles. The data before the kinks is well described by Euler's theory of buckling applied to an initially slightly crooked column. A fit to this model is shown by the solid line. The horizontal dashed line represents a parameter of this fit, the asymptotic critical buckling load.

sweep to straighten the nanotube, the first inward sweep and the first kink, another outward sweep with the nanotube in its kinked configuration, and a second inward sweep to repeat the experiment.

The portion of the data where the nanotube is not kinked (*i.e.* sweep 1 and the first portions of sweeps 2 and 4) is well described by Euler's model with the initially slightly crooked column. We fit this model, as described by Eq. 5.3, to the data from sweep 1 and the first portion of sweep 2 using the amplitude of y_0 and the critical buckling load as fitting parameters. From the fit, we determine $A = 14.4$ nm and $F_{cr} = 14.8$ nN.

From the fitted value of the critical load and from the length and inner and outer diameter measurements of the nanotube from the TEM video images, it is possible, using Euler's formula for the critical load, to determine a value for the Young's modulus of the

nanotube. Using the values $F_{\mathrm{cr}} = 14.8$ nN, $L = 610$ nm, $D = 12.8$ nm, $D_{\mathrm{i}} = 3.2$ nm, we find that $Y = 425$ GPa. This value is consistent with previous measurements of the Young's modulus for MWNTs obtained with alternate techniques[131].

5.2.2 Brazier theory and local buckling

In Euler's theory of buckling, it is assumed that the cross-section of the column remains constant throughout the buckling process. This is not necessarily true, and moreover, a deformable cross-section has significant effects on buckling. As a cylindrical tube is bent, its cross-section changes from circular to elliptical, most dramatically at its midpoint where the curvature and thus bending moment are greatest. The change in cross-section decreases the tube's flexural stiffness making it progressively easier to bend, or more specifically reducing the additional bending moment required to induce a unit change in curvature. This implies that there is a maximum bending moment that the tube can withstand. Beyond this point, the tube buckles locally, or kinks, where the bending moment is greatest, again at the center. Both the decrease in flexural stiffness and the kinking are new effects not found in Euler's original theory of buckling.

Brazier studied these effects for the case of a thin-walled tube with an initially circular cross-section[132]. He calculated the maximum moment that the tube could withstand, or the critical kinking moment, to be[133]:

$$M_{\mathrm{kink}} \approx 0.4683 \frac{YDt^2}{\sqrt{1 - \nu^2}} \qquad (5.4)$$

Here, t is the thickness of the tube and ν is the Poisson ratio of the tube's material ($\nu = 0.17$ for graphite[134]).

Many MWNTs, including the one used in this study, are not necessarily "thin-walled" as their thickness is a significant portion of their total radius. Nonetheless, Brazier theory provides a useful lower bound for their expected critical kinking moment. This lower bound is determined by considering only the outermost shells of a thick MWNT, which do form a thin tube. Clearly, the critical kinking moment of the entire, thick MWNT will be greater than this bound as the inner shells can only impede formation of a kink. For the approximations used in Brazier theory to hold, the thickness of these outer shells must be significantly less than the MWNT's radius. For the particular MWNT used in our experiment, considering only the outer two shells and using the fitted value for Y, the lower bound for the critical kinking moment is 1200 nN nm. The measured critical kinking moment, as determined from Fig. 5.4, rests slightly above this limit, as expected, at 1600 nN nm.

5.2.3 Plastic deformation

Before the MWNT kinks, it displays, to within the precision of our instrument, completely elastic behavior. This is easily seen in Fig. 5.4 by considering that paths 1 and 2 coincide. Interestingly, we can use this fact to calculate a lower bound for the yield strength of MWNTs of 1.7 GPa, which is greater than the yield strength of steel[135]. However, after the first kink, there is evidence that the MWNT has been plastically deformed meaning that there have been permanent changes to its atomic structure.

First, it should be noted that the hysteresis in the force versus deflection curve of Fig. 5.4 is not, by itself, an indication of plastic deformation. This particular inelastic

behavior occurs because of the rapid transition between configurations with different strain energies during a kink. The excess energy is dissipated through vibrations and heat and not, necessarily, through rearrangements in atomic structure.

Rather, evidence for plastic deformation comes from the slightly different force versus deflection curve of path 4 when compared to paths 1 and 2. The curve of path 4 indicates that the neutral shape of the MWNT, after the first kink, has become more crooked. As was done with paths 1 and 2, we fit the model described in Eq. 5.3 to path 4, and from the fit, we determine that there was a larger initial deflection of 30 nm. Obviously, a change in the neutral shape of the MWNT must be due to changes in the atomic structure.

More evidence for plastic deformation comes from the critical bending moment of the second kink. While the second kink occurs at the same position along the nanotube and at approximately the same compressive force, it occurs at a significantly lower bending moment. The change in critical bending moment must be due to a local (*i.e.* near the kink) change in one of the parameters of Eq. 5.4 or to a flattening of the cross-section of the nanotube at the kink, both due to changes in atomic structure.

It is still an open question as to what mechanism governs the atomic rearrangements. Some changes in atomic structure likely occur immediately following or even during the kinking process. Quick atomic rearrangements as a result of kinking have been predicted by molecular dynamics simulations[136]. Other changes appear to occur over longer periods of time. Shortly after the first kink, there is, as shown in Fig. 5.3, a period where the force supplied by the MWNT slowly relaxes over the span of two seconds. This could be explained by the thermally assisted migration of defects, either inherent to the nanotube

or created by the 100 keV electron beam of the TEM, to the area of the kink.

5.3   Discussion

Using our technique for operating an AFM inside a TEM, we have thoroughly studied the forces involved in repeatedly buckling and kinking a single MWNT and correlated them with the geometry of the MWNT. Specifically, we have precisely measured the compressive force sustained by a buckled and then kinked, or locally buckled, MWNT as a function of its deflection from an initial state. These measurements are in good agreement with the classical elastic theory of buckling. Moreover, the value of the Young's modulus for a MWNT determined by these measurements is consistent with values obtained by alternate techniques. Finally, by repeatedly buckling and kinking a MWNT, we have tested the limits of its elasticity and set a lower bound on its yield strength.

Chapter 6

Friction between telescoping nanotubes

The grip of tire-tread, the squeaks from an unoiled hinge, and the wear on automobile parts are all consequences of friction. A better knowledge of friction could save industry considerable money and introduce new commercial applications. However, even though the subject is often taught as a simple macroscopic law, the fundamental mechanisms and models governing friction at the nanoscale are not well understood. Fortunately, advances in experimental methods at the nanoscale are opening new doors to the study of friction.

Carbon nanotubes, in particular, offer unique insights into the nature of friction. As discussed in Ch. 2, multi-walled carbon nanotubes exhibit a striking telescoping property[76], which has found widespread application as a linear bearing in nanomechanical systems[77, 78, 106]. Of course, understanding friction in these telescoping devices is cru-

cial to their commercial application. More fundamentally, telescoping nanotubes provide an ideal, one-dimensional system to study nanoscale friction. Here we describe theories of nanoscale friction, measure the interlayer forces between telescoping nanotubes, and place limits on the frictional forces in this system. These experiments were performed in close collaboration with Andras Kis.

6.1 Theory of nanoscale friction

There are numerous modes of friction and even more models describing the different modes. We introduce a few models which have particular relevance to friction in telescoping nanotubes. The Brownian motion model (see Sec. 6.1.1), which forms the basis for many more sophisticated models, relates friction and the dissipation of energy to the statistical fluctuations in a fluid. The sliding friction model (see Sec. 6.1.2) builds on this model by introducing a corrugated potential, which greatly amplifies the Brownian friction, and by defining friction in terms of the constant external force required for movement. Finally, the "stick-slip" model (see Sec. 6.1.3) replaces the constant external force with a more realistic spring-like force, whose effects highlight the importance of unstable equilibria. In all of these methods, dissipation is described at the statistical mechanics level in terms of irreversible processes. The fundamental friction mechanisms arising from electronic and phononic effects are described in the final section, Sec. 6.1.4.

6.1.1 Brownian motion model

The Brownian motion model, as its name suggests, describes friction in terms of a massive object moving through a viscous fluid. The kinetic energy of the object is dissipated through collisions with particles in the fluid. Here, the terms "particle" and "fluid" are used in a very general sense. They could mean actual atoms or gases. Or, for surfaces sliding against one another, the fluid is actually the electron and phonon gases in the materials, and the particles are elementary excitations of these gases. This is a very general model that ignores the exact mechanism of dissipation and describes friction at a statistical mechanics level.

To make this model quantitative, we consider the case of a free Brownian particle with mass m, which is constantly bombarded by other particles. As a result of these impacts, the Brownian particle feels a force, which may be separated into two components: a dissipative term, $-m\Gamma\dot{x}$, representing viscous drag and a rapidly fluctuating term, $f(t)$, which averages to zero over long time periods. Thus, we write the equation of motion in one dimension as

$$m\ddot{x} = -m\Gamma\dot{x} + f(t); \quad \langle f(t) \rangle = 0. \tag{6.1}$$

This is known as the Langevin equation. The dissipative term in this equation represents Brownian friction with Γ being termed the Brownian friction coefficient[49].

As mentioned earlier, the dissipative term fundamentally results from electronic and phononic effects, which we discuss in Sec. 6.1.4. On a statistical mechanics level, the dissipative term is related to the random force fluctuations. This relationship can be made explicit by solving Eq. 6.1 for the ensemble average of the energy of the particle and setting

this equal to the result expected from the equipartition theorem. The final result, known as the fluctuation dissipation theorem, is

$$\langle f(t)f(t')\rangle = 2m\Gamma k_{\mathrm{B}}T\delta(t-t').\tag{6.2}$$

In fact, this is just another way of describing thermomechanical noise (Eq. 1.19) which was encountered in Ch. 1. According to this equation, we could, in principle, measure friction simply by measuring the fluctuations in force experienced by the object.

6.1.2 Sliding friction model

The measured value of friction is often much greater than that predicted by the Brownian motion model and fundamental friction mechanisms. This is because the Brownian friction coefficient can be amplified by placing the Brownian particle in certain potentials. For example, a particle adsorbed to a crystalline surface will experience a regularly varying van der Waals attraction as a function of its position. Such potentials create barriers that impede the free motion of the particle. However, the combination of a small external force and thermal excitations can still cause the particle to move. We define sliding friction in terms of this external force.

To model this effect, we use the simple potential $U(x) = U_0(1 - \cos(2\pi x/a))$ and apply an external force F. The equation of motion is then

$$m\ddot{x} = -m\Gamma\dot{x} - \frac{\partial U}{\partial x} + f(t) + F\tag{6.3}$$

$$= -m\Gamma\dot{x} - \frac{2U_0\pi}{a}\sin(2\pi x/a) + f(t) + F.\tag{6.4}$$

Figure 6.1 shows a particle in such a potential before and after an external force is applied.
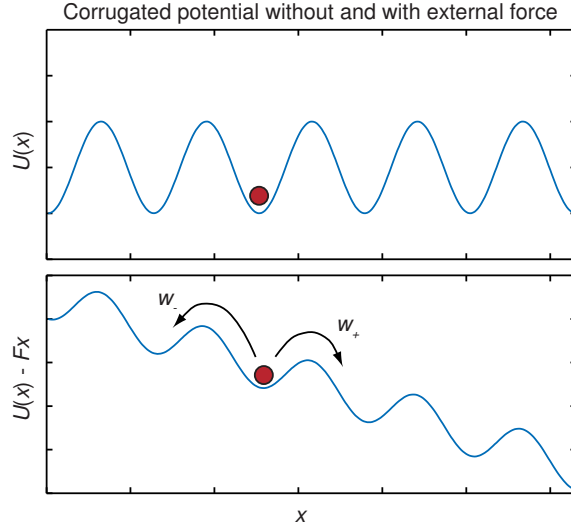
Figure 6.1: A particle lies in a corrugated potential. Before application of an external force, the particle cannot overcome the activation barriers and remains still. With an external force, the barrier on the right is effectively reduced. The particle will jump to the right with rate w_+ and to the left with rate w_-, where $w_+ > w_-$.

Generally, the $2U_0$ potential barrier prevents the particle from moving. However, when the constant force F is applied, the particle begins to drift in one direction with velocity v. Thus, we may define a new sliding friction coefficient, $\overline{\Gamma}$, through the equation

$$m\overline{\Gamma}v = F. \tag{6.5}$$

Now we find explicit formulas for $\overline{\Gamma}$ in the small and large force limits. We first analyze the small force limit $(Fa/2 + k_{\mathrm{B}}T \ll 2U_0)$. Here, the potential barrier is much greater than the energy supplied by the external force and thermal energy. Boltzmann's law gives the probability that a particle has sufficient energy to jump over the activation barrier either to the right or left. Combining this probability with an effective rate ν for

hitting the barrier yields the following rates for jumps to the right, w_+, or left, w_-:

$$w_+ = \nu \exp\left(-\frac{2U_0 - Fa/2}{k_B T}\right) \quad (6.6)$$

$$w_- = \nu \exp\left(-\frac{2U_0 + Fa/2}{k_B T}\right). \quad (6.7)$$

In the large friction (*i.e.* over-damped) limit, the effective collision rate is

$$\nu = \frac{2\pi U_0}{\Gamma m a^2}. \quad (6.8)$$

According to these rates, the ensemble average of the velocity is

$$\langle \dot{x} \rangle = a(w_+ - w_-) = 2a\nu \exp\left(-\frac{2U_0}{k_B T}\right)\sinh\left(\frac{Fa}{2k_B T}\right). \quad (6.9)$$

Combining Eq. 6.5 and Eq. 6.9 and taking the small force limit, we arrive at an equation for the sliding friction coefficient[83]:

$$\overline{\Gamma} = \frac{\Gamma}{2\pi}\frac{k_B T}{U_0}\exp\left(\frac{2U_0}{k_B T}\right). \quad (6.10)$$

There are a few interesting things to point out about Eq. 6.10. First, the sliding friction coefficient is proportional to the Brownian friction coefficient, and, in the region where our approximations are valid, it is much greater than the Brownian friction coefficient. Second, increasing the temperature or reducing the potential barrier reduces sliding friction as expected. Finally, the sliding friction coefficient is independent of the potential's period.

In the large force limit ($Fa/2 + k_B T \gg 2U_0$) the particle can jump over many potential wells at the same time. Essentially, the particle does not see the corrugated potential. The friction in this case approaches the friction for the Brownian model, $\overline{\Gamma} \rightarrow \Gamma$.

Stick-slip friction and elastic instabilities
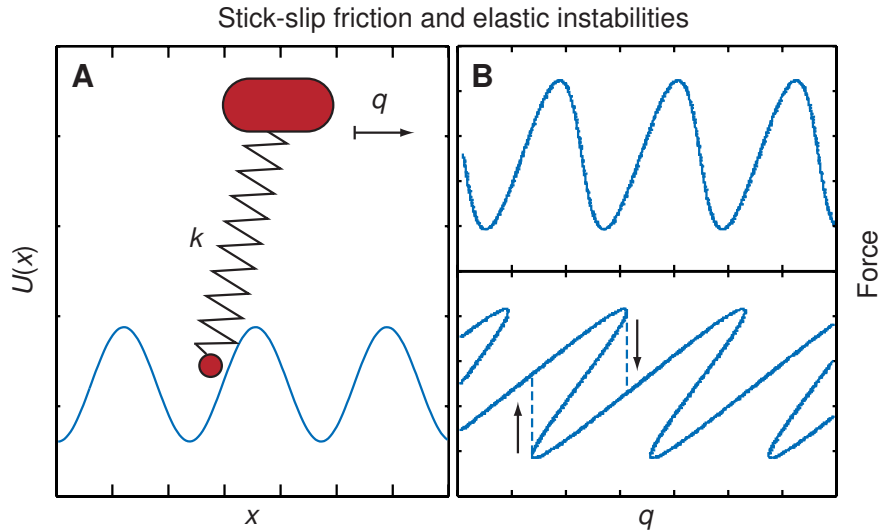
Figure 6.2: Stick-slip friction model. (A) A spring is attached between a mobile support and the particle. There are now two coordinates, the position of the particle x and the position of the support q. (B) For stiff springs, the force on the particle is a smooth function of the support position (top). For soft springs, the force undergoes discontinuous jumps and displays hysteresis as a function of the support position (bottom).

6.1.3 "Stick-slip" friction model

In most friction experiments, it is difficult to apply a constant external force because the object applying the force has a finite spring constant. The action of this spring dramatically affects the dynamic behavior of the system and is responsible for what is known as "stick-slip" friction[137]. A model system for stick-slip friction is shown in Fig. 6.2(A).

According to our model, we must add a spring term to the potential used in Eq. 6.3 so that the potential becomes

$$U(x,q) = U_0(1 - \cos(2\pi x/a)) + \frac{1}{2}k(q-x)^2 \qquad (6.11)$$

where x is still the position of the particle and q is the position of the support attached to the spring.

Through minimizing the potential, we solve Eq. 6.11 for the equilibrium position of the particle.

$$\frac{2U_0\pi}{a}\sin(2\pi x/a) + k(q - x) = 0 \qquad (6.12)$$

Assume for simplicity that the support is positioned above a maximum in the potential so that

$$\frac{2U_0\pi}{a}\sin(2\pi x/a) + kx = 0. \qquad (6.13)$$

When the spring is "stiff" meaning $k > 4\pi^2 U_0/a^2$, there is only one solution to this equation, and thus there is only one equilibrium position of the particle. However, when the spring is "soft" there can be multiple stable positions. Obviously, the dynamics of the sliding particle will differ greatly between these two scenarios.

Figure 6.2(B) shows typical plots of the theoretical force versus position of the support for both the stiff (top) and soft (bottom) spring scenarios. For the stiff spring scenario, the particle follows the corrugated potential smoothly as it is dragged along the surface. Thus, the force acting on the spring support oscillates regularly. The kinetic friction may be defined as the average of this force, which should approach zero as the velocity goes to zero. For the soft spring scenario, the particle's motion can be divided into a "slow" phase and a "fast" phase. During the slow phase, the particle climbs the potential well. During the fast phase, the particle quickly jumps from one stable position to another and dissipates energy as it undergoes damped oscillatory motion before coming to rest. In this case, there is a finite kinetic friction force even as the velocity approaches zero. This fact is illustrated by the hysteresis shown in the plot.

6.1.4   Fundamental friction mechanisms

The two primary fundamental friction mechanisms are electronic and phononic friction with coefficients Γ_{el} and Γ_{ph} respectively. Together these mechanisms are responsible for the microscopic friction coefficient, $\Gamma = \Gamma_{el} + \Gamma_{ph}$.

Electronic friction is caused by the excitation of electron-hole pairs. With physiosorption, a vibrating neutral molecule interacts with a metallic substrate via its electric dipole moment. In this case, the electronic friction is generally in the range $\Gamma_{el} \sim 10^8 - 10^9$ Hz. Whereas with chemiosorption, the vibrating molecule interacts with the substrate through its small effective charge. The electronic friction is higher with $\Gamma_{el} \sim 10^{10} - 10^{12}$ Hz. Notably, electronic friction only occurs above a conducting surface[83].

Phononic friction is caused by the excitation of surface or bulk phonons. By viewing the particle's oscillations as collisions with the surface, it is possible to crudely approximate the magnitude of phononic friction. During each collision, we expect an energy transfer of $\Delta E \approx E(m/m_{eff})$ where E is the energy of vibration and m_{eff} is the effective mass of the substrate. The effective mass of the substrate may be estimated by only considering the portion of substrate affected during the collision, which is assumed to last for $\tau \approx 1/\omega$ where ω is the resonance frequency of the particle in the potential U. Thus, $m_{eff} \approx \rho(c_s/\omega)^3$ where ρ is the density of the substrate and c_s is the velocity of sound. Assuming the frequency of collisions is given by ω, we can calculate the energy transferred per unit time though the differential equation, $dE/dt \approx -\omega(m/m_{eff})E$. This equation has

a damping constant, which corresponds to the phononic friction, given by[83]:

$$\Gamma_{\mathrm{ph}} \approx \frac{m\omega^4}{\rho c_{\mathrm{s}}{}^3}.$$ (6.14)

6.2 Experiment

The experimental requirements for measuring frictional forces during nanotube telescoping are similar to those described for nanotube buckling in Ch. 5. The TEM is necessary as it is the only microscope capable of observing telescoping behavior with atomic resolution. Also, AFM remains the best way of measuring the sub-nanonewton forces involved. Thus, we use an experimental setup that is very similar to the one used for buckling force measurements: a TEM nanopositioning system outfitted with a standard AFM cantilever.

There is, however, an important additional complication. For this experiment, choosing an AFM cantilever with an appropriate effective spring constant is critical. As the force resolution is limited by the resolution of the TEM, greater cantilever deflections, or equivalently softer spring constants, offer increased force sensitivity. However, at the same time, softer spring constants lead to stick-slip motion, which obscures information of the interlayer potential. We found that cantilevers with $k_{\mathrm{eff}} \approx 0.3$ nN/nm were a good compromise between these competing design goals. Though in some experiments, we purposefully chose softer spring constants in order to study stick-slip motion.

Figure 6.3(A) is a schematic of our experimental setup. A MWNT protrudes from a mobile piezo-controlled support (Pt wire) at the bottom of the schematic. The outer few walls of the MWNT are peeled away via electrostatic discharge[79] to reveal the inner
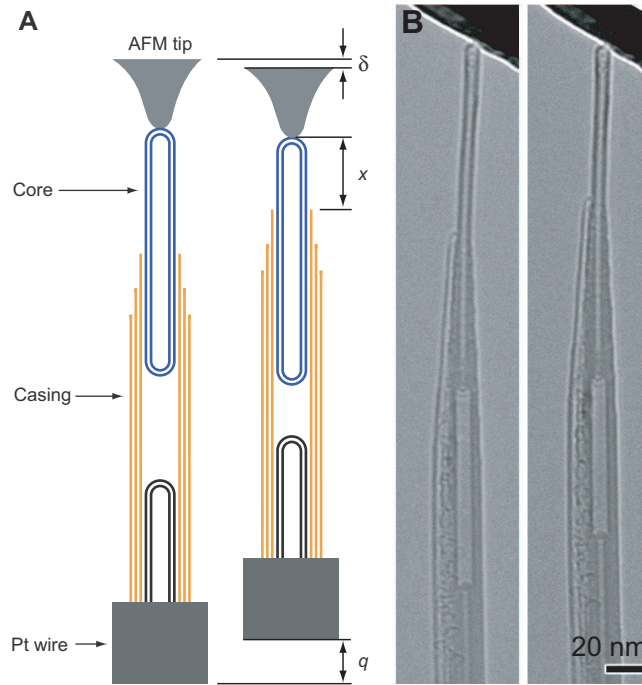
Figure 6.3: Schematic of nanotube friction measurement experiment and corresponding TEM image.

nanotube. We refer to the outer nanotube as the casing nanotube and the inner nanotube as the core nanotube. The core nanotube is attached to the tip of an AFM cantilever. By moving the support up and down, we controllably slide the nanotube casing inward and outward. At the same time, we monitor the deflection of the AFM cantilever and thus measure the force exerted by the interlayer potential. Figure 6.3(B) shows corresponding TEM images of a telescoping nanotube system.

The relevant variables in this experiment are the distance the support moves, q, the relative position of the core nanotube to the casing nanotube, x, and the deflection of the AFM cantilever, δ. These variables correspond to the variables discussed when describing stick-slip friction in Sec. 6.1.3. An image processing routine, similar to the one in Ch. 5,
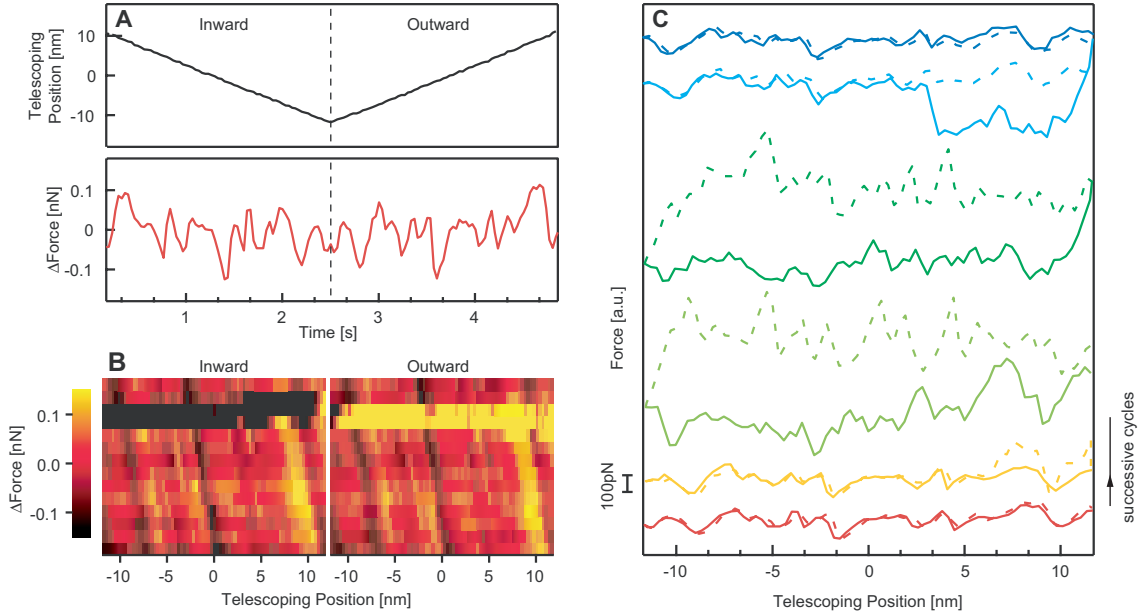
Figure 6.4: Interlayer forces in telescoping nanotubes. (A) Raw data showing the mobile support position and the measured force during a single inward and outward cycle. (B) Force map of telescoping system over multiple cycles. (C) Different method of representing the force data from successive cycles, which highlights the effects of friction. Inward sweeps are solid lines while outward sweeps are dashed lines.

automatically determines both the support travel distance q and the cantilever deflection δ. From these parameters it is possible to infer changes in x. Typical position sensitivity from the image processing routine was on the order of 1.6 Å. For a 0.3 N/m spring constant, this corresponds to a force sensitivity of 48 pN.

Data from a typical experiment are shown in Fig. 6.4(A). The top plot shows the position of the mobile support, q, as a function of time during a single inward and outward cycle. The bottom plot shows the changes in force experienced by the AFM cantilever, $\Delta F = k_{eff}\delta$, during the same time interval. The spring constant used in these experiments was $k_{eff} = 0.26$ nN/nm. The force signature is symmetric for the inward and outward sweeps as expected for a conservative interlayer potential.

Figure 6.4(B) is a force map displaying force versus q for multiple inward and outward cycles. The color represents the change in force, the horizontal axis represents q, and vertical axis represents successive cycles. The force signature remains constant for inward and outward sweeps over multiple cycles. Though, some hysteresis, representing friction, is present for the top few cycles.

Figure 6.4(C) shows a different method of displaying the force data from successive cycles. Here inward sweeps are solid lines and outward sweeps are dashed lines. Each color represents a different cycles starting with red and ending with blue. This method of displaying force signatures is particularly relevant to friction as the energy dissipated due to friction is given by the closed loop integral of the force times the position, or the area between the solid and dashed curves.

6.3 Analysis

As Fig. 6.4 shows, we have made detailed measurements of the forces between telescoping nanotubes. But, what causes these forces? And, what information about the nanotube or about friction in general can we extract from them? Here we interpret the data from Fig. 6.4 and from other telescoping nanotube experiments.

6.3.1 Interlayer potential

The interlayer potential between the nanotube core and casing is dominated by a van der Waals attraction, just as for layers of graphite. This van der Waals potential is proportional to the overlap area between the core and casing nanotube: $U_{\mathrm{vdw}}(x) = \gamma C x$

where γ is the van der Waals energy per unit area, C is the circumference of the core, and x is the overlap length. So far, we have assumed that the van der Waals attraction is uniform, but this does not account for the crystal structure of the nanotubes nor the presence of defects. Thus, we expect a corrugated potential $\Delta U(x)$ on top of the constant van der Waals potential.

Of course we do not measure the potential directly; rather, we measure the force, $F(x) = -\frac{dU}{dx}$. This force can be divided into a contribution from the constant van der Waals potential, f_{vdw} and a contribution from the corrugation, f_{corr}. Also, the system is not necessarily conservative, so there may be an additional frictional force, f_{fric}. Thus the total force between the core and the casing nanotube is

$$F(x) \ = \ f_{\mathrm{vdw}} + f_{\mathrm{corr}} + f_{\mathrm{fric}} \tag{6.15}$$

$$= \ -\gamma C - \frac{d}{dx}\Delta U(x) + f_{\mathrm{fric}}. \tag{6.16}$$

To measure the van der Waals force, we completely extract the nanotube core from its casing. During slow extraction (15 nm/s), the force is characterized by a constant background superimposed with stick-slip events, as shown in Fig. 6.5. Complete extraction results in an abrupt decrease in force of 3.1 nN, occurring in less than 30 ms (the time between consecutive TEM video frames). This is the van der Waals force. From the van der Waals force and from the diameter of the nanotube, we calculate a value for the cohesive surface energy between nanotube shells of 0.2 J/m^2, in good agreement with theoretical predictions[138, 76, 139].

The corrugation force was measured in Fig. 6.4. The corrugation appears to have a magnitude of approximately 0.1 nN and, though there is no obvious periodic structure,
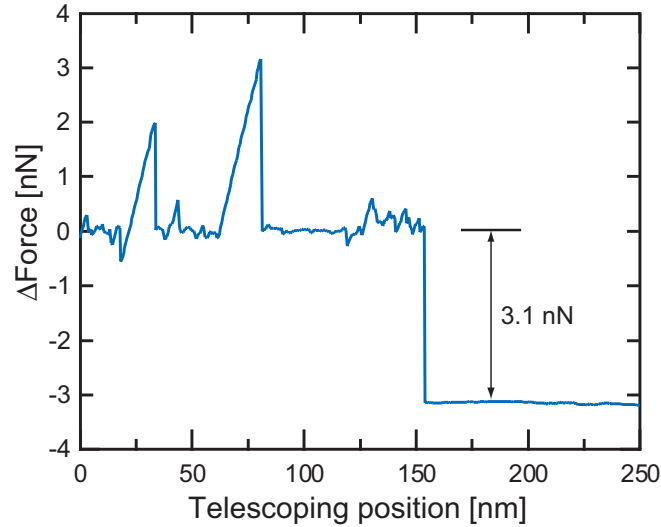
Figure 6.5: As the nanotube core is slowly extracted from its casing, the van der Waals interaction between the core and casing nanotubes applies a relatively constant force, superimposed with a few stick-slip events. Once the core is completely extracted, the sudden decrease in force on the AFM cantilever represents the magnitude of the van der Waals force.

it appears to have a characteristic length of a few nanometers. As mentioned above, this force could be caused by the crystal structure of the nanotube or by the presence of defects. Though one might expect the corrugation from a crystal structure to be periodic, this is not necessarily the case for nanotubes as the ratio of the unit cell lengths of the core and casing nanotube are likely incommensurate[140]. More likely however, due to the amplitude of the corrugation, these irregular forces are the result of interactions between defects on the core nanotube with the shell nanotube or vis a versa.

Frictional forces appear as differences in the force signatures between inward and outward sweeps. Such forces are apparent in a few of the cycles in Fig. 6.4(B) and Fig. 6.4(C). However, the inward and outward signatures for most cycles are equivalent to within the resolution of our instrument, 42 pN. Thus, we can put a limit of the frictional forces

present in this telescoping nanotube system of 42 pN or 1.4×10^{-15} N/atom. This is less than the previous upper bound on friction between telescoping nanotubes of 2.3×10^{-14} N/atom[76]. Moreover, this is lower than the observed friction between C_{60} islands and NaCl, one of the least dissipative nanoscale interfaces.

6.3.2 Self-repairing nanotube bearings

All mechanical systems, even nanomechanical systems, eventually experience wear. In macroscopic systems, surfaces become rough, chips of material break off, and cracks form. Whereas in nanoscale systems, bonds form between sliding surfaces, atoms are knocked out of the crystal lattice, and defects migrate. What effect will such damage have on nanomechanical systems? And more importantly, is there a way to repair it? To address these questions, we purposely damage our telescoping nanotube system using the TEM's electron beam.

The TEM's 100 keV electron beam can eject carbon atoms from a nanotube through single electron-carbon collisions, also known as knock-on collisions[141]. The extent of this damage may be controlled, to some degree, through adjusting the electron beam's intensity. For our experiments, we used an electron flux of 2.5×10^4 e$^-$/nm^2·s, which assuming a displacement energy of 17 eV[142] will result in 5×10^{-5} displacements per atom per second, or approximately 3 displacements per second for a typical telescoping interface. While controllably damaging the telescoping system, we slide the core nanotube in and out multiple times and monitor the interlayer forces.

As Fig. 6.4(B) shows, our nanoscale device is indeed damaged by electron ir-

radiation. Near the top of the force map, prominent horizontal dark and bright streaks, visible for both the inward and outward direction of motion, indicate hysteresis in the force versus telescoping position loop. These features are shown in more detail in Fig. 6.4(C). This dissipative motion can be attributed to the creation of one or more vacancies on the telescoping interface[143].

Fortunately, damage to the telescoping system is easily repaired. Just two cycles after friction initially appears, the original, nearly frictionless force signature returns, as seen in the the upper traces in Fig. 6.4(B) and Fig. 6.4(C). The continuous telescoping movement promotes dangling bond saturation and Stone-Wales defect formation[144], and thus optimizes the atomic structure and restores the original force signature. Due to the stability of their atomic structure, carbon nanotubes have the fascinating ability to self-repair, absorbing damage that could otherwise lead to dissipation and jamming. Obviously, such an ability is a unique feature of nanomechanical systems.

6.3.3 Stick-slip friction

Our experimental system most closely resembles the stick-slip model presented in Sec. 6.1.3. To determine the applicability of this model, we operated a telescoping nanotube system in both the soft and stiff spring regimes. This data from this experiment is presented in Fig. 6.6.

The soft spring regime, shown in Fig. 6.6(A), is characterized by stick-slip motion. The general shape of this plot resembles the theoretical force versus displacement curve for the soft spring case shown at the bottom of Fig. 6.2(B). The slanted lines on the left and
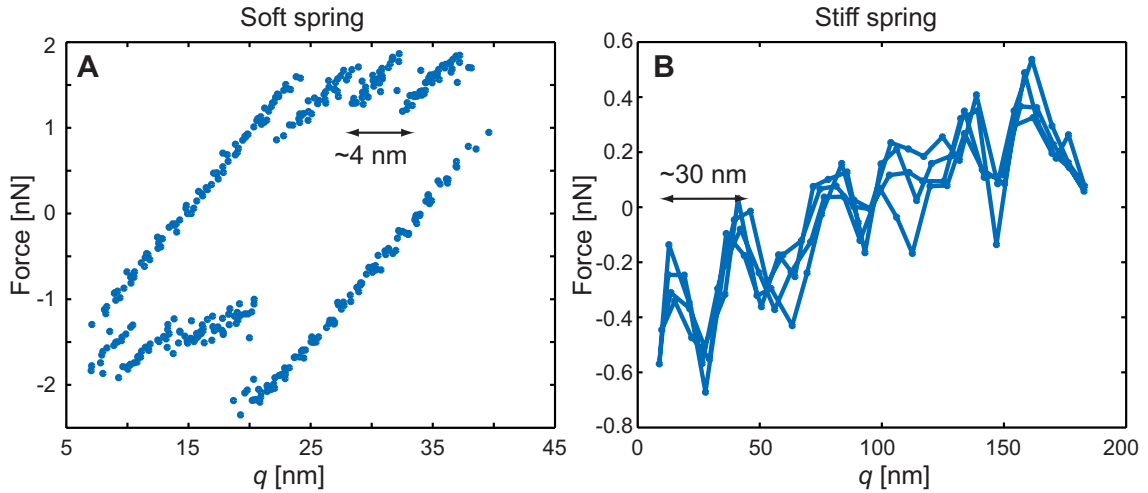
Figure 6.6: Stick-slip friction in the soft and stiff regimes. The forces on two different telescoping nanotubes are plotted as a function of the position of the mobile support. (A) In the soft spring regime, friction is evident in a hysteresis loop. Discontinuous jumps in the force hint at the corrugation period. (B) In the stiff spring regime, there is no measurable hysteresis; however the corrugated potential can still be seen in the oscillating force.

right of the loop and the shorter, slanted lines, three of which are clearly visible on the top of the loop, represent the slow phase of motion. The particle, in this case the entire nanotube core, climbs the effective potential until it quickly transitions to another well. The fast transition phase is marked by the sharp changes in force. On the top of the loop, these changes occur with an approximate period of 4 nm, which may represent the length of the unit cell of one of the nanotubes, or may represent the spacings of defects. The frictional force is given by half the height of the loop, or approximately 1.5 nN.

In the stiff spring regime, shown in Fig. 6.6(B), the stick-slip motion is suppressed and the only remaining friction is sliding or Brownian friction. Our current setup is not sensitive enough to measure these values. We can set an upper limit on them based on the sensitivity of our setup, which is currently roughly 42 pN.

Interestingly, both sets of data, soft and stiff spring, were taken with the same

effective spring constant, $k_{\text{eff}} = 0.3$ N/m, but on different telescoping nanotube systems. The change from soft to stiff spring regimes is thus a result of the different nature of the potentials. It is easily seen by examining Fig. 6.6 that the potential for the soft spring data had a larger U_0 and a smaller a than the stiff spring data, as expected. More precisely, the amplitude of the potential for Fig. 6.6(A) is approximately $U_0 \approx 9.5 \times 10^{-19}$ J and the characteristic length is $a = 4$ nm. Thus the critical spring constant, derived in Sec. 6.1.3, is $k_c = 4\pi^2 U_0/a^2 = 2.3$ N/m. As expected for a soft spring system, the spring constant of the AFM is less than this value. The potential for Fig. 6.6(B) is approximately $U_0 \approx 9.5 \times 10^{-19}$ J and the characteristic length is $a = 30$ nm. Thus the critical spring constant here is $k_c = 0.04$ N/m. Again, as expected for a stiff spring system, the spring constant of the AFM is greater than this value.

6.3.4 Limits on sliding friction

Once the nanotube core detaches from the AFM cantilever and is free to slide within the casing, the sliding friction model becomes appropriate. There is only a very brief period when this situation is observed. In fact, the nanotube core, pulled by the van der Waals force, completely retracts into its casing within the time of a single TEM video frame (30 ms). From this simple observation it is possible to put a limit on the sliding friction coefficient.

Clearly, the frictional force must be less than the van der Waals force. We have already measured the van der Waals force from the data presented in Fig. 6.5. Also, we know that the nanotube core's velocity must be greater than $v_{\text{min}} = 5.1\mu$m/s from the fact that it

completely retracts into the casing, over a distance of 154 nm, in less than 30 ms (the time between successive TEM video frames). Finally, the mass of the nanotube core, determined from TEM images, is $m_{\text{core}} = 1.2 \times 10^{-20}$ kg. Thus, $\overline{\Gamma} < f_{\text{vdw}}/m_{\text{core}}v_{\text{min}} = 5.1 \times 10^{16}$ Hz. As we are in the large force limit of sliding friction and thus $\overline{\Gamma} \approx \Gamma$, our results imply that $\Gamma < 5.1 \times 10^{16}$ Hz, consistent with the fundamental friction values mentioned in Sec. 6.1.4.

6.4   Discussion

Using our technique for operating an AFM inside a TEM, we have made detailed measurements of the interlayer potential and frictional forces between telescoping nanotubes. Under the appropriate conditions, the telescoping interface is frictionless to within the precision of our instrument, which implies that any frictional forces are less than 42 pN or 1.4×10^{-15} N/atom. When friction does appear it is either the result of electron beam induced damage to the nanotube's crystal structure or the result of the AFM cantilever's soft spring constant, which leads to stick-slip friction. Electron beam induced damage can be repaired through continual telescoping motion. Stick-slip friction can be avoided simply by choosing a stiffer spring constant. Our friction measurements are well-described by the sliding and stick-slip friction models. Refinements to this experiment, such as a faster TEM video camera, could enable improved experimental limits on the sliding friction coefficient.

Part III

Nanofluidics

Chapter 7

Current-controlled nanotube growth and zone refinement

The remarkable properties of carbon nanotubes (CNTs) are sensitive to geometrical details, which depend intricately on the method of nanotube growth[5, 145, 146]. As such, much effort has been devoted to studying CNT synthesis and growth mechanisms. Different methods presently exist for CNT production, including arc-discharge[147], chemical vapor deposition[148], laser vaporization[149], and high-pressure oxide reactions[150], most using transition metal catalysts to facilitate the reaction. Unfortunately, none of these bulk synthesis methods affords truly controlled growth, whereby a CNT can be grown at a precisely determined rate with pre-selected diameter, length, and defect concentration.

We here present two novel reaction methods by which the growth of a single CNT can be controlled using an electrical current. In the first method, a CNT grows inside a preformed nanotube reaction chamber. The synthesis rate is adjustable, and the growth of

a single CNT can be stopped and restarted at will. In the second closely related method, a preexisting marginal quality multi-walled CNT is zone-refined into a higher quality multi-walled CNT, again in a controlled manner. Here the current-controlled refinement process proceeds axially down the CNT, and can be terminated at will to create precisely placed junctions between nanotube segments with different electrical characteristics.

Our experimental configuration exploits the well-known critical role transition metal catalysts play in CNT growth as well as the ability to incorporate metals within[151] and transport metals along[111, 152] preformed nanotubes. Multi-walled CNTs containing cobalt catalyst nanoparticles in their interior were synthesized through the pyrolysis of cobaltocene[153]. A mat of cobalt-filled nanotubes was then glued to a platinum wire with conducting silver epoxy and mounted to a custom-made piezo-controlled nanomanipulation stage, operated inside a transmission electron microscope (TEM). Inside the TEM, the free end of a single nanotube was approached and contacted with an etched tungsten tip, thus completing a circuit between the grounded tungsten tip and the sample that can be held at an arbitrary voltage.

7.1 Experiment

Figure 7.1 shows a schematic of our experimental setup and distinguishes the two modes of operation. Figure 7.1(A) shows what we term the "ink reservoir" method of nanotube growth. A cobalt catalyst nanoparticle, initially containing dissolved carbon (the "ink"), is confined within the interior of a preformed nanotube, which serves as the reaction chamber. An electrical current I runs through the reaction chamber nanotube, causing the
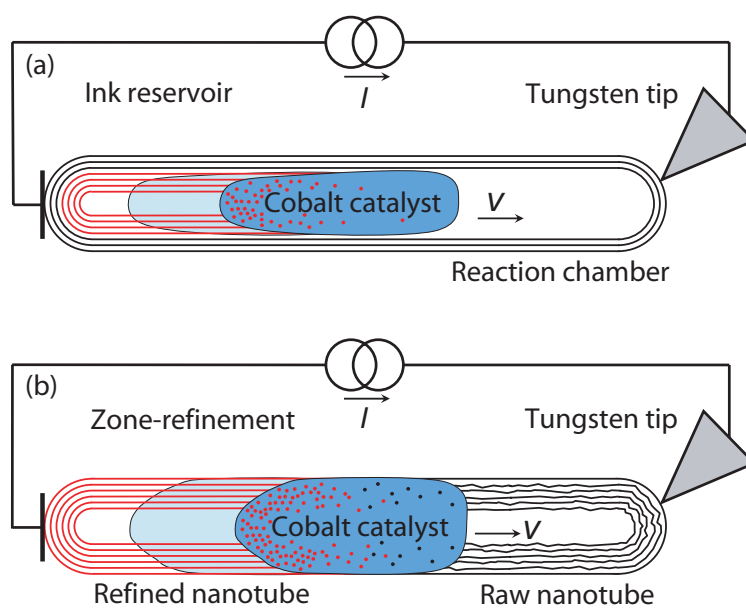
Figure 7.1: Schematic diagrams of the two modes of operation. The etched tungsten tip of a nanomanipulator contacts a single nanotube anchored inside a TEM, thus completing a circuit. By running current through the system, it is possible to controllably move the catalyst particle with velocity v. (A) Ink reservoir method. As the catalyst moves, carbon initially dissolved in the catalyst particle (the "ink") precipitates out and forms a new high-quality CNT (red). (B) Zone-refinement method. The catalyst particle continuously refines the raw, defective nanotube on the right (black) into a higher quality nanotube on the left (red).

catalyst particle to melt and move to the right at velocity v, streaming out a newly formed CNT in its wake. The outer diameter of the new CNT is dictated by the inner diameter of the reaction chamber, and the speed at which the catalyst particle ejects the new CNT is controlled by I. CNT growth ceases when the cobalt catalyst particle exhausts its feedstock of dissolved carbon. Figure 7.1(B) shows the "zone-refinement" configuration. A preformed nanotube of marginal quality contains a cobalt catalyst nanoparticle, which encompasses its entire cross-section. An electrical current I again runs axially through the nanotube, causing the cobalt nanoparticle to melt and move to the right. In doing so, the original nanotube is consumed by the catalyst nanoparticle and a higher quality CNT is grown and ejected from the trailing end. In this continuous process there is no carbon feedstock limitation and the entire original nanotube can be zone-refined into a higher quality CNT.

We first examine the ink reservoir method of controlled CNT growth. Figure 7.2 shows a time sequence of TEM video images depicting the movement of a cobalt catalyst particle through the core of the nanotube reaction chamber. The grounded tungsten tip contacts the right side of the nanotube while the sample side is held at a negative potential (both out of view). With increasing I, Joule heating melts the catalyst particle (dark cigar-shaped object), and electric field effects generate a force that displaces it towards the anode on the right. In Fig. 7.2(B) the current is ramped to 60 μA, and the catalyst particle distorts in shape and begins moving to the right. The formation of a new CNT endcap can just be resolved near the left end of the catalyst particle. Further increasing I increases the velocity v of the catalyst particle. Between Fig. 7.2(C) and 7.2(D), both with $I = 130$ μA, the catalyst travels 68 nm in less than 0.1 s yielding $v = 680$ nm/s.
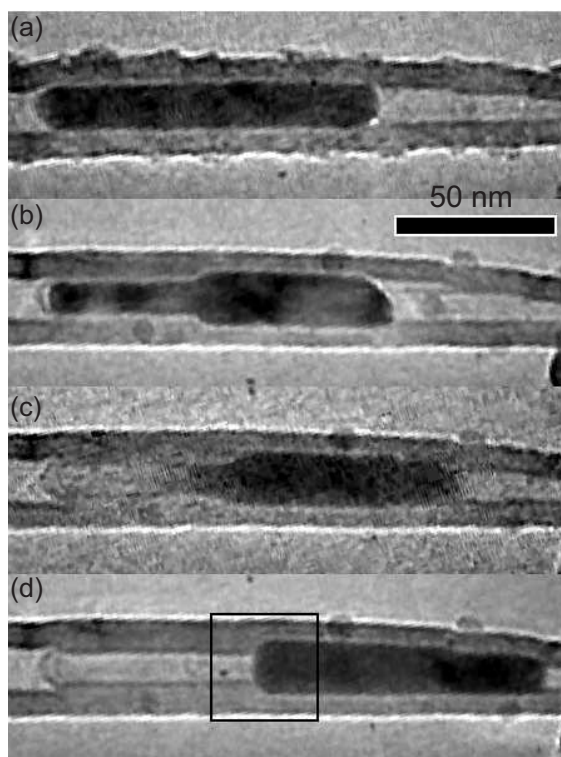
Figure 7.2: A time sequence of TEM video images showing the controlled movement of a cobalt catalyst particle. (A) The catalyst particle (dark cigar-shaped object) rests within the interior of a nanotube reaction chamber. (B) As the current is ramped to 60 μA, the particle deforms and begins to move. (C) At 130 μA, the particle slides through the core of the nanotube. (D) The particle finally comes to rest. Behind it, a new CNT has formed as evidenced by the reduced diameter of the core of the nanotube.
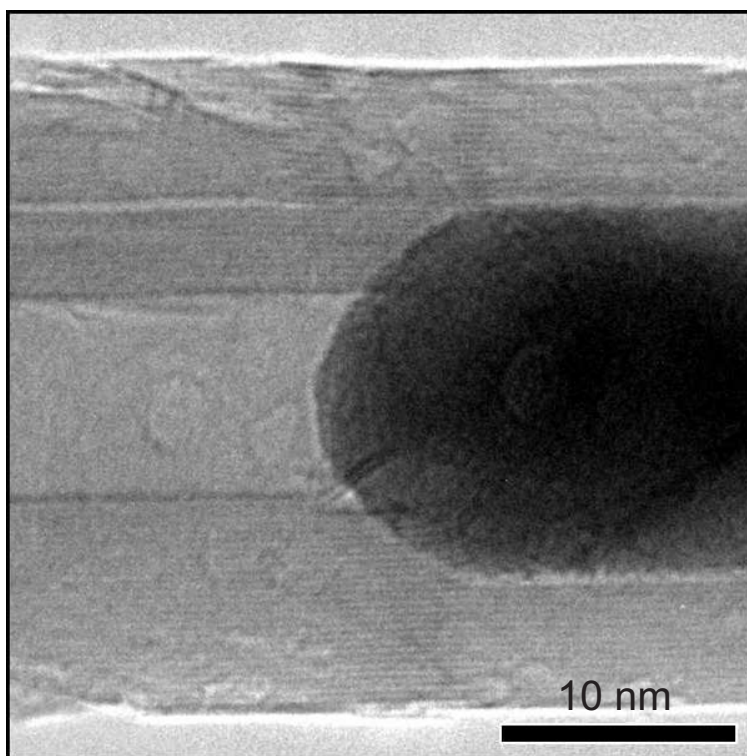
Figure 7.3: TEM micrograph of a high-quality multi-walled CNT growing within the core of a larger nanotube reaction chamber. This is the area outlined in Fig. 7.2(D). The image clearly shows the formation of a new 11-wall CNT streaming from the end of the catalyst particle. The newly formed CNT walls have no detectible defects, even at the interface with the more defective nanotube reaction chamber.

As the catalyst particle moves to the right within the nanotube reaction chamber, it ejects behind it a new multi-walled CNT whose outer diameter precisely fits within the inner diameter of the nanotube reaction chamber. The newly formed CNT in Fig. 7.2 has an inner and outer diameter of 11 nm and 14 nm, respectively. Interestingly, the growth speed $v = 680$ nm/s is comparable to that reported for typical CVD grown nanotubes[154].

Importantly, the speed of CNT growth, which is closely related to CNT defect density, is controllable via I. The CNT grown in Fig. 7.2 is of a remarkably high quality, in fact of a much higher quality than the pyrolysis-produced reaction chamber nanotube.

Figure 7.3 shows a high-resolution TEM micrograph of the outlined area in Fig. 7.2(D). In stark contrast to the reaction chamber nanotube, which has curved, defect-filled walls, the newly formed CNT ejected from the catalyst particle has virtually perfect walls with no detectible defects, even near the interface with the reaction chamber. Figure 7.3, essentially a snapshot of catalytic CNT growth, contains a wealth of information pertinent to nanotube formation. Among other things the figure shows several sequential double graphene sheets emerging from the catalyst particle at an angle to the walls of the newly formed CNT. This demonstrates that, in this growth process, CNT walls are laid down or "paved" on top of each other from the outside in, rather than simply being ejected from the catalytic particle simultaneously. Atomic resolution videos capturing the synthesis of multi-walled CNTs in action have obvious implications for the thermodynamic analysis of nanotube synthesis.

In the ink reservoir method of CNT formation, growth ceases when the catalyst particle depletes its feedstock of dissolved carbon. For the new CNT shown in Fig. 7.2, growth was limited to about 70 nm. The volume of the catalyst particle decreases as it expels the new CNT (by 760 nm^3 from the initial volume of 1.6×10^4 nm^3). Attributing the entire volume loss to carbon, we estimate that the catalyst particle initially contained approximately 5.9 atomic percent carbon.

We next examine the zone-refinement method of controlled CNT growth described in Fig. 7.1(B). Figure 7.4 shows a time sequence of TEM video images taken at 10 s intervals depicting a catalyst particle refining a multi-walled carbon nanotube. A constant current of 240 μA runs though the nanotube. The catalyst particle encompasses the entire diameter of the nanotube, and as it advances towards the anode (out of view to the right), it cannibalizes
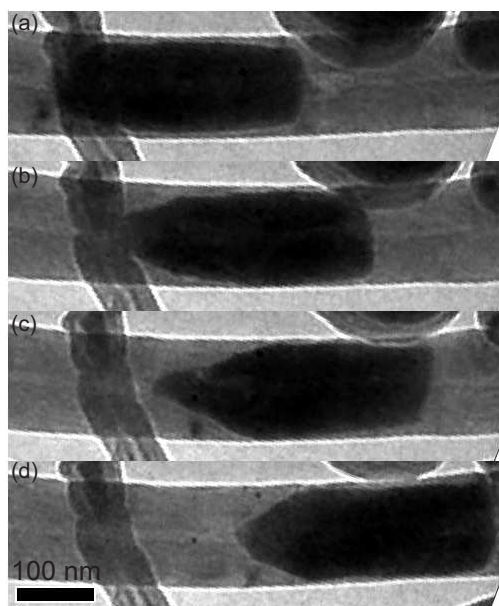
Figure 7.4: A time sequence of TEM video images at 10 s intervals showing a cobalt catalyst particle cannibalize a raw nanotube to its right and reform a CNT to its left as it moves toward the anode. The resistance of the entire nanotube system decreases as the catalyst advances demonstrating that the catalyst particle is refining the nanotube and removing defects.

raw nanotube at its front and reforms it into new, higher quality CNT at its rear. Over the course of the experiment, the resistance of the entire nanotube (raw and reformed) is found to decrease by 6% following the advance of the catalyst along the full 3 μm length of the nanotube. Hence, the refined nanotube has a significantly enhanced electrical conductance, which is consistent with a decreased defect concentration. In contrast to the ink reservoir method, in the zone refining method a constant supply of carbon ingested at the head of the catalyst particle allows for essentially unlimited dissolution and precipitation of CNTs.

7.2 Analysis

What is the nature of the driving force causing the catalyst particles to move in response to the electric current I? The carbon supply's effect on transport suggests that the electromigration of carbon in cobalt drives the motion. Previous experiments have shown that carbon ions move toward the cathode in cobalt[155]. Here the direct electrostatic force on the carbon ions dominates over the "electron wind" force resulting from the momentum transfer between electrons and ions[156]. As a result a carbon concentration gradient develops across the catalyst particle. Eventually, the side of the particle near the cathode becomes supersaturated with carbon causing the carbon to precipitate. The maximum carbon concentration, n_{max}, may be calculated from the 12.75 atomic percent carbon that cobalt in its liquid state near the melting point can accommodate[157]. When the carbon precipitates, it forms new concentric nanotube shells that displace the cobalt as demonstrated in Fig. 7.2(B). To minimize surface energy, molten cobalt will minimize contact surface area with the nanotube. Thus, as shown in Fig. 7.2(C) and Fig. 7.2(D), surface tension forces the catalyst particle out of the region narrowed by new CNT formation, and the catalyst particle moves forward.

This mechanism for nanotube growth is similar to the vapor-liquid-solid mechanism traditionally used to describe the growth of CNTs[158]. In the vapor-liquid-solid model, a liquid catalyst particle preferentially absorbs carbon from the vapor, becomes supersaturated, and precipitates carbon in the more energetically favorable graphitic, nanotube form. In our zone-refinement experiments there is no vapor; however, because of the voltage-induced concentration gradient, the liquid catalyst particle preferentially absorbs

solid carbon from the front of the particle near the anode and precipitates it out at the rear near the cathode. Previous experiments have reported a similar solid-liquid-solid mechanism of nanotube growth[159, 160] but without the field-induced concentration gradient.

To test our model, we estimate the current density necessary to initiate movement by calculating the electric field required to increase the carbon concentration to n_{max} on the side of the particle near the cathode. The carbon concentration across the cobalt particle in the steady state is given by combining the Nernst-Einstein equation with the diffusion equation,

$$n\frac{D}{k_{\mathrm{B}}T}Z^0e\vec{E} = -D\vec{\nabla}n, \tag{7.1}$$

where n is the ion concentration, D is the diffusion constant, k_{B} is the Boltzmann constant, T is the temperature, Z^0 is the effective valence of the ion, e is the charge of an electron, and $\vec{E}$ is the electric field[156]. Here the effective valence, Z^0, represents contributions from both the direct electrostatic force and the "wind force." Solving this equation in one dimension yields a decaying exponential for the distribution of the carbon ion concentration across the catalyst particle, $n(x) = n(0)\exp\left(-Z^0e|E|x/k_{\mathrm{B}}T\right)$. According to our model, carbon will precipitate and the particle will move when $n(0) = n_{\mathrm{max}}$. The mean ion concentration, $\bar{n}$, and the length of the catalyst particle, L, provide the final constraint required to calculate $|\vec{E}|$. For the particle displayed in Fig. 7.2(A), assuming the precipitation of all the initial carbon is responsible for the noted volume change, we find $\bar{n} = 5$ ions/nm^3. With $Z^0 = 10$[156], $n_{\mathrm{max}} = 10$ ions/nm^3, $T = 1000$ K[161, 162], and $L = 105$ nm, we determine $|\vec{E}| \approx 1.3 \times 10^{-4}$ V/nm. Assuming all current passes through the cobalt catalyst particle and using the resistivity of pure cobalt ($\rho_{\mathrm{Co}} = 5.6 \times 10^{-8}$ $\Omega \cdot$ m[163]), we calculate that

$I \approx 300 \ \mu\text{A}$, the same magnitude as experimentally observed values.

7.3 Discussion

Our technique offers the unique opportunity both to study nanotube growth with atomic resolution in a controllable manner and to fine-tune the parameters of nanotube formation. Control over the velocity of the catalyst particle could be exploited to vary defect densities in the created nanotubes. In addition, the ability to freeze and restart nanotube growth could lead to the precise control of nanotube length or the tailored placement of nanotube caps. Engineering the defect densities, length, and cap locations in multi-walled CNTs may ultimately be applied to the creation of quantum dots[164] or other devices with interesting quantum scattering conditions[165].

Bibliography

[1] Sauerbrey, G. Verwendung von schwingquarzen zur wagung dunner schichten und zur mikrowagung. *Zeit. Phys.* **155**, 206–222 (1959).

[2] Cleland, A. N. & Roukes, M. L. Fabrication of high frequency nanometer scale mechanical resonators from bulk Si crystals. *Appl. Phys. Lett.* **69**, 2653–2655 (1996).

[3] Craighead, H. G. Nanoelectromechanical systems. *Science* **290**, 1532–1535 (2000).

[4] Ekinci, K. L. & Roukes, M. L. Nanoelectromechanical systems. *Rev. Sci. Instrum.* **76**, 061101 (2005).

[5] Poncharal, P., Wang, Z. L., Ugarte, D. & de Heer, W. A. Electrostatic deflections and electromechanical resonances of carbon nanotubes. *Science* **283**, 1513–1516 (1999).

[6] Sazonova, V. *et al.* A tunable carbon nanotube electromechanical oscillator. *Nature* **431**, 284–287 (2004).

[7] Ekinci, K. L. Electromechanical transducers at the nanoscale: actuation and sensing motion in nanoelectromechancail systems (NEMS). *Small* **1**, 786 (2005).

[8] Mamin, H. J. & Rugar, D. Sub-attonewton force detection at millikelvin temperatures. *Appl. Phys. Lett.* **79**, 3358–3360 (2001).

[9] Knobel, R. G. & Cleland, A. N. Nanometre-scale displacement sensing using a single electron transistor. *Nature* **424**, 291–293 (2003).

[10] LaHaye, M. D., Buu, O., Camarota, B. & Schwab, K. C. Approaching the quantum limit of a nanomechanical resonator. *Science* **304**, 74–77 (2004).

[11] Ekinci, K. L., Yang, Y. T. & Roukes, M. L. Ultimate limits to inertial mass sensing based upon nanoelectromechanical systems. *J. Appl. Phys.* **95**, 2682–2689 (2004).

[12] Armour, A. D., Blencowe, M. P. & Schwab, K. C. Entanglement and decoherence of a micromechanical resonator via coupling to a Cooper-pair box. *Phys. Rev. Lett.* **88**, 148301 (2002).

[13] Hopkins, A., Jacobs, K., Habib, S. & Schwab, K. Feedback cooling of a nanomechanical resonator. *Phys. Rev. B* **68**, 235328 (2003).

[14] Martin, I., Shnirman, A., Tian, L. & Zoller, P. Ground-state cooling of mechanical resonators. *Phys. Rev. B* **69**, 125339 (2004).

[15] Wilson-Rae, I., Zoller, P. & Imamoglu, A. Laser cooling of a nanomechanical resonator mode to its quantum ground state. *Phys. Rev. Lett.* **92**, 075507 (2004).

[16] Naik, A. *et al.* Cooling a nanomechanical resonator with quantum back-action. *Nature* **443**, 193–196 (2006).

[17] Landau, L. D. & Lifshitz, E. M. *Mechanics*. Butterworth-Heinenann, Oxford, 3rd edition, (1993).

[18] Mohanty, P. *et al.* Intrinsic dissipation in high-frequency micromechanical resonators. *Phys. Rev. B* **66**, 085416 (2002).

[19] Hutchinson, A. B. *et al.* Dissipation in nanocrystalline-diamond nanomechanical resonators. *Appl. Phys. Lett.* **84**, 972 (2004).

[20] Houston, B. H. *et al.* Thermoelastic loss in microscale oscillators. *Appl. Phys. Lett.* **80**, 1300 (2002).

[21] Verbridge, S. S., Craighead, H. G. & Parpia, J. M. A megahertz nanomechanical resonator with room temperature quality factor over a million. *Appl. Phys. Lett.* **92**, 013112 (2008).

[22] Judge, J. A., Photiadis, D. M., Vignola, J. F., Houston, B. H. & Jarzynski, J. Attachment loss of micromechanical and nanomechanical resonators in the limits of thick and thin support structures. *J. Appl. Phys.* **101**, 013521 (2007).

[23] Wang, K., Wong, A. C. & Nguyen, C. T. VHF free-free beam high-Q micromechanical resonators. *J. Microelectromech. Syst.* **9**, 347 (2000).

[24] McGuigan, D. F., Lam, C. C., Gram, R. Q., Hoffman, A. W. & Douglass, D. H. Measurements of mechanical Q of single-crystal silicon at low-temperatures. *J. Low Temp. Phys.* **30**, 621 (1978).

[25] Kleiman, R. N., Agnolet, G. & Bishop, D. J. Two-level systems observed in the

mechanical properties of single-crystal silicon at low temperatures. *Phys. Rev. Lett.* **59**, 2079 (1987).

[26] Buser, R. A. & DeRooij, N. F. Very high Q-factor resonators in monocrystalline silicon. *Sens. Actuators, A* **21**, 323 (1990).

[27] Greywall, D. S., Yurke, B., Busch, P. A. & Arney, S. C. Low-temperature anomalies in the dissipation of small mechanical resonators. *Europhys. Lett.* **34**, 37 (1996).

[28] Feng, X. L., He, R. R., Yang, P. D. & Roukes, M. L. Very high frequency silicon nanowire electromechanical resonators. *Nano Lett.* **7**, 1953–1959 (2007).

[29] Jensen, K., Kim, K. & Zettl, A. An atomic-resolution nanomechanical mass sensor. *Nature Nano.* (2008).

[30] Yang, J., Ono, T. & Esashi, M. Surface effects and high quality factors in ultrathin single-crystal silicon cantilevers. *Appl. Phys. Lett.* **77**, 3860 (2000).

[31] Richter, A. M., Sengupta, D. & Hines, M. A. Effect of surface chemistry on mechanical energy dissipation: silicon oxidation does not inherently decrease the quality factor. *J. Phys. Chem. C* **112**, 1473 (2008).

[32] Lifshitz, R. & Roukes, M. L. Thermoelastic damping in micro- and nanomechanical systems. *Phys. Rev. B* **61**, 5600–5609 (2000).

[33] Cleland, A. N. *Foundations of Nanomechanics.* Springer-Verlag, New York, (2003).

[34] Petersen, K., Shartel, A. & Raley, N. F. Micromechanical accelerometer integrated with MOS detection circuitry. *IEEE Trans. Electron Devices* **29**, 23 (1982).

[35] Truitt, P. A., Hertzberg, J. B., Huang, C. C., Ekinci, K. L. & Schwab, K. C. Efficient and sensitive capacitive readout of nanomechanical resonator arrays. *Nano Lett.* **7**, 120–126 (2007).

[36] Masmanidis, S. C. *et al.* Multifunctional nanomechanical systems via tunable coupled piezoelectric actuation. *Science* **317**, 780 (2007).

[37] Peng, H. B., Chang, C. W., Aloni, S., Yuzvinsky, T. D. & Zettl, A. Ultrahigh frequency nanotube resonators. *Phys. Rev. Lett.* **97**, 087203 (2006).

[38] Cleland, A. N., Aldridge, J. S., Driscoll, D. C. & Gossard, A. C. Nanomechanical displacement sensing using a quantum point contact. *Appl. Phys. Lett.* **81**, 1699–1701 (2002).

[39] Cleland, A. N. & Roukes, M. L. External control of dissipation in a nanometer-scale radiofrequency mechanical resonator. *Sens. Actuators, A* **72**, 256–261 (1999).

[40] De Vlaminck, I. *et al.* Detection of nanomechanical motion by evanescent light wave coupling. *Appl. Phys. Lett.* **90**, 233116 (2007).

[41] Bocko, M. F., Stephenson, K. A. & Koch, R. H. Vacuum tunneling probe: a nonreciprocal, reduced-back-action transducer. *Phys. Rev. Lett.* **61**, 726 (1988).

[42] Flowers-Jacobs, N., Schmidt, D. R. & Lehnert, K. W. Intrinsic noise properties of atomic point contact displacement detectors. *Phys. Rev. Lett.* **98**, 096804 (2007).

[43] Kemiktarak, U., Ndukum, T., Schwab, K. C. & Ekinci, K. L. Radio-frequency scanning tunneling microscopy. *Nature* **450**, 85 (2007).

[44] Purcell, S. T., Vincent, P., Journet, C. & Binh, V. T. Tuning of nanotube mechanical resonances by electric field pulling. *Phys. Rev. Lett.* **89**, 276103 (2002).

[45] Jensen, K., Weldon, J., Garcia, H. & Zettl, A. Nanotube radio. *Nano Lett.* **7**, 3508–3511 (2007).

[46] Fowler, R. H. & Nordheim, L. Electron emission in intense electric fields. *Proc. R. Soc. London Ser. A* **119**, 173–181 (1928).

[47] Wang, X. Q., Wang, M., He, P. M., Xu, Y. B. & Li, Z. H. Model calculation for the field enhancement factor of carbon nanotube. *J. Appl. Phys.* **96**, 6752–6755 (2004).

[48] Dean, K. A., von Allmen, P. & Chalamala, B. R. Three behavioral states observed in field emission from single-walled carbon nanotubes. *J. Vac. Sci. Technol., B* **17**, 1959 (1999).

[49] Pathria, R. K. *Statistical Mechanics*. Butterworth-Heinemann, Oxford, 2nd edition, (1996).

[50] Cleland, A. N. & Roukes, M. L. Noise processes in nanomechanical resonators. *J. Appl. Phys.* **92**, 2758–2769 (2002).

[51] Mather, J. C. Bolometer noise - Non-equilibrium theory. *Appl. Opt.* **21**, 1125 (1982).

[52] Poggio, M., Degen, C. L., Mamin, H. J. & Rugar, D. Feedback cooling of a cantilever's fundamental mode below 5 mK. *Phys. Rev. Lett.* **99**, 017201 (2007).

[53] Peng, H. B., Chang, C. W., Aloni, S., Yuzvinsky, T. D. & Zettl, A. Microwave

electromechanical resonator consisting of clamped carbon nanotubes in an abacus arrangement. *Phys. Rev. B* **76**, 035405 (2006).

[54] Geller, M. R. & Cleland, A. N. Superconducting qubits coupled to nanoelectrome-chanical resonators: An architecture for solid-state quantum-information processing. *Phys. Rev. A* **71**, 032311 (2005).

[55] Blencowe, M. Quantum electromechanical systems. *Phys. Rep.* **395**, 159 (2004).

[56] Huang, S., Woodson, M., Smalley, R. & Liu, J. Growth mechanism of oriented long single walled carbon nanotubes using "fast-heating" chemical vapor deposition process. *Nano Lett.* **4**, 1025 (2004).

[57] Zwickl, B. M. *et al.* High quality mechanical and optical properties of commercial silicon nitride membranes. *Appl. Phys. Lett.* **92**, 103125 (2008).

[58] Armani, D. K., Kippenberg, T. J., Spillane, S. M. & Vahala, K. J. Ultra-high-Q toroid microcavity on a chip. *Nature* **421**, 925–928 (2003).

[59] Verbridge, S. S., Shapiro, D. F., Craighead, H. G. & Parpia, J. M. Substate bending for reversible control of frequency and quality factor of nanostring resonators. *Nano Lett.* **7**, 1728 (2007).

[60] Chu, S., Hollberg, L., Bjorkholm, J. E., Cable, A. & Ashkin, A. 3-dimensional viscous confinement and cooling of atoms by resonance radiation pressure. *Phys. Rev. Lett.* **55**, 48 (1985).

[61] Brown, K. R. *et al.* Passive cooling of a micromechanical oscillator with a resonant electric circuit. *Phys. Rev. Lett.* **99**, 137205 (2007).

[62] Thompson, J. D. *et al.* Strong dispersive coupling of a high-finesse cavity to a micromechanical membrane. *Nature* **542**, 72 (2008).

[63] Pellizzari, T., Gardiner, S. A., Cirac, J. I. & Zoller, P. Decoherence, continuous observation, and quantum computing: A cavity QED model. *Phys. Rev. Lett.* **75**, 3788 (1995).

[64] Ilic, B., Yang, Y. & Craighead, H. G. Virus detection using nanoelectromechanical devices. *Appl. Phys. Lett.* **85**, 2604 (2004).

[65] Ekinci, K. L., Huang, X. M. H. & Roukes, M. L. Ultrasensitive nanoelectromechanical mass detection. *Appl. Phys. Lett.* **84**, 4469–4471 (2004).

[66] Ilic, B. *et al.* Attogram detection using nanoelectromechanical oscillators. *J. Appl. Phys.* **95**, 3694–3703 (2004).

[67] Yang, Y. T., Callegari, C., Feng, X. L., Ekinci, K. L. & Roukes, M. L. Zeptogram-scale nanomechanical mass sensing. *Nano Lett.* **6**, 583–586 (2006).

[68] Mamin, H. J., Poggio, M., Degen, C. L. & Rugar, D. Nuclear magnetic resonance imaging with 90-nm resolution. *Nature Nano.* **2**, 302 (2007).

[69] Erbe, A. *et al.* Mechanical mixing in nonlinear nanomechanical resonators. *Appl. Phys. Lett.* **77**, 3102 (2000).

[70] Rugar, D. & P., G. Mechanical parametric amplification and thermomechanical noise squeezing. *Phys. Rev. Lett.* **67**, 699 (1991).

[71] Dragoman, M. *et al.* Nanoelectromechanical switches based on carbon nanotubes for microwave and millimeter waves. *Appl. Phys. Lett.* **90**, 113102 (2007).

[72] Huang, X. M. H., Feng, X. L., Zorman, C. A., Mehregany, M. & Roukes, M. L. VHF, UHF, and microwave frequency nanoelectromechanical resonators. *New J. Phys.* **7**, 247 (2005).

[73] Cleland, A. N., Pophristic, M. & Ferguson, I. Single-crystal aluminum nitride nanomechanical resonators. *Appl. Phys. Lett.* **79**, 2070 (2001).

[74] Chen, Z. *et al.* An integrated logic circuit assembled on a single carbon nanotube. *Science* **311**, 1735 (2006).

[75] Kocabas, C. *et al.* Radio frequency analog electronics based on carbon nanotube transistors. *Proc. Nat. Acad. Sci. U.S.A.* **105**, 1405 (2008).

[76] Cumings, J. & Zettl, A. Low-friction nanoscale linear bearing realized from multiwall carbon nanotubes. *Science* **289**, 602–604 (2000).

[77] Fennimore, A. M. *et al.* Rotational actuators based on carbon nanotubes. *Nature* **424**, 408–410 (2003).

[78] Cumings, J. & Zettl, A. Localization and nonlinear resistance in telescopically extended nanotubes. *Phys. Rev. Lett.* **93**, 086801 (2004).

[79] Cumings, J., Collins, P. G. & Zettl, A. Peeling and sharpening multiwall nanotubes. *Nature* **406**, 586–586 (2000).

[80] Southwell, R. V. *An Introduction to the Theory of Elasticity for Engineers and Physicists.* Dover Publications, New York, (1969).

[81] Dalton, A. B. *et al.* Super-tough carbon-nanotube fibres - These extraordinary composite fibres can be woven into electronic textiles. *Nature* **423**, 703–703 (2003).

[82] Braginski, V. B., Eller, C., Thorne, K. S., Panov, V. I. & Mitrofanov, V. P. *Systems with Small Dissipation.* University of Chicago Press, Chicago, (1985).

[83] Persson, B. N. J. *Sliding Friction: Physical principles and applications.* Nanoscience and Technology. Springer, New York, 2nd edition, (2000).

[84] Yasumura, K. Y. *et al.* Quality factors in micron- and submicron-thick cantilevers. *J. Microelectromech. Syst.* **9**, 117–125 (2000).

[85] Regal, B. *Radio: The life story of a technology.* Greenwood Publishing Group, Westport, CT, (2005).

[86] Balanis, C. A. *Antenna Theory: Analysis and design.* John Wiley, Hoboken, NJ, 3rd edition, (2005).

[87] Mathur, N. Nanotechnology - Beyond the silicon roadmap. *Nature* **419**, 573–575 (2002).

[88] Yao, Z., Postma, H. W. C., Balents, L. & Dekker, C. Carbon nanotube intramolecular junctions. *Nature* **402**, 273–276 (1999).

[89] Collins, P. G. & Zettl, A. Unique characteristics of cold cathode carbon-nanotube-matrix field emitters. *Phys. Rev. B* **55**, 9391–9399 (1997).

[90] Tans, S. J., Verschueren, A. R. M. & Dekker, C. Room-temperature transistor based on a single carbon nanotube. *Nature* **393**, 49–52 (1998).

[91] Collins, P. G., Bradley, K., Ishigami, M. & Zettl, A. Extreme oxygen sensitivity of electronic properties of carbon nanotubes. *Science* **287**, 1801–1804 (2000).

[92] Kong, J. *et al.* Nanotube molecular wires as chemical sensors. *Science* **287**, 622–625 (2000).

[93] de Heer, W. A., Chatelain, A. & Ugarte, D. A carbon nanotube field-emission electron source. *Science* **270**, 1179–1180 (1995).

[94] Treacy, M. M. J., Ebbesen, T. W. & Gibson, J. M. Exceptionally high Young's modulus observed for individual carbon nanotubes. *Nature* **381**, 678–680 (1996).

[95] Collins, P. G., Arnold, M. S. & Avouris, P. Engineering carbon nanotubes and nanotube circuits using electrical breakdown. *Science* **292**, 706 (2001).

[96] Hanson, G. W. Fundamental transmitting properties of carbon nanotube antennas. *IEEE Trans. Antennas Propag.* **53**, 3426–3435 (2005).

[97] Wang, Y. *et al.* Receiving and transmitting light-like radio waves: Antenna effect in arrays of aligned carbon nanotubes. *Appl. Phys. Lett.* **85**, 2607–2609 (2004).

[98] Wang, Z. L., Gao, R. P., de Heer, W. A. & Poncharal, P. In situ imaging of field

emission from individual carbon nanotubes and their structural damage. *Appl. Phys. Lett.* **80**, 856–858 (2002).

[99] Dean, K. A. & Chalamala, B. R. Field emission microscopy of carbon nanotube caps. *J. Appl. Phys.* **85**, 3832–3836 (1999).

[100] Bonard, J. M., Klinke, C., Dean, K. A. & Coll, B. F. Degradation and failure of carbon nanotube field emitters. *Phys. Rev. B* **67**, 115406 (2003).

[101] Kahn, J. M., Katz, R. H. & Pister, K. S. J. Emerging challenges: Mobile networking for "Smart Dust". *J. Commun. Net.* **2**, 188–196 (2000).

[102] Thornton, W. & Ord, J. Physiological mass measurements in Skylab. *Proc. of the Skylab Life Sci. Symp* **1**, 373–386 (1974).

[103] Schottky, W. Regarding spontaneous current fluctuation in different electricity conductors. *Ann. Phys.* **57**, 541–567 (1918).

[104] Hartmann, C. ber die bestimmung des elektrischen elementarquantums aus dem schroteffekt. *Ann. Phys.* **65**, 51–78 (1921).

[105] Hutchison, J. L. *et al.* Double-walled carbon nanotubes fabricated by a hydrogen arc discharge method. *Carbon* **39**, 761–770 (2001).

[106] Jensen, K., Girit, C., Mickelson, W. & Zettl, A. Tunable nanoresonators constructed from telescoping nanotubes. *Phys. Rev. Lett.* **96**, 215503 (2006).

[107] Arthur, J. R. & Cho, A. Y. Adsorption and desorption kinetics of Cu and Au on (0001) graphite. *Surf. Sci.* **36**, 641–660 (1973).

[108] van der Ziel, A. *Noise.* Prentice-Hall Electrical Engineering Series. Prentice-Hall, Inc., New York, (1954).

[109] Langmuir, I. Chemical reactions at low pressures. *J. Am. Chem. Soc.* **37**, 1139–1167 (1915).

[110] Newland, D. *An Introduction to Random Vibrations and Spectral Analysis.* Longman, Inc., New York, (1984).

[111] Regan, B. C., Aloni, S., Ritchie, R. O., Dahmen, U. & Zettl, A. Carbon nanotubes as nanoscale mass conveyors. *Nature* **428**, 924–927 (2004).

[112] Zhang, Y., Franklin, N. W., Chen, R. J. & Dai, H. Metal coating on suspended carbon nanotubes and its implication to metal-tube interaction. *Chem. Phys. Lett.* **331**, 35–41 (2000).

[113] Karas, M. & Hillenkamp, F. Laser desorption ionization of proteins with molecular masses exceeding 10000 daltons. *Anal. Chem.* **60**, 2299–2301 (1988).

[114] Fenn, J., Mann, M., Meng, C., Wong, S. & Whitehouse, C. Electrospray ionization for mass spectrometry of large biomolecules. *Science* **246**, 64–71 (1989).

[115] Demczyk, B. G. *et al.* Direct mechanical measurement of the tensile strength and elastic modulus of multiwalled carbon nanotubes. *Mater. Sci. Eng., A* **334**, 173–178 (2002).

[116] Yu, M. F. *et al.* Strength and breaking mechanism of multiwalled carbon nanotubes under tensile load. *Science* **287**, 637–640 (2000).

[117] Dai, H. J., Hafner, J. H., Rinzler, A. G., Colbert, D. T. & Smalley, R. E. Nanotubes as nanoprobes in scanning probe microscopy. *Nature* **384**, 147–150 (1996).

[118] Schadler, L. S., Giannaris, S. C. & Ajayan, P. M. Load transfer in carbon nanotube epoxy composites. *Appl. Phys. Lett.* **73**, 3842–3844 (1998).

[119] Zhang, M., Atkinson, K. R. & Baughman, R. H. Multifunctional carbon nanotube yarns by downsizing an ancient technology. *Science* **306**, 1358–1361 (2004).

[120] Edwards, B. C. Design and deployment of a space elevator. *Acta Astronautica* **47**, 735–744 (2000).

[121] Wong, E. W., Sheehan, P. E. & Lieber, C. M. Nanobeam mechanics: Elasticity, strength, and toughness of nanorods and nanotubes. *Science* **277**, 1971–1975 (1997).

[122] Chen, X., Kis, A., Zettl, A. & Bertozzi, C. R. A cell nanoinjector based on carbon nanotubes. *Proc. Nat. Acad. Sci. U.S.A.* **104**, 8218–8222 (2007).

[123] Waters, J. F., Riester, L., Jouzi, M., Guduru, P. R. & Xu, J. M. Buckling instabilities in multiwalled carbon nanotubes under uniaxial compression. *Appl. Phys. Lett.* **85**, 1787–1789 (2004).

[124] Waters, J. F. *et al.* Shell buckling of individual multiwalled carbon nanotubes using nanoindentation. *Appl. Phys. Lett.* **87**, 103109 (2005).

[125] Falvo, M. R. *et al.* Bending and buckling of carbon nanotubes under large strain. *Nature* **389**, 582–584 (1997).

[126] Lourie, O., Cox, D. M. & Wagner, H. D. Buckling and collapse of embedded carbon nanotubes. *Phys. Rev. Lett.* **81**, 1638–1641 (1998).

[127] Meyer, G. & Amer, N. M. Novel optical approach to atomic force microscopy. *Appl. Phys. Lett.* **53**, 1045–1047 (1988).

[128] Sader, J. E., Larson, I., Mulvaney, P. & White, L. R. Method for the calibration of atomic-force microscope cantilevers. *Rev. Sci. Instrum.* **66**, 3789–3798 (1995).

[129] Kis, A., Jensen, K., Aloni, S., Mickelson, W. & Zettl, A. Interlayer forces and ultralow sliding friction in multiwalled carbon nanotubes. *Phys. Rev. Lett.* **97**, 025501 (2006).

[130] Timoshenko, S. & Gere, J. *Theory of Elastic Stability.* McGraw-Hill Book Company, Inc., New York, (1961).

[131] Qian, D., Wagner, G. J., Liu, W. K., Yu, M.-F. & Ruoff, R. S. Mechanics of carbon nanotubes. *Appl. Mech. Rev.* **55**, 495–533 (2002).

[132] Brazier, L. G. On the flexure of thin cylindrical shells and other "thin" sections. *Proc. R. Soc. London, Ser. A* **116**, 104–114 (1927).

[133] Calladine, C. R. *Theory of Shell Structures.* Cambridge University Press, Cambridge, (1983).

[134] Blakslee, O. L., Proctor, D. G., Seldin, E. J., Spence, G. B. & Weng, T. Elastic constants of compression-annealed pyrolytic graphite. *J. Appl. Phys.* **41**, 3373–3382 (1970).

[135] (Shackelford, J. & Alexander, W., eds). *CRC Materials Science and Engineering Handbook.* CRC Press, Boca Raton Florida, 3rd edition, (2001).

[136] Shibutani, Y. & Ogata, S. Mechanical integrity of carbon nanotubes for bending and torsion. *Modell. Simul. Mater. Sci. Eng.* **12**, 599–610 (2004).

[137] Tomlinson, G. A. A molecular theory of friction. *Philos. Mag.* **7**, 905–939 (1929).

[138] Charlier, J. C. & Michenaud, J. P. Energetics of multilayered carbon tubules. *Phys. Rev. Lett.* **70**, 1858 (1993).

[139] Benedict, L. X. *et al.* Microscopic determination of the interlayer binding energy in graphite. *Chem. Phys. Lett.* **286**, 490 (1998).

[140] Kolmogorov, A. N. & Crespi, V. H. Smoothest bearings: interlayer sliding in multi-walled carbon nanotubes. *Phys. Rev. Lett.* **85**, 4727 (2000).

[141] Smith, B. W. & Luzzi, D. E. Electron irradiation effects in single wall carbon nanotubes. *J. Appl. Phys.* **90**, 3509 (2001).

[142] Crespi, V. H., Chopra, N. G., Cohen, M. L. & Zettl, A. Anisotropic electron-beam damage and the collapse of carbon nanotubes. *Phys. Rev. B* **54**, 5927 (1996).

[143] Huhtala, M. *et al.* Improved mechanical load transfer between shells of multiwalled carbon nanotubes. *Phys. Rev. B* **70**, 045404 (2004).

[144] Ajayan, P. M., Ravikumar, V. & Charlier, J. C. Surface reconstructions and dimensional changes in single-walled carbon nanotubes. *Phys. Rev. Lett.* **81**, 1437 (1998).

[145] Bockrath, M. *et al.* Luttinger-liquid behaviour in carbon nanotubes. *Nature* **397**, 598–601 (1999).

[146] Hone, J., Whitney, M., Piskoti, C. & Zettl, A. Thermal conductivity of single-walled carbon nanotubes. *Phys. Rev. B* **59**, R2514–R2516 (1999).

[147] Ebbesen, T. W. & Ajayan, P. M. Large-scale synthesis of carbon nanotubes. *Nature* **358**, 220–222 (1992).

[148] Li, W. Z. *et al.* Large-scale synthesis of aligned carbon nanotubes. *Science* **274**, 1701–1703 (1996).

[149] Guo, T., Nikolaev, P., Thess, A., Colbert, D. T. & Smalley, R. E. Catalytic growth of single-walled nanotubes by laser vaporization. *Chem. Phys. Lett.* **243**, 49–54 (1995).

[150] Nikolaev, P. *et al.* Gas-phase catalytic growth of single-walled carbon nanotubes from carbon monoxide. *Chem. Phys. Lett.* **313**, 91–97 (1999).

[151] Ajayan, P. M. & Iijima, S. Capillarity-induced filling of carbon nanotubes. *Nature* **361**, 333–334 (1993).

[152] Svensson, K., Olin, H. & Olsson, E. Nanopipettes for metal transport. *Phys. Rev. Lett.* **93**, 145901 (2004).

[153] Satishkumar, B. C., Govindaraj, A., Sen, R. & Rao, C. N. R. Single-walled nanotubes by the pyrolysis of acetylene-organometallic mixtures. *Chem. Phys. Lett.* **293**, 47–52 (1998).

[154] Bonard, J. M., Croci, M., Conus, F., Stockli, T. & Chatelain, A. Watching carbon nanotubes grow. *Appl. Phys. Lett.* **81**, 2836–2838 (2002).

[155] Ho, P. S. & Kwok, T. Electromigration in metals. *Rep. Prog. Phys.* **52**, 301–348 (1989).

[156] Pratt, J. N. & Sellors, R. G. R. *Electrotransport in Metals and Alloys.* Diffusion and defect monograph series, No. 2. Trans Tech SA, Riehen, (1973).

[157] Hansen, M. & Elliott, R. P. *Constitution of Binary Alloys.* McGraw-Hill, New York, 2nd edition, (1958).

[158] Kukovitsky, E. F., L'Vov, S. G. & Sainov, N. A. VLS-growth of carbon nanotubes from the vapor. *Chem. Phys. Lett.* **317**, 65–70 (2000).

[159] Ichihashi, T., Fujita, J., Ishida, M. & Ochiai, Y. In situ observation of carbon-nanopillar tubulization caused by liquidlike iron particles. *Phys. Rev. Lett.* **92**, 215702 (2004).

[160] Gorbunov, A., Jost, O., Pompe, W. & Graff, A. Solid-liquid-solid growth mechanism of single-wall carbon nanotubes. *Carbon* **40**, 113–118 (2002).

[161] Buffat, P. & Borel, J. P. Size effect on melting temperature of gold particles. *Phys. Rev. A* **13**, 2287–2298 (1976).

[162] Krivoruchko, O. P. & Zaikovskii, V. I. A new phenomenon involving the formation of liquid mobile metal-carbon particles in the low-temperature catalytic graphitisation of amorphous carbon by metallic Fe, Co and Ni. *Mendeleev Commun.* , 97–100 (1998).

[163] (Lide, D. R., ed). *CRC Handbook of Chemistry and Physics.* CRC Press, Boca Raton, Florida, (1999).

[164] Mason, N., Biercuk, M. J. & Marcus, C. M. Local gate control of a carbon nanotube double quantum dot. *Science* **303**, 655–658 (2004).

[165] Louie, S. G. Electronic properties, junctions, and defects of carbon nanotubes. in *Carbon Nanotubes*, 113–145. Springer, Berlin (2001).

[166] Iijima, S. Helical microtubules of graphitic carbon. *Nature* **354**, 56 (1991).

[167] Iijima, S. & Ichihashi, T. Single-shell carbon nanotubes of 1-nm diameter. *Nature* **363**, 603 (1993).

[168] Saito, R., Fujita, M., Dresselhaus, G. & Dresselhaus, M. S. Electronic structure of chiral graphene tubules. *Appl. Phys. Lett.* **60**, 2201 (1992).

[169] Saito, R., Dresselhaus, G. & Dresselhaus, M. *Physical Properties of Carbon Nanotubes.* Imperial College Press, London, (1998).

[170] Di Ventra, M., Evoy, S. & Heflin, J. R. *Introduction to Nanoscale Science and Technology.* Springer, New York, 3rd edition, (2004).

[171] Lu, J. P. Elastic properties of carbon nanotubes and nanoropes. *Phys. Rev. Lett.* **79**, 1297–1300 (1997).

[172] Krishnan, A., Dujardin, E., Ebbesen, T. W., Yianilos, P. N. & Treacy, M. M. J. Young's modulus of single-walled nanotubes. *Phys. Rev. B* **58**, 14013 (1998).

[173] Walters, D. A. *et al.* Elastic strain of freely suspended single-wall carbon nanotube ropes. *Appl. Phys. Lett.* **74**, 3803 (1999).

[174] Mintmire, J. W. & White, C. T. Electronic and structural properties of carbon nanotubes. *Carbon* **33**, 893 (1995).

[175] Durkop, T., Getty, S. A., Cobas, E. & Fuhrer, M. S. Extraordinary mobility in semiconducting carbon nanotubes. *Nano Lett.* **4**, 35 (2004).

[176] Park, J. Y. *et al.* Electron-phonon scattering in metallic single-walled carbon nanotubes. *Nano Lett.* **4**, 517 (2004).

[177] Kasumov, A. Y., Khodos, I. I., Ajayan, P. M. & Colliex, C. Electrical resistance of a single carbon nanotube. *Europhys. Lett.* **34**, 429 (1996).

[178] Yao, Z., Kane, C. L. & Dekker, C. High-field electric transport in single-wall carbon nanotubes. *Phys. Rev. Lett.* **84**, 2941 (2000).

[179] Zhou, X., Park, J. Y., Huang, S., Liu, J. & McEuen, P. L. Band structure, phonon scattering, and the performance limit of single-walled carbon nanotube transistors. *Phys. Rev. Lett.* **95**, 146805 (2005).

[180] McEuen, P. L., Fuhrer, M. S. & Park, H. Single-walled carbon nanotube electronics. *IEEE Trans. Nano.* **1**, 78 (2002).

[181] Berber, S., Kwon, Y. & Tomanek, D. Unusually high thermal conductivity of carbon nanotubes. *Phys. Rev. Lett.* **84**, 4613 (2000).

[182] Kim, P., Shi, L., Majumdar, A. & McEuen, P. L. Thermal transport measurements of individual multiwalled nanotubes. *Phys. Rev. Lett.* **87**, 215502 (2001).

[183] Pop, E., Mann, D., Wang, Q., Goodson, K. & Dai, H. J. Thermal conductance of an individual single-wall carbon nanotube above room temperature. *Nano Lett.* **6**, 96 (2006).

[184] Anthony, T. R. *et al.* Thermal-diffusivity of isotopically enriched C-12 diamond. *Phys. Rev. B* **42**, 1104 (1990).

[185] Fujii, M. *et al.* Measuring the thermal conductivity of a single carbon nanotube. *Phys. Rev. Lett.* **95**, 065502 (2005).

[186] Kwon, Y., S., B. & D., T. Thermal contraction of carbon fullerenes and nanotubes. *Phys. Rev. Lett.* **92**, 015901 (2004).

[187] Hone, J., Batlogg, B., Benes, Z., Johnson, A. T. & Fischer, J. E. Quantized phonon spectrum of single-wall carbon nanotubes. *Science* **289**, 1730 (2000).

[188] Yi, W., Lu, L., Dian-lin, Z., Pan, Z. W. & Xie, S. S. Linear specific heat of carbon nanotubes. *Phys. Rev. B* **59**, R9015 (1999).

[189] Chang, C. W., Okawa, D., Garcia, H. G., Majumdar, A. & A., Z. Nanotube phonon waveguide. *Phys. Rev. Lett.* **99**, 045901 (2007).

[190] Landau, L. D. & Lifshitz, E. M. *Theory of Elasticity.* Pergamon Press, New York, 3rd edition, (1986).

[191] Dohn, S., Svendsen, W., Boisen, A. & Hansen, O. Mass and position determination of attached particles on cantilever based mass sensors. *Rev. Sci. Instrum.* **78**, 103303 (2007).

Appendix A

Properties of carbon nanotubes

A carbon nanotube is one or more sheets of graphene that have been rolled into a tube typically with a diameter of a few nanometers and a length on the order of microns (see Fig. A.1). When only a single sheet of graphene is used, this material is called a single-walled carbon nanotube (SWNT), and when multiple sheets are used it is called a multi-walled carbon nanotube (MWNT). These materials were discovered in 1991 by S. Iijima[166, 167], and since then there has been an immense amount of research on their fundamental properties and potential applications.

Single-walled carbon nanotubes are classified by their chiral vector, $\vec{c_h}$, or the vector that describes which points on graphene's honeycomb lattice to connect to form the tube (see Fig. A.2). This vector may be written in terms of the lattice vectors of graphene, $\vec{a_1}$ and $\vec{a_2}$, so that $\vec{c_h} = n\vec{a_1} + m\vec{a_2}$. Often, nanotubes are referenced simply by the indices (n, m) of this vector. The properties of carbon nanotubes are intimately tied to their chirality. For example, as we discuss below, the chirality determines whether a carbon
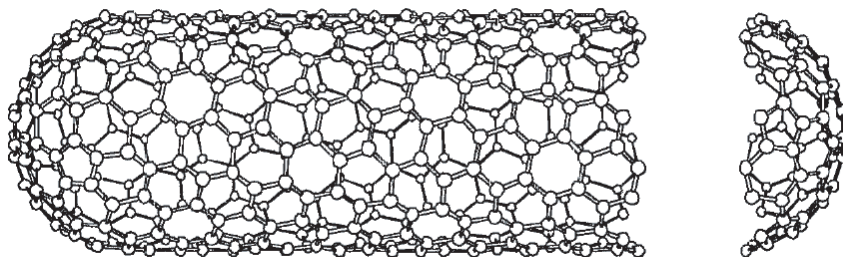
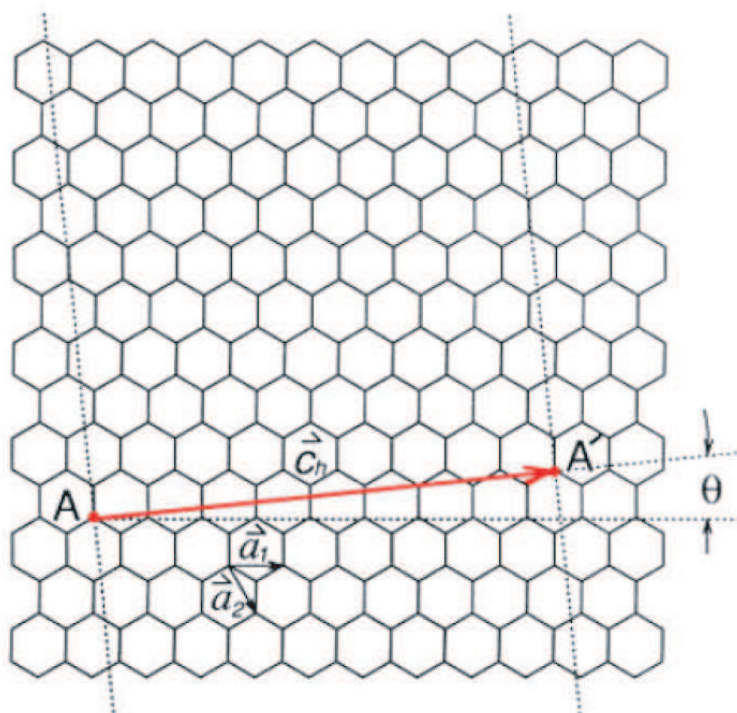Figure A.1: Structure of a single-walled carbon nanotube[168].

Figure A.2: The chiral vector, $\vec{c_h}$, of a single-walled carbon nanotube[168].
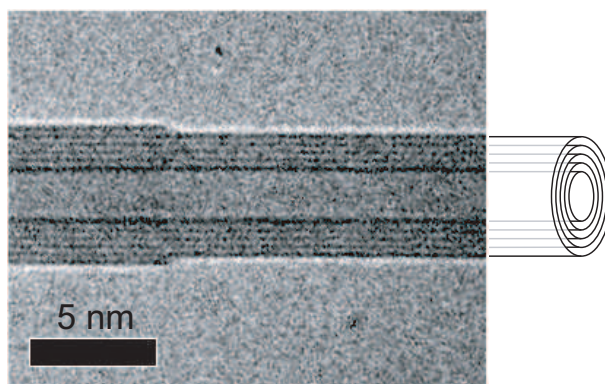
Figure A.3: TEM image of a 6-walled nanotube that narrows to a 5-walled nanotube

nanotube is metallic or semiconducting.

Because their properties are intimately tied to their structure, atomic resolution observation of carbon nanotubes during a measurement is invaluable. Thus, the transmission electron microscope (TEM), with its atomic resolution and ability to image the inner nanotubes in a multi-walled carbon nanotube, is a powerful tool for observing carbon nanotubes and an excellent environment within which to perform experiments. Figure A.3 shows a TEM image of a multi-walled carbon nanotube. As shown, each shell of the nanotube appears as two dark parallel lines. These dark lines originate from the electron scattering, which occurs predominately in the carbon planes parallel to the electron beam. The spacing between shells is 3.4Å, similar to the spacing between the layers of graphite.

In this appendix, we briefly review the important mechanical, electrical, and thermal properties of carbon nanotubes, focusing on those that are relevant to this thesis. Tables A.1, A.2, and A.3 summarize the physical constants for both single and multi-walled carbon nanotubes. Of course, the physics of carbon nanotubes is a vast and well-developed field,

and we can not hope to cover all of it. For a more thorough review, we recommend *Physical Properties of Carbon Nanotubes* by R. Saito *et al.*[169].

A.1   Mechanical properties

Carbon nanotubes are among the strongest materials ever created. Their tensile strength exceeds 63 GPa[116], which is more than 100 times that of steel. Moreover, their Young's modulus is greater than 1 TPa[94], a record for any material. These remarkable properties stem from the carbon-carbon sp^2 hybridized bonds that form graphene's honeycomb lattice. The carbon-carbon sp^2 bond is the strongest chemical bond in nature with a binding energy of 7.5 eV/atom[170].

As a result of this amazing strength, carbon nanotubes have been proposed as mechanical components for a number of applications. Their strength combined with their high aspect ratio makes them ideal for the sharp tips of AFM cantilevers[117]. Also, as they are relatively light, carbon nanotubes are especially attractive as a structural material due to their high strength-to-weight ratio[118, 81, 119]. Finally, their high Young's modulus and low density give nanotubes an impressive speed-of-sound (see Tbl. A.1) and characteristically high mechanical resonance frequencies, which are important for the nanomechanical resonator applications developed in Ch. 2, 3, and 4.

In contrast to the strong carbon-carbon bonds within a nanotube, the van der Waals bond between concentric nanotubes in a MWNT is very weak. In Ch. 6, we measure the cohesive energy here to be just 0.033 eV/atom. The weak van der Waals bond enables the fabrication of a variety of interesting nanomechanical devices, such as nanoscale linear

Table A.1: Mechanical properties of carbon nanotubes.

Material	SWNT	MWNT
Density [g/cm^3]	2.03	2.24[1]
Speed of sound (TA) [m/s]	9430 [169]	12300[1] [169]
Speed of sound (LA) [m/s]	20350 [169]	21000[1] [169]
Young's modulus [GPa]	1000-1250 [171, 172]	100-1800 [94, 121, 171, 5, 116]
Shear modulus [GPa]	450 [171]	450 [171]
Poisson ratio [#]	0.17-0.28 [134, 171]	0.17-0.27 [134, 171]
Tensile strength [GPa]	>45 [173]	11-63 [115, 116]

and rotational bearings[76, 77]. Here, an inner nanotube core is free to slide or rotate within the atomically smooth casing of an outer nanotube shell. This property is discussed in detail in Ch. 2 and Ch. 6.

A.2 Electrical properties

Carbon nanotubes inherit their electrical properties from graphene; though interesting properties emerge as a result of their tubular structure and quasi-one-dimensional nature. We first describe the electrical properties of graphene and later describe how these change for nanotubes.

In the tight binding model, the electrical transport properties of graphene are primarily determined by the π and π^* energy bands, which originate from the $2p_z$ atomic orbitals. There are two π electrons per unit cell, which completely fill the π valence band. Due to symmetry the π and π^* bands are degenerate at the K points of graphene's hexagonal Brillouin zone, shown in Fig. A.4. Thus, the π valance band and the π^* conduction band touch at the Fermi level with zero energy gap. Detailed calculations show that the density
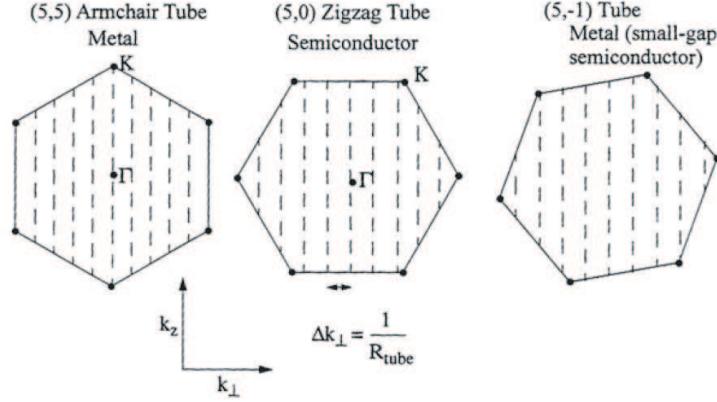
---

[1]Value for bulk graphite

Figure A.4: Brillouin zones for metal and semiconducting nanotubes showing the effect of a quantized wave vector.

of states is zero at the Fermi level, and thus graphene is a zero-gap semiconductor[169].

The tubular structure of carbon nanotubes imposes periodic boundary conditions on the electron's wave function. This results in the quantization of the electron's wave vector in the direction of the chiral vector. The quantization of the wave vector, $\vec{k_\perp}$, is shown as the dashed lines in Fig. A.4. Clearly, a necessary condition for a carbon nanotube to be metallic is that one of these lines must intersect a K point, the only points in graphene's Brillouin zone with zero energy gap. This occurs precisely when the nanotube's chiral indices satisfy: $n - m \equiv 0 \,(\mathrm{mod}\,3)$. As the density of states does not vanish at the Fermi level in a carbon nanotube as it does for graphene[169], these nanotubes are in fact metallic. Nanotubes that do not satisfy this equation are semiconducting with bandgap[169, 174]: $E_\mathrm{g} \approx 2.5\,\mathrm{eV} \cdot a_\mathrm{C-C}/D$, where $a_\mathrm{C-C}$ is the distance between carbon atoms and D is the diameter of the nanotube. The chiral indices of metallic and semiconducting nanotubes are shown graphically in Fig. A.5.

Besides their great tunability, carbon nanotubes exhibit many other notable elec-
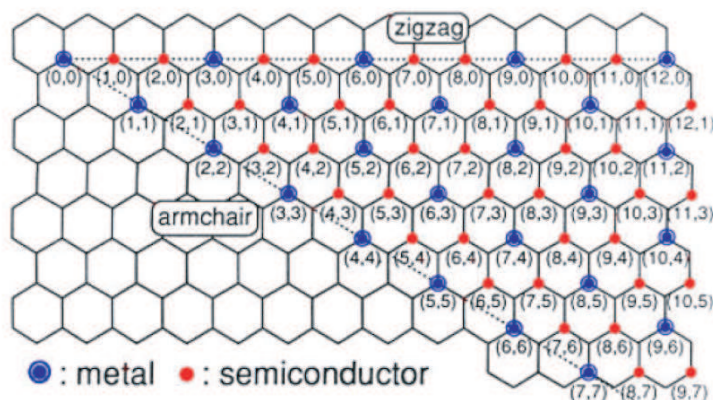
Figure A.5: Chirality determines whether a nanotube is metallic or semiconducting[168].

Table A.2: Electrical properties of carbon nanotubes at room temperature.

Material	SWNT		MWNT
	Semiconducting	Metallic	
Resistivity [Ω cm]	$2.6 \times 10^{-6} - \infty$ [175]	10^{-6} [176]	10^{-4} [177]
Maximum current density [A/cm^2]		10^9[178]	10^9[95]
Intrinsic mobility [cm^2/V s]	$10^4 - 10^5$ [179, 175]		
Electron mean free path [μm]	0.7 [180]	1.6 [176]	25-250 [78]

trical properties. Carbon nanotubes are ballistic conductors with an electron mean free path

of up to 1.6 μm. This ballistic conduction combined with their thermal stability enables

nanotubes to carry high current densities on the order of 10^9 A/cm^2, which is 100 times

greater than copper wire can withstand. Finally, due to their long, thin structure, carbon

nanotubes are excellent field emitters with a low turn-on voltage, as described in detail in

Ch. 3.

Table A.3: Thermal properties of carbon nanotubes at room temperature.

Material	SWNT	MWNT
Thermal conductivity [W/m·K]	3500 [183]	3000 [182, 185]
Thermal expansion coefficient [K^{-1}]	-1.1×10^{-5} [186]	-1.1×10^{-5} [186]
Specific heat [J/kg K]	620 [187]	490 [188]
Volumetric specific heat [J/m^3 K]	1.26×10^6 [187]	1.10×10^6 [188]
Phonon mean free path [μm]	0.5-1.5 [146]	0.05-0.5 [189, 182]

A.3 Thermal properties

Like the other carbon allotropes diamond and graphite, carbon nanotubes are excellent thermal conductors. In all these materials, phonons, rather than electrons, predominately carry the thermal energy. Thus, their high thermal conductivity may be attributed to their high phonon velocities, which result from their high elastic modulus and low density. The room temperature thermal conductivity of single walled nanotubes is predicted to be 6600 W/m K[181], though measured values for both single and multi-walled nanotubes are typically $\sim 3000 - 3500$ W/m K[182, 183]. Still this compares favorably with the value for one of the best thermal conductors, nearly isotopically pure diamond, 3320 W/m K[184].

The tubular structure of carbon nanotubes has two primary effects on their phonon properties. First, due to the periodic boundary conditions, the phonon wave vector in the direction of the chiral vector is quantized. This results in the appearance of discrete subbands in the phonon dispersion relation. Second, carbon nanotubes have four low-lying acoustic phonon modes, rather the the three of graphite. There are two transverse, one longitudinal, and one "twist" mode. The phonon velocities of these modes are predicted to be: $v_{TA} = 7.5 \times 10^3$ m/s, $v_{LA} = 2 \times 10^4$ m/s, and $v_{twist} = 1 \times 10^4$ m/s.

Appendix B

Classical elastic theory

B.1   Euler-Bernoulli beam theory

The equation of motion for the displacement $y(x)$ of a rigid beam under tension is[190]

$$\frac{\partial^2}{\partial x^2}\left(YI\frac{\partial^2 y}{\partial x^2}\right) - \frac{\partial}{\partial x}\left(T\frac{\partial y}{\partial x}\right) = f(x) - \rho A\frac{\partial^2 y}{\partial t^2}. \tag{B.1}$$

Here Y is the Young's modulus, I is the areal moment of inertia, T is the tension, $f(x)$ is the transverse external force per unit length, ρ is the density, and A is the cross-sectional area. Solving Eq. B.1 for the mode shape, $y(x)$, of the beam (assuming no external force), we find:

$$y(x) = A\cos(\beta x) + B\sin(\beta x) + C\cosh(\beta x) + D\sinh(\beta x) \tag{B.2}$$

where

$$\beta = \pm\left(\frac{T \pm \sqrt{T^2 + 4\rho AYI\omega^2}}{2YI}\right)^{1/2}. \tag{B.3}$$

The constants A, B, C, and D are determined by the boundary conditions of the beam.
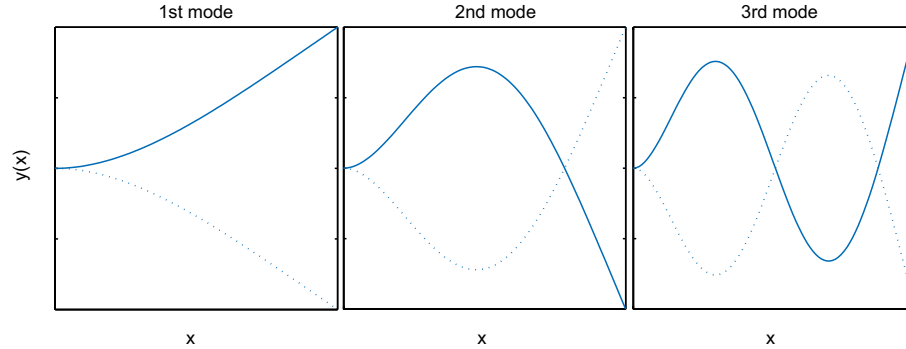
Figure B.1: Vibrational modes of a cantilevered resonator.

The boundary conditions depend on the manner in which the beam attaches to its support. The two forms of attachment encountered in this thesis are clamped and pin-jointed. In a clamped attachment, the beam is at a fixed angle to the support, and thus, the boundary conditions for a clamp at $x = 0$ are: $y(0) = y'(0) = 0$. In a pin-jointed attachment, there is no bending moment at the support, so the boundary conditions are: $y(0) = y''(0) = 0$. Obviously, for doubly supported beams such boundary conditions are applied at each support. For cantilevered beams, there is no bending moment or shear force at the free end $(x = L)$, so the boundary conditions here are: $y''(L) = y'''(L) = 0$.

Applying the boundary conditions for a clamped, cantilevered beam, we find the shape of the fundamental mode (assuming no tension) to be:

$$y_0(x) = a_0 \left(\cos \left(\beta_0 \frac{x}{L} \right) - \cosh \left(\beta_0 \frac{x}{L} \right) \right) + b_0 \left(\sin \left(\beta_0 \frac{x}{L} \right) - \sinh \left(\beta_0 \frac{x}{L} \right) \right) \tag{B.4}$$

where $a_0/b_0 = -1.3622$ and $\beta_0 = 1.875$[33]. The mode shapes of the fundamental mode and the first few higher modes are shown in Fig. B.1.

B.2 Rayleigh-Ritz approximation

The Rayleigh-Ritz method[191] provides a simple means of approximating resonance frequencies of complex mechanical systems. The central assumption of the approximation is the equality of the time-averaged kinetic and potential energies of the system in resonance. For rigid beams under tension this approximation yields the following equation for resonance frequency:

$$\omega^2 = \frac{\int_0^L dx \left(YIy''^2 + Ty'^2 \right)}{\int_0^L dx \rho A y^2} \tag{B.5}$$

Note that the amplitude of $y(x)$ is irrelevant as it appears evenly in numerator and denominator.

To simplify calculations, we use an approximation for the mode shape of the beam, rather than the exact shape (Eq. B.2). Specifically, we use the simplest polynomial function that satisfies the boundary conditions. For a cantilevered beam ($y(0) = 0, y'(0) = 0, y''(L) = 0, y'''(L) = 0$), this approximate mode shape is: $y(x) = x^4 - 4Lx^3 + 6L^2x^2$.

Applying the Rayleigh-Ritz formula (Eq. B.5) to this mode shape yields an equation for the resonance frequency of the fundamental mode of a cantilever with no tension[1]:

$$\omega_0 = \sqrt{\frac{k_{\text{eff}}}{m_{\text{eff}}}} \approx \sqrt{\frac{3YI/L^3}{0.24\rho AL}}. \tag{B.6}$$

With tension the formula for resonance frequency becomes

$$\omega_0 \approx \sqrt{\frac{3YI/L^3 + 1.07 \cdot T/L}{0.24\rho AL}}. \tag{B.7}$$

---

[1]We chose constants such that $k_{\text{eff}} = 3YI/L^3$ represents the effective spring constant relating the deflection of the end of the cantilever to a transverse force applied to the end of the cantilever.

In some experiments (see Ch. 4), we load extra point-like masses (*i.e.* atoms) onto

the beam. These masses may be modeled as a local modification of the beam's density:

$\rho(x) = \rho_0 + m_i \delta(x_i)/A$. Again, using the Rayleigh-Ritz approximation, we find:

$$\omega_0 \approx \sqrt{\frac{3YI/L^3 + 1.07 \cdot T/L}{0.24(\rho_0 AL + \Sigma_i w(x_i) m_i)}} \tag{B.8}$$

Here, $w(x)$ is a weighting function for the mass, which depends on its position along the

beam. Obviously, masses near the tip of the cantilever will have a larger effect than those

near the base. The weighting function is

$$w(x) = \frac{L \, y_0{}^2(x)}{\int_0^L dx \, y_0{}^2(x)} \tag{B.9}$$

which for cantilevered beams is

$$w(x) = \frac{45}{104L^8} y_0{}^2(x). \tag{B.10}$$

Repeating this calculation for doubly clamped beams with boundary conditions,

$y(0) = 0, y'(0) = 0, y(L) = 0, y'(L) = 0$ and mode shape $y(x) = x^2(x - L)^2$, we find[2]:

$$\omega_0 \approx \sqrt{\frac{384YI/L^3 + 9.14 \cdot T/L}{0.76\,(\rho_0 AL + \Sigma_i w(x_i) m_i)}} \tag{B.11}$$

with weighting function

$$w(x) = \frac{630}{L^8} x^4(x - L)^4. \tag{B.12}$$

---

[2]We chose constants such that $k_{\text{eff}} = 384YI/L^3$ represents the effective spring constant relating the deflection of the center of the beam to a transverse force applied uniformly over the length of the beam.